Development of a Novel Radial Heat Flow Apparatus for Measuring Solid-Liquid Interfacial Energy

Thesis Submitted for the Degree of

Master of Philosophy

At the University of Leicester

by

SungWoo Son

Department of Engineering

University of Leicester

2016

Abstract: Development of a Novel Radial Heat Flow Apparatus for measuring Solid-Liquid interfacial energy by Sung Woo Son

The solid-liquid interfacial energy,σ_{SL}, plays an important role in all processes that involves nucleation and growth of solids from its liquid state. In nucleation, interfacial energy affects the temperatures at which solids nucleate from its liquids during growth, the interfacial energy affects the transformation rate. Solid-liquid interfacial energy also plays important role in determining the growth morphology which may lead to solidification occurring in the preferred crystallographic directions. The solid-liquid interfacial energy is also important in the phenomena such as coarsening of dendrites, sintering and wetting.

It is thus very important to have quantitative values of the interfacial energy, as this will assist in gaining fundamental knowledge into the structural nature and physics of interfaces.

To measure the σ_{SL}, the grain boundary groove method is used. The grain boundary grooves are obtained in a stable temperature gradient and by using direct application of the Gibbs-Thomson equation on the groove shape, the σ_{SL} can be obtained.

The main aim of this study is to design and construct aradial heat flow apparatus and then to commission and test using a commercial Al alloy. The Radial heat flow apparatus provides ideal set up to obtain grain boundary groove shape, as the central heating element in the centre of the sample and the water cooling jacket around the sample provides the radial temperature gradient to produce solid-liquid interface.

The equilibrated grain boundary groove shapes for an industrial alloy LM25 were obtained in experiment at above eutectic temperature for 10 days with the temperature control to within ±0.05K. From the observed grain boundary groove shapes, the σ_{SL} for LM25 has been determined to be 167.361± 8.312 mJ/m^2.

Publications

1. S. Son, H.B. Dong. “Measuring Solid-Liquid Interfacial Energy by Grain Boundary Groove Profile Method” Materials Today: Proceedings, Volume 2, Supplement 2, 2015, Pages S306-S313

Acknowledgements

I would like to thank my supervisor, Professor Hongbiao Dong, who has supported me throughout my study. He has guided me with encouragement and advice, and have given me many opportunities to experience the life as a PhD student in sending me to many conferences and training courses. He has given me endless support during my time at the university and I am very grateful.

I would like to thank Professor Atkinson, who has also given me a lot of support. I am very grateful to both Professor Dong and Professor Atkinson, and I hope that I can be in a position in the future to repay the support and opportunities I have received from them, to someone else in need.

I also thank all the technicians and colleagues at the Universityfor giving me a lot of support and help in being able to complete an experiment, which I found very challenging. I could not have done it without the help and support of the technicians and colleagues.

I thank my girlfriend Nahee for her endless prayer and support she has given me throughout my PhD studyand her understanding in times of difficulty.

lthank all my families for their thoughts and prayers, and the love and support they have shown me through both good and bad times.

But most of all I thank God for the opportunity that you have given me to study PhD. I thank God for the guidance throughout the study.

Table of Contents

List of Tables

List of figures

1 Solidification Thermodynamics

The solid liquid surface energy, σ_{SL}, is the reversible work, at constant temperature, chemical potential and volume, required in extending or forming a unit area of interface between solid and its liquid. It is known to play a key role in a wide range of metallurgical phenomena from sintering to phase transformations and coarsening [1, 2] and wetting [3]. In order to measure the solid-liquid surface free energy, it is necessary to understand solidification thermodynamics.

1.1 First Law of thermodynamics

The first law of thermodynamics states [4] that, "Energy cannot be created or destroyed and the total quantity of energy available is constant. Heat energy and mechanical energy are convertible". Thus mathematically it can be expressed by,

$$\Delta U = q - w \tag{1.1}$$

whereΔU is the total internal energy change of the system, q is the heat added to the system and w is the work done by the system.

The above equation show that the change in internal energy of a system is equal to the heat put into the system from the surrounding minus the work done by the system on the surrounding.

If a process from state 1 to state 2 occurs at constant pressure, then the equation 1.1 becomes,

$$U_2 - U_1 = q - w \tag{1.2}$$

1.2 System work

In a thermodynamic system, the work done can be visualized as the area below the pressure volume curve which shows the process taking place. In Figure 1.1(a), the line from 'a' to 'b' shows an expansion at constant pressure. Thus at constant pressure, the work done is represented by the area under the curve,

$$w = P\Delta V \tag{1.3}$$

Figure 1.1(b) shows that for non-constant pressure, the work done is expressed by the integral expression for the area under the curve. The more general formula for work done is,

$$w = \int_1^2 P\, dv \tag{1.4}$$

$$w = P\int_1^2 dv = P\,(V_2 - V_1) \tag{1.5}$$

By adding equations 1.2 and 1.5 gives;

$$(U_2 + PV_2) - (U_1 + PV_1) = q_p \tag{1.6}$$

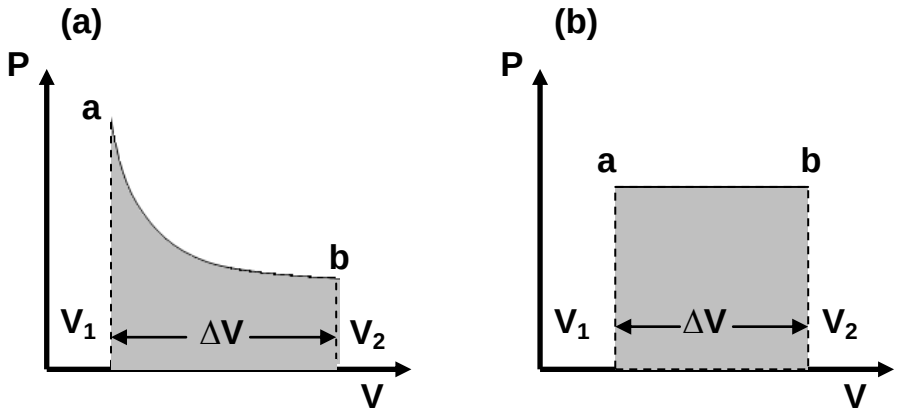

Figure 1.1 System Work (a) Constant Pressure (b) Non Constant Pressure

1.3 Enthalpy change

In a system, the enthalpy change is a thermodynamic function which is the sum of the internal energy, *U*, and external energy, *w*, which is the product of pressure and volume, thus giving the enthalpy expression,

$$H = U + PV \qquad 1.7$$

Where U *is the internal energy,* PV *is the external energy*

The volume change in phase transformation can be large and not negligible, typically between 7% to 45%, but the volume change in metallurgical processes can be considered negligible thus the external energy term in equation 1.7, will become $P\Delta V \rightarrow 0$ giving,

$$\Delta H = \Delta U \qquad 1.8$$

1.4 Latent heat of pure material

During a phase change, the heat absorbed or released by a substance is termed Latent heat [4], where the word latent means 'hidden', as despite the heat energy addition, the temperature does not increase. This occurs whenever a phase change occurs, for example, as a solid turns into a liquid and as a liquid turns into a gas. When a solid turns into a liquid, the heat energy supplied is called the latent heat of fusion, and when a liquid turns into a gas, it is called the latent heat of vaporization.

So the Latent heat for pure material is,

$$L = H_l - H_s = \Delta H \tag{1.9}$$

where ΔH *is latent heat of melting.*

Thus for a process at constant pressure,

$$H_l - H_s = \Delta H = q_p \tag{1.10}$$

This shows that at a constant pressure, the enthalpy change, ΔH, is equal to the heat transfer in and out of the system during the process.

1.5 Entropy

Entropy is a thermodynamic property which is the measure of the quantity of energy that is not available to be used to do work in a process.

For the change of state from a solid to liquid,

$$\Delta S = \frac{\Delta H}{T_m} \tag{1.11}$$

ΔS is the change in entropy of the system

1.6 Second Law of thermodynamics

The second law of thermodynamics states [4] that "it is impossible for heat to be transferred from a lower to a higher temperature without the expenditure of external work".

For an isolated system, external work must be used until it reaches an equilibrium state. When the thermodynamic properties of an isolated system do not change with time, the system is said to be in equilibrium. For an isolated system, the mathematical expression of the second law is given as,

$$\Delta S_{total} \geq 0 \tag{1.12}$$

Where "total" means that both the system and its surroundings are included

1.7 Gibbs free energy and phase transformation

The Gibbs free energy, *G*, is the minimized quantity of chemical potential at equilibrium when both the pressure and temperature of a system are constant and it is given as,

$$G = H - TS \qquad 1.13$$

H is the enthalpy, T is the absolute temperature, S is the entropy

Here the enthalpy represents the sum of internal and external energies of a system as heat content and the entropy is the measure of energy unavailable to do work and also the randomness of the system.

The enthalpy, *H*, is given as in equation 1.7,

$$H = U + PV \qquad 1.14$$

U is the internal energy, P is pressure, V is the volume

Here the internal energy term is the difference between the heat into the system and the work done by the system. The volume change in solid and liquid phases is negligible and thus the *PV→0*, therefore $H \cong U$ as in equation 1.8.

In a single component system, by considering the enthalpy H and entropy S of the system, it can be determined if the solid and liquid phases are in equilibrium with one another. This is shown,

$$G_s = H_s - TS_s \quad \textbf{1.15}$$

$$G_l = H_l - TS_l \quad \textbf{1.16}$$

For the reaction from solid phase to liquid phase, by subtracting equation 1.16 from 1.15, gives,

$$\Delta G_{(s\to l)} = \Delta H_{(s\to l)} - T\Delta S_{(s\to l)} \quad \textbf{1.17}$$

Where $\Delta H_{(s\to l)}$is the molar enthalpy change, $T\Delta S_{(s\to l)}$is the molar entropy change

When a closed system at constant pressure and temperature, has its lowest possible value of Gibbs free energy, it can be considered to be in equilibrium state, $G_s = G_l$. This is,

1.18

$$\left(\Delta G_{(s\to l)}\right)_{T,P} = 0$$

And this occurs at the melting temperature T_m when,

$$\Delta H_{(s\to l)} = T_m \Delta S_{(s\to l)} \quad \textbf{1.19}$$

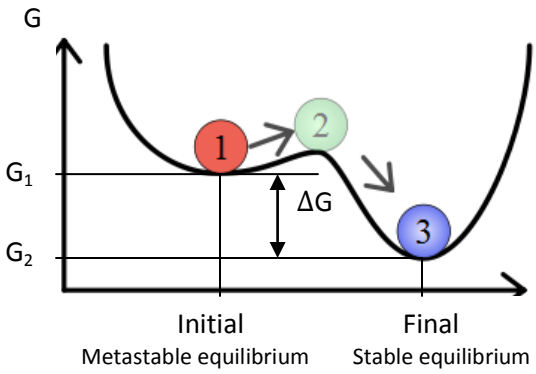

Figure 1.2 Gibbs free energy from initial to final state [7]

This is represented in Figure 1.2 as state 1 and 3 show the equilibrium states. The state 1 is called metastable equilibrium state as it lies at its local minimum but does not have the lowest Gibbs free energy of the system thus making it less stable than the state 3. The transformation from one phase to another occurs when the initial state has a higher Gibbs free energy than the final state i.e. G_1-G_2<0, as initial state is then less stable than the final state of the system. The Gibbs free energy can be varied over some temperature range to look at transformation of solid liquid phase and the equilibrium at the interface. This can be done if a system of steady composition and mass is considered,

$$dG = -SdT + VdP \qquad 1.19$$

And if the pressure is also constant, term *dP* becomes *0*,

$$\left(\frac{G}{T}\right)_P = -S \qquad 1.20$$

This is to show that the Gibbs free energy would decrease when a metal either in pure solid or pure liquid form is heated.

Figure 1.3 shows $G(l)$ and $G(s)$ as a function of temperature in a way that clearly shows how the regions of stability of solid and liquid are determined by the "driving force".

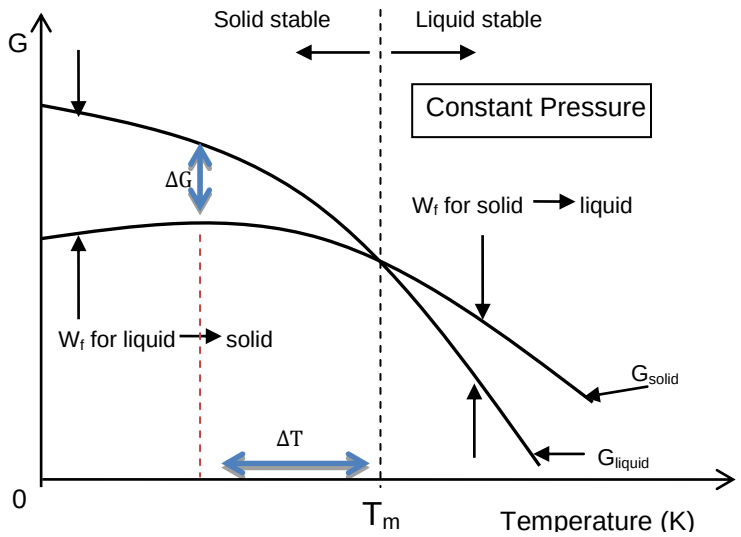

Figure 1.3Schematic representation of the Gibbs free energies of solid and liquid as a function of temperature at constant pressure [6]

The Figure 1.3 above shows that the Gibbs free energy for liquid phase has steeper negative slope than the solid phase as the liquid state has larger entropy. For temperatures below the equilibrium melting temperature, T_m, the solid phase is the stable phase as it has lower Gibbs free energy, and for temperatures above T_m, the liquid phase is the stable phase. At T_m, both the solid and liquid phase can exist in equilibrium as both phases have the same value of Gibbs free energy. From the figure above, it is expected that if a liquid is under-cooled by ΔT below T_m, then the liquid should spontaneously transform to solid. This is not always possible as the first solid forming requires a large amount of energy to form the interface between solid and liquid. For the liquid phase to transform to solid at the temperature ΔT below T_m, atoms in the

liquid must form groups of atoms or form embryos that have similar structure to solids. The decrease in the Gibbs free energy for the transformation process of solid and liquid phase provides the driving force for this solidification process.

Figure 1.3 shows that a material adopts a phase with the lowest possible Gibbs free energy as its equilibrium phase. For example, when the temperature is higher than the equilibrium melting temperature, T_m, the minimum free energy occurs for liquid phase, thus the liquid becomes a stable phase, making a material liquid. When the temperature is lower than T_m, then the minimum free energy occurs for solid phase, making the material solid.

The change of physical state of a material and its transformation from a liquid to solid state occurs at temperature below the equilibrium melting temperature T_e and this temperature is denoted as T_l. The difference between the two temperatures is called under-cooling. This is due to the fact that the transformation process from liquid to solid state requires large amount of energy form a new solid-liquid interface. The under-cooling equation can be used to aid the understanding of solid liquid transformation process and also to measure the interfacial surface energy.

$$T_e - T_l = \Delta T = \Delta T_k + \Delta T_d + \Delta T_r \qquad \textbf{1.21}$$

ΔT_k is the kinetic undercooling, ΔT_d is the diffusion undercooling, ΔT_r is the curvature under-cooling.

The kinetic under-cooling,ΔT_k, can be defined as the undercooling of the interface that drives the transfer of atoms through the energy barrier which determines the growth of either solid or liquid phase. One phase grows if the transfer of atoms is greater towards the phase that is growing. The system reaches equilibrium state once the atom addition rate becomes balanced by the dissolution rate and for pure and multi component systems, this can be represented by, $\Delta T_k = 0$.

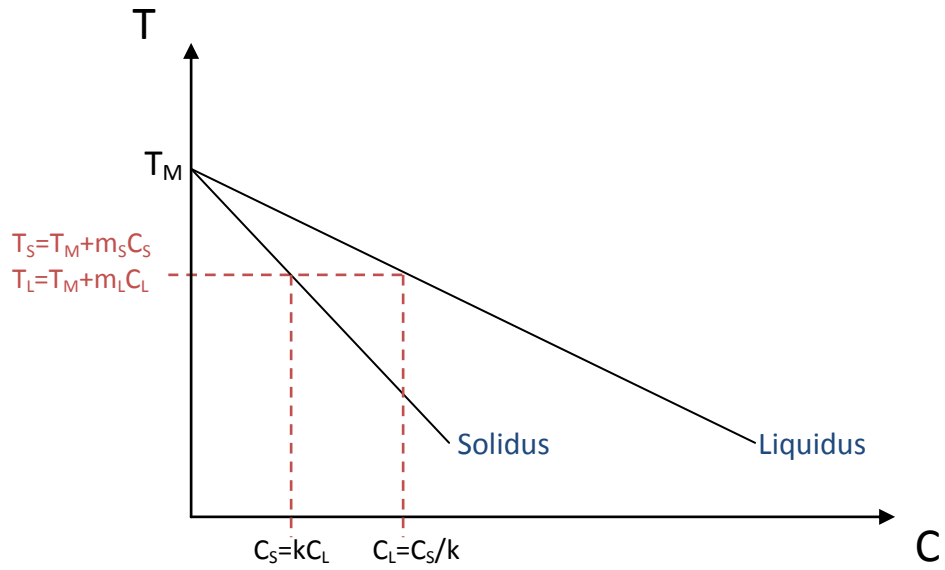

Figure 1.4 Typical phase diagram of a binary alloy system where $\boldsymbol{k} = \frac{\boldsymbol{m_L}}{\boldsymbol{m_S}}$ and m_S and m_L are gradient of solidus and liquidus lines, for this case, k<1.

The diffusion under-cooling, ΔT_d, is the under-cooling which results from the composition gradient of the liquid phase at the solid liquid interface, and can be represented as,

$$\Delta T_d = m(C_{l\infty} - C_{lr}) \qquad \textbf{1.22}$$

m is the liquidus gradient, $C_{l\infty}$ is the liquid composition at planar surface, C_{lr} is the liquid composition at curved surface

A typical binary alloy phase diagram is shown in figure 1.4, to show the temperature on the phase diagram is dependent on the concentration of solute.

For pure materials and multi component materials that are in equilibrium condition, the value $\Delta T_d = 0$, thus the total under-cooling is mathematically equal to the curvature under-cooling term, i.e. $\Delta T_d = \Delta T$.

The remaining term ΔT_r, is the curvature under-cooling which accounts for the surface energy that is present at the solid liquid interface and this term is also known as the Gibbs Thomson effect. This curvature under-cooling term is used to calculate the solid liquid surface energy, σ_{SL}, for binary alloys using the curvature of the interface and also the weighted entropy of fusion.

To derive the curvature under-cooling term, ΔT_r, the following concept needs to be considered, which are, the solid liquid surface energy, the driving force and the Gibbs free energy and equilibrium.

1.8 Driving Force

This driving force for solidification is the change in Gibbs free energy and this is the energy which drives solidification. This force can be derived if we consider the region in Figure 1.3 between temperatures T_m-ΔT and T_m, and the lines G_{solid} and $G_{liquid}$and the values of entropy and enthalpy do not vary over this temperature range. This gives,

$$\Delta G = G_S - G_L = H_S - H_L - T(S_S - S_L) = \Delta H - T\Delta S \qquad 1.23$$

However, at the equilibrium melting temperature, T_m, the Gibbs free energy for both solid and liquid phase will be equal i.e. G_L=G_S, which means that $\Delta G = 0$. Thus,

$$\Delta S = \frac{\Delta H}{T_m} = \frac{L}{T_m} \quad \textbf{1.24}$$

L is the latent heat of fusion ($= \Delta H$), heat given off or taken in by a substance during a phase change

And using the above equation, the change in Gibbs free energy which is the thermodynamic driving force for phase transformation, can be expressed as,

$$\Delta G \cong L - \frac{LT}{T_m} = \frac{L\Delta T}{T_m} = \Delta T \Delta S \quad \textbf{1.25}$$

1.9 Determination of solid-liquid interfacial free energy

A flat solid liquid interface has an interfacial energy, but when the solid liquid interface is curved, an additional energy term σ_{SL} is needed to form the curved solid-liquid interface, which represents the solid liquid surface energy. An equation for this surface energy term related to curvature undercooling can be derived if the conditions for mechanical equilibrium and chemical equilibrium at the curved interface are combined together.

The chemical potential, which is the change in free energy of the whole system, needs to be determined in order to understand the condition of chemical equilibrium. This chemical potential is,

$$\mu_i = \left(\frac{\partial G_i}{\partial n_i}\right)_{T,P,n_j} \quad \textbf{1.26}$$

μ is chemical potential i.e. molar free energy, i and j are components

In relation to the bulk phase properties, in a single component system, the change in the Gibbs free energy value of the system which arises from the addition of one mole of component i at constant pressure and temperature is equal to the chemical potential of component i, i.e. $\Delta G = \mu_i$. This shows that the change of Gibbs free energy of the single component system is the molar free energy of component *i*, and thus,

$$g_i = \mu_i \quad \textbf{1.27}$$

$g$is the change of Gibbs free energy of a single component system

It can be assumed that the chemical potential the phases on either side of the curved interface are equal if it is in metastable equilibrium. And this is given as,

$$\mu_{isr} = \mu_{il\infty} \; (\mu_{ilr} = \mu_{il\infty}) \quad \textbf{1.28}$$

Unlike the equal pressure of both solid and liquid phase on planar solid liquid interface, the pressure from the solid phase side of the curved solid liquid interface are greater than the other liquid phase side due to the tension produced by the surface. If we neglect the transfer of material and just look at the mechanical equilibrium, it gives,

$$(P_S - P_L)dV = \sigma_{SL} d\varphi \qquad \textbf{1.29}$$

P is the pressure, dV is the volume change due to curvature effect, $d\varphi$ is the surface area change due to curvature effect

If the curved interface is assumed to be a shape of a sphere, this means that $\frac{d\varphi}{dV} = \frac{2}{r}$, and thus,

$$\Delta P = \frac{2\sigma_{SL}}{r} \qquad \textbf{1.30}$$

1.10 Solid liquid surface energy for pure materials

To find the solid liquid surface energy for pure materials, first, molar volume is expressed using equation 1.28. And this is,

$$\left(\frac{\partial g}{\partial P}\right)_T = \left(\frac{\partial \mu}{\partial P}\right)_T = V \tag{1.31}$$

And the change in molar free energy between the phases for a pure incompressible material can be deduced by using equation 1.30 and 1.31. They are,

$$\Delta g = g_{Sr} - g_{L\infty} = \int_{P_L}^{P_s} V\, dP \tag{1.32}$$

$$\Delta g = \Delta P V = \frac{2\sigma_{SL}}{r} V \tag{1.33}$$

And also using equation1.25,

$$\Delta g = \Delta T_r \Delta S = \Delta T_S \Delta S \tag{1.34}$$

From the equation 1.33 and 1.34, the solid liquid surface energy term relating to the curvature under-cooling for pure materials can be deduced as follows,

$$\Delta T_r = \frac{2\sigma_{SL}}{r\Delta S} V_s \qquad 1.35$$

1.11 Solid liquid surface energy for binary alloys

To find the solid liquid surface energy for binary alloys, it is not as easy as the average change in Gibbs free energy is the function of the solid and liquid composition for both phases as can be seen by black lines in Figure 1.5. At the solid liquid interface, the temperature and the chemical potential must be the same throughout the alloy to reach the equilibrium condition. If we consider a binary alloy with phases A and B, the Gibbs free energy is given as,

$$G = n_A\mu_A + n_B\mu_B \qquad 1.36$$

n is the number of atoms, μ is the chemical potential

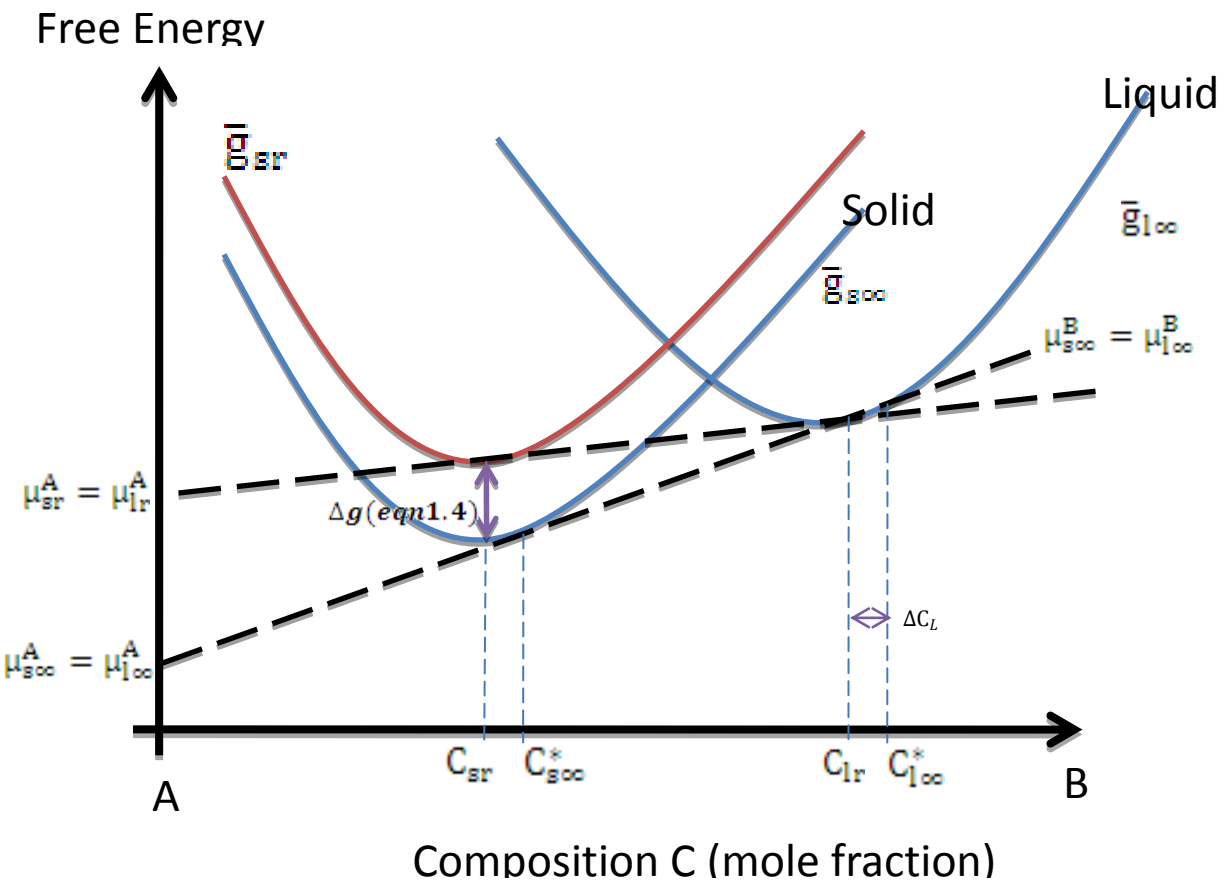

Figure 1.5 Free energy verses composition for a binary alloy [7]

The red line in the Figure 1.5 above represents the average free energy per atom, $\overline{g_{sr}}$ which shows the curvature effect of a binary alloy. The chemical potential of a given composition of a phase is given by the tangential line drawn and the intercept on either A or B axis. As seen in Figure 1.5, the equilibrium for two phases occur when both A and B have a common tangential line. The red line drawn is to make the curved interface to be in the metastable equilibrium state and this line is the $\overline{g_{s\infty}}$ line that has been shifted up at the same composition. The metastable equilibrium occur when a new common tangential line is drawn between the red line and the liquid phase line and this will give $\mu_{sr}^{A} = \mu_{Lr}^{A}$ and $\mu_{sr}^{B} = \mu_{Lr}^{B}$ for the compositions C_{sr} and C_{Lr} .

Thus the change of molar free energy of a spherical solid at steady composition caused by the curvature effect can be expressed using equation 1.37 as follows,

$$\left(\frac{\partial g}{\partial P}\right)_{T,n_A,n_B} = n_A\left(\frac{\partial \mu^A}{\partial P}\right)_{T,n_A,n_B} + n_B\left(\frac{\partial \mu^B}{\partial P}\right)_{T,n_A,n_B} \quad \textbf{1.37}$$

$\left(\frac{\partial \mu_s^A}{\partial P}\right)_{T,n_A,n_B} = V_s^A$ *and* $\left(\frac{\partial \mu_s^B}{\partial P}\right)_{T,n_A,n_B} = V_s^B$ *are the partial atomic volumes*

And by using this equation 1.38, the Gibbs free energy can be deduced as,

$$\Delta g = n_A \int_{P_L}^{P_s} V_s\, dP + n_B \int_{P_L}^{P_s} V_s\, dP \quad \textbf{1.38}$$

This is,

$$\Delta g = (n_A V_s^A + n_B V_s^B)\Delta P \quad \textbf{1.39}$$

And thus for a spherical solid that is incompressible, using equation 1.36, this gives,

$$\Delta g = \frac{2\sigma_{SL}}{r} V_S \qquad 1.40$$

Where $n_A V_s^A + n_B V_s^B = V_s$

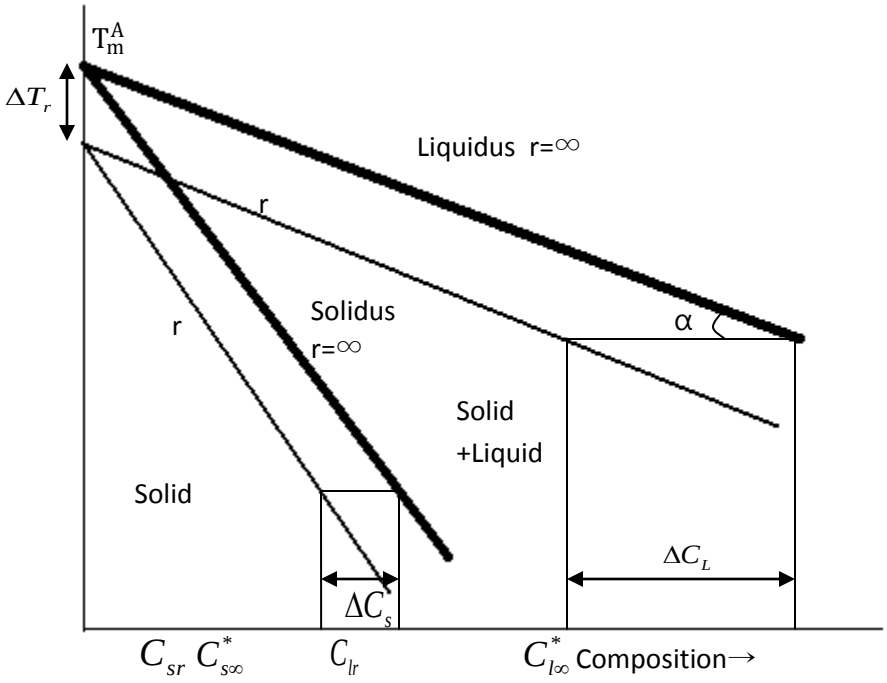

Figure 1.6 Depression of equilibrium condition caused by the Gibbs Thomson effect on binary alloy [7]

The curvature under-cooling ΔT_r, can be expressed as a function of solid liquid surface energy σ_{SL}, gradient of liquidus slope m_l, composition of both phases, principal radius *r* and equilibrium temperature *T*, by referring to Figure 1.5 and Figure 1.6. By looking at the area

between two tangential lines in Figure 1.5, it is shown that, $\Delta C_L = C_{lr} - C_{l\infty}$ and for small changes in ΔC_L and assuming the triangle area under free energy diagram in figure 1.5 are similar, it is approximated,

$$\frac{\mu_{sr}^{A} - \mu_{s\infty}^{A}}{\overline{g_{sr}} - \overline{g_{s\infty}}} = \frac{\Delta G}{\Delta g} = \frac{1 - C_{L\infty}}{C_{s\infty} - C_{L\infty}} \qquad \textbf{1.41}$$

Where $\mu_{sr}^{A} - \mu_{s\infty}^{A}$ is the chemical potential difference between a curved and flat interface, and $\overline{g_{sr}} - \overline{g_{s\infty}}$ are the equilibrium concentrations of solid and liquid phases for a flat interface.

For binary system of A and B, the chemical potential energy of A at constant pressure and temperature can be given as

$$\mu_A = \mu_0 + kT \ln a \qquad \textbf{1.42a}$$

μ_0 is the chemical potential of pure A, k is the gas constant, a is the activity where it is the activity coefficient times the concentration of A

If the activation coefficients are considered at steady pressure and temperature, ΔG is given,

$$\Delta G = \Delta\mu = kT \ln\left(\frac{\gamma_{Lr} C_{Lr}}{\gamma_{L\infty} C_{L\infty}}\right) \qquad \textbf{1.42b}$$

$\gamma_{L\infty}$, γ_{Lr} are the activation coefficients

If the activation coefficients are assumed to be constant over the considered composition range, ΔC_L is small magnitude and therefore approximated and it is,

$$ln\left(\frac{C_{Lr}}{C_{L\infty}}\right) = ln(1 + \frac{\Delta C_L}{C_{L\infty}}) \cong \frac{\Delta C_L}{C_{L\infty}} \quad \textbf{1.43a}$$

That means,

$$\Delta G = kT\frac{\Delta C_L}{C_{L\infty}} \quad \textbf{1.44b}$$

Combining the three equation 1.41, 1.42, 1.43 together gives,

$$\Delta C_L = \frac{2\sigma_{SL}}{rkT} V_S \frac{(1 - C_{L\infty})\, C_{L\infty}}{(C_{s\infty} - C_{L\infty})} \quad \textbf{1.45}$$

It can be noted that for small changes, $\Delta T_r = \Delta C_l \tan(\alpha)$, where $\tan(\alpha) = m$, where m is slope, thus giving, $\Delta T_r = m\Delta C_l$ which gives,

$$\Delta T_r = \frac{2\sigma_{SL} m\, V_S}{rkT} \frac{(1 - C_{L\infty})}{(C_{s\infty} - C_{L\infty})} C_{L\infty} \quad \textbf{1.46}$$

The change in atomic molar free energy for an incompressible spherical solid is given as, $\bar{g}_{sr} - \bar{g}_{s\infty} = \Delta g = \frac{2\sigma_{SL}}{r} V_S$, and this change in atomic molar free energy term can be represented as,

$$\bar{g}_{sr} - \bar{g}_{s\infty} = \Delta g = \frac{2\sigma_{SL}}{r} V_S = \int_{T_\infty}^{T_r} \Delta S^* \, dT + kT_\infty \Delta C_L \frac{(C_{s\infty} - C_{L\infty})}{(1 - C_{L\infty})\, C_{L\infty}} \quad \textbf{1.47}$$

$V_S = (1 - C_{s\infty})V_s^A + C_{s\infty}V_s^B$ *is the atomic volume of the solid,*

$\Delta S^* = [(1 - C_{s\infty})(S_s^A - S_L^A) + C_{s\infty}(S_s^B - S_L^B)]$ *is weighted entropy change,*

T_∞ *is the equilibrium temperature,* T_r *is the curved interface temperature, K is Boltzmann's constant,*

ΔC_L *is the change in composition in the liquid phase at the interface due to curvature effect.*

Using equation 1.46, it can be deduced that the change in the liquid composition with interface radius r is the same as equation 1.45. If the ΔS^* term is assumed to be steady, and at constant composition of $\Delta C_L = 0$, the curvature under-cooling term is given by,

$$\Delta T_r = \frac{2\sigma_{SL}}{r\Delta S^*} V_S = \frac{2\sigma_{SL}}{r\Delta S_f^*} \quad \textbf{1.48}$$

$\Delta S_f^* = \left(\frac{\Delta S^*}{\Delta V_s}\right)$ *is the entropy of fusion per unit volume*

This is same as equation 1.35. Also this curvature under-cooling term can derived by using a theory called homogeneous nucleation theory and equations 1.46 or 1.48 can be used to compute the value for solid liquid surface energy, σ_{SL} for binary alloys.

The curvature under-cooling equation thus solid liquid surface energy has so far been discussed for pure and binary alloys that have isotropic surface energy and have spherical interfaces.

If the non-spherical surfaces are considered, the Figure 1.7 is used to aid in deducing an equation for the surface energy. The surface energy term is numerically equal to the surface tension, σ_{SL} and as previously mentioned is the work done to form a unit area of a surface. The diagram on the left of the Figure 1.7 show segment δθ of a cylindrical surface and due to the difference in pressure throughout the surface, the inward force F_1 and the outward force F_2 must be equal to each other so if $\delta\theta \rightarrow 0$, it will be,

$$\sigma_{SL}\delta\theta = \Delta P r \delta\theta \qquad \textbf{1.49}$$

Or

$$\Delta P = \frac{\sigma_{SL}}{r} \qquad \textbf{1.50}$$

The diagram on the right of Figure 1.6 shows the curvature of the surface in two directions with two principal radii, r_1 and r_2 and the change in pressure is given by,

$$\Delta P = \sigma_{SL}\left(\frac{1}{r_1}+\frac{1}{r_2}\right) \qquad 1.51$$

And this referring to equation 1.33, gives the change in chemical potential to be,

$$\mu_{sr} - \mu_{s\infty} = V_s \Delta P$$

that is

$$\Delta P = \sigma_{SL}\left(\frac{1}{r_1}+\frac{1}{r_2}\right)V_s \qquad 1.52$$

The $\left(\frac{1}{r_1}+\frac{1}{r_2}\right)$ term in the curvature undercooling equations obtained for the non-spherical solid liquid interface replaces $\frac{2}{r}$ term in the spherical interface equations.

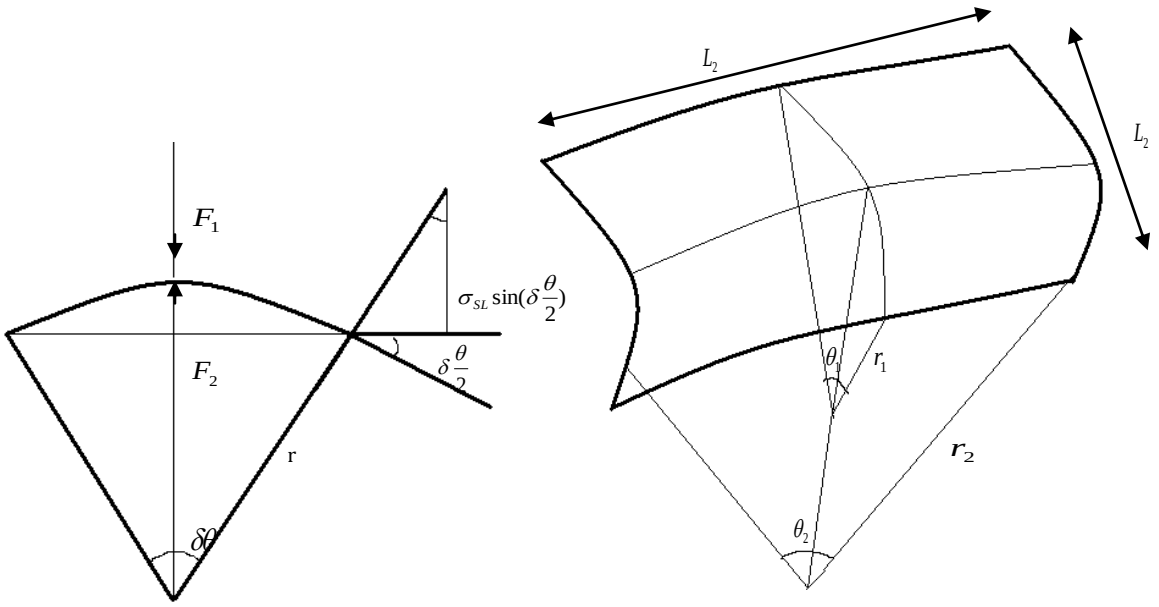

Figure 1.7 Representation of non-spherical surfaces used to calculate Gibbs Thomson equation [7]

When we consider crystallographic orientation effect on surface energy, if the atomic transportability is high to preserve the microscopic structure of the interface after the deformation, the value of surface energy is numerically equal to the surface stress and surface stress do not change with orientation.

The surface stress is the normal force across a small area of a boundary. However, with solid phase that has low atomic transportability over larger area of a boundary, it may not be possible to keep the local structure around a particular atom constant, in the region of surface where deformation has occurred. In this case, the crystallographic orientation effect needs to be taken into consideration when calculating surface tension. The surface energy term, σ_{SL} when it is a function of the crystallographic orientation, a couple is required to stop flat surface rotating into a lower energy position as shown in the diagram on the left of Figure 1.8. The work done in opposing the couple is,

$$W_1 = 2\,flh\,\delta\theta \qquad \textbf{1.53}$$

f is the force per unit length

This work done force W_1 should equal to the change in free energy of the surface,

$$W_2 = 2hl\frac{d\sigma_{SL}}{d\theta}\delta\theta \qquad \textbf{1.54}$$

And from equation 1.52 and 1.53,

$$f = \frac{d\sigma_{SL}}{d\theta} \qquad \textbf{1.55}$$

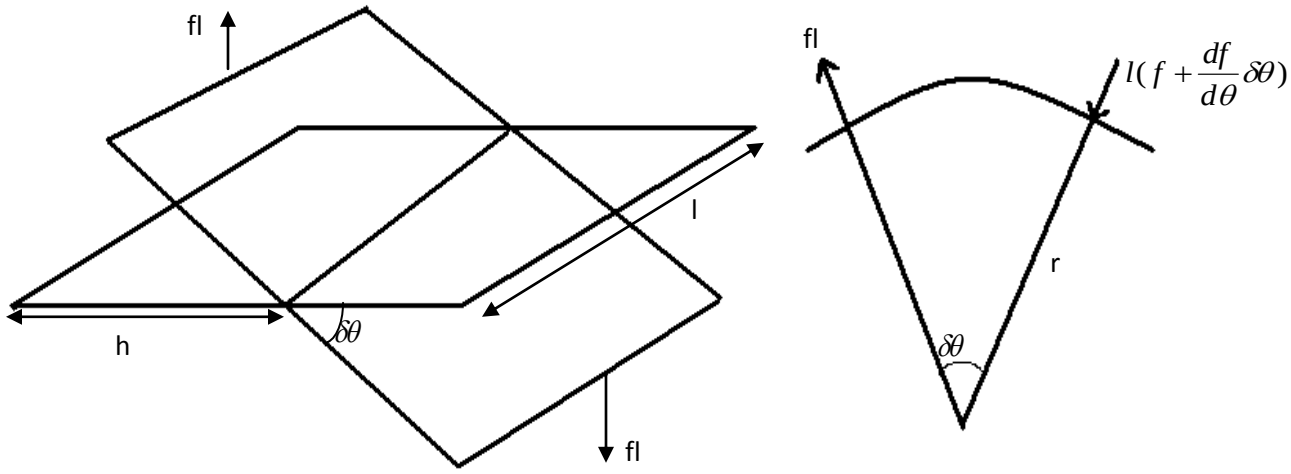

Figure 1.8Representation of diagrams for calculating crystallographic orientation effect [7]

In Figure 1.8, there is no net vertical force acting on the flat surface but for a curved surface shown on right diagram of Figure 1.8, the inward force is not equal to the outward force and there is a net inward force,

$$\Delta f = \frac{ldf}{d\theta}\delta\theta = \frac{ld^2\sigma_{SL}}{d\theta^2}\delta\theta \qquad 1.56$$

This net inward force is then added to the force from the surface tension, and equation 1.49 becomes,

$$\Delta P l r \delta\theta = \sigma_{SL} l \delta\theta + \frac{ld^2\sigma_{SL}}{d\theta^2}\delta\theta \qquad 1.57$$

Or

$$\Delta P = \frac{1}{r}(\sigma_{SL} + \frac{d^2\sigma_{SL}}{d\theta^2}) \qquad 1.58$$

Referring to the right diagram in the Figure 1.7, and take into consideration the curvature in two directions,

$$\Delta P = \frac{1}{r_1}\left(\sigma_{SL} + \frac{d^2\sigma_{SL}}{d\theta_1{}^2}\right) + \frac{1}{r_2}\left(\sigma_{SL} + \frac{d^2\sigma_{SL}}{d\theta_2{}^2}\right) \quad \textbf{1.59}$$

Using equation 1.51 and 1.58,

$$\mu_{sr} - \mu_{s\infty} = \Delta g = V_s \Delta P = V_s\left[\frac{1}{r_1}\left(\sigma_{SL} + \frac{d^2\sigma_{SL}}{d\theta_1{}^2}\right) + \frac{1}{r_2}\left(\sigma_{SL} + \frac{d^2\sigma_{SL}}{d\theta_2{}^2}\right)\right] \quad \textbf{1.60}$$

In the equation 1.59, if the term $\mu_{sr} - \mu_{s\infty}$is substituted into the equation 1.45, then the curvature undercooling term at constant temperature becomes,

$$\Delta T_r = \left[\frac{1}{r_1}\left(\sigma_{SL} + \frac{d^2\sigma_{SL}}{d\theta_1{}^2}\right) + \frac{1}{r_2}\left(\sigma_{SL} + \frac{d^2\sigma_{SL}}{d\theta_2{}^2}\right)\right]\frac{m\,V_S}{kT}\frac{(1 - C_{L\infty})}{(C_{s\infty} - C_{L\infty})}C_{L\infty} \quad \textbf{1.61}$$

At constant composition,

$$\Delta T_r = \left[\frac{1}{r_1}\left(\sigma_{SL} + \frac{d^2\sigma_{SL}}{d\theta_1{}^2}\right) + \frac{1}{r_2}\left(\sigma_{SL} + \frac{d^2\sigma_{SL}}{d\theta_2{}^2}\right)\right]\frac{V_S}{\Delta S^*} \qquad \textbf{1.62}$$

It can be seen from the above equations that when σ_{SL} is not a function of the crystallographic orientation, which means when it is isotropic, for non-spherical surface, the equations 1.60 and 1.61 becomes,

$$\Delta T_r = \frac{\sigma_{SL} m\, V_S}{kT}\frac{(1 - C_{L\infty})}{(C_{s\infty} - C_{L\infty})} C_{L\infty}\left[\frac{1}{r_1} + \frac{1}{r_2}\right] \qquad \textbf{1.63}$$

$$\Delta T_r = \frac{\sigma_{SL} V_S}{\Delta S^*}\left(\frac{1}{r_1} + \frac{1}{r_2}\right) \qquad \textbf{1.64}$$

And if the interfacial surface is spherical i.e. r_1 and r_2 are equal, equations 1.62 and 1.63 becomes equations 1.47 and 1.49 respectively.

The equation 1.63 is the most useful method for calculating the solid liquid interfacial energy at the equilibrated interface and as it shows the effective change in melting point at a curved surface, it is also useful for solidification and melting process. Also for a binary alloy system, both phases will be uniform and the composition difference will be zero at equilibrium. And thus equation 1.63 will be used to calculate σ_{SL}.

2 Literature Review of theExperimental Methods for Measuring Solid-Liquid Interfacial Energy

This chapter is a literature review, providing summary of some of the common methods that have been used in experimental measurement of solid-liquid interfacial energy, σ_{SL}. To experimentally determine solid-liquid interfacial energy for pure and multi component systems, there are two methods commonly used. Those methods are: from the measurement of dihedral angle method, and the direct application of Gibbs-Thomson equation.

2.1 The calculation of σ_{SL} from the measurement of dihedral angle

2.1.1 Equilibrium at three phase junction

One of the general methods used in measuring the surface tension is to study the configuration of boundaries where three interfaces intersect. The relative values of the surface tensions can be calculated by considering the angles of intersection of interfaces of the system that is in equilibrium.

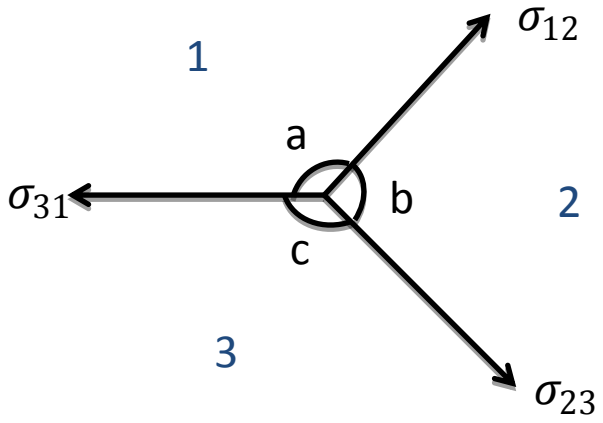

Figure 2.1. Showing surface tensions acting where the three interfaces between the phases 1,2 and 3 intersect

The simplest example of such intersection is shown in Figure 2.1, and in specific situations two of the phases may be the same, for example is solid-vapour interfaces where an interface could be a grain boundary in a solid and the other two phases could be of the same type.

For simplicity all the phases will be considered as simple fluids so that the σ are isotropic. In this case the surface tension can be equated to the surface free energy, and this can be the same for all methods of interface intersections.

For the simple case shown in Figure 2.1

$$\frac{\sigma_{12}}{\sin c} = \frac{\sigma_{23}}{\sin a} = \frac{\sigma_{31}}{\sin b} \qquad \textbf{2.1}$$

The relative values of surface tensions can be obtained by directly measuring the angles of the intersection of the interfaces. Therefore by knowing the absolute value of one of the surface tensions, the surface tensions of others can be determined. The equation 2.1 is only true when all the phases are liquid i.e. for isotropic interfacial energy.

For a case when a grain boundary intersects a solid liquid interface, the three phase junction is as shown in figure 2.2(a), and the equilibrium condition is given as

$$\sigma_{gb} = 2\sigma_{SL}\, cos\left(\frac{\theta_{SL}}{2}\right) \qquad \textbf{2.2a}$$

(a)

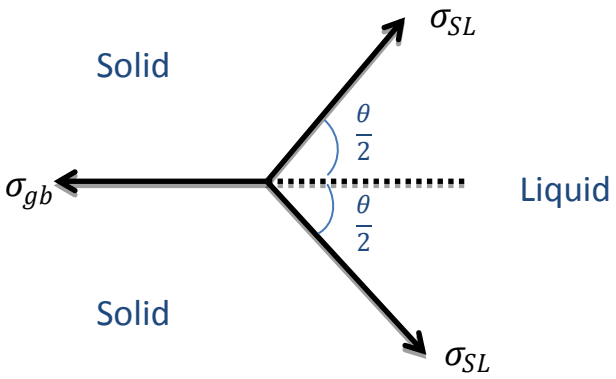

(b)

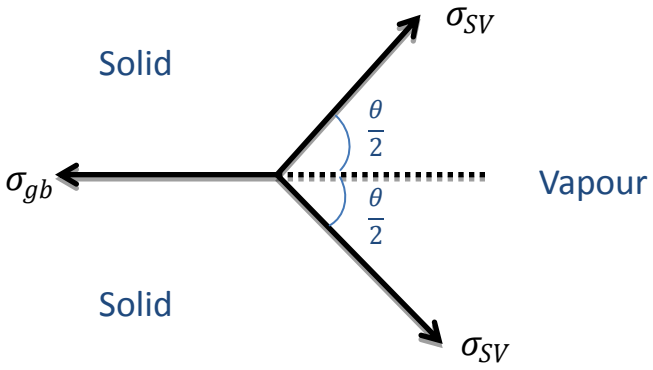

(c)

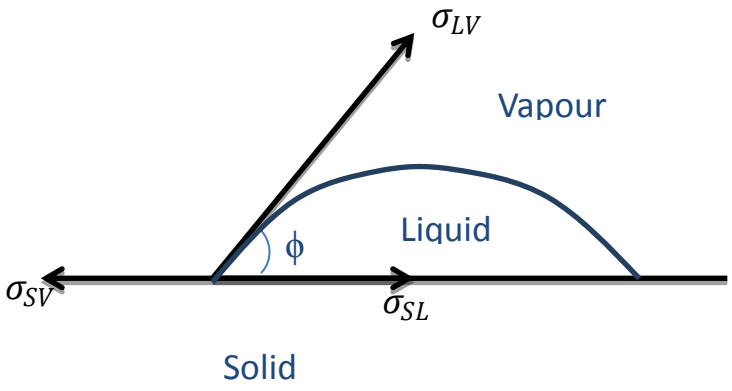

Figure 2.2. Schematic diagrams of three phase system for (a) solid-liquid system, (b) solid-vapour system, (c) solid-liquid-vapour system

And similarly the equilibrium condition for the solid vapour system shown in figure 2.2(b) is given as

$$\sigma_{gb} = 2\sigma_{SV}\, cos\left(\frac{\theta_{SV}}{2}\right) \qquad \textbf{2.2b}$$

For the solid-liquid-vapour system in equilibrium, the liquid droplet is placed on solid surface and this is shown in figure 2.2(c) and represented as

$$\sigma_{SV} = \sigma_{SL} + \sigma_{LV} cos(\phi) \qquad \textbf{2.2c}$$

Where σ_{gb}, σ_{SV}, σ_{LV}, and σ_{SL} are interface energies at the grain boundary, solid-vapour, liquid-vapour and solid-liquid interfaces respectively and the angles are shown in figure 2.2.

By using equations 2.2, the solid liquid interface energy, σ_{SL}, can be obtained for any suitable pure material in the case of high angle grain boundaries and when θ_{SV}, θ_{SL} and ϕ are measured and σ_{LV} is known. Ketcham and Hobbs used this principle to measure σ_{SL} for ice water system[8,10] of 33 ± 3 erg/cm^2 and the value obtained was smaller than the value obtained for the same system using other direct methods. Suzuki and Kuroiwa[9] has shown that the technique used by Ketcham and Hobbs was particularly sensitive to θ_{SV} and by giving an appropriate correction, the value of θ_{SL} could be improved to bring the result for the ice-water system closer to agreement with other direct measurements.

This method of using interface intersections is usually not applicable to solid-liquid interface study, however one example where this method is applied to solid-liquid interface study is a technique called 'sessile drop method', which observes the equilibrium shape of a liquid drop on a solid surface. For this system, the equilibrium is only achieved when the solid and liquid phases are in equilibrium with the vapour.

2.1.2 Sessile drop method

The recent experiments on using this sessile drop method are shown in the literatures by [11-17], and this method is briefly explained below.

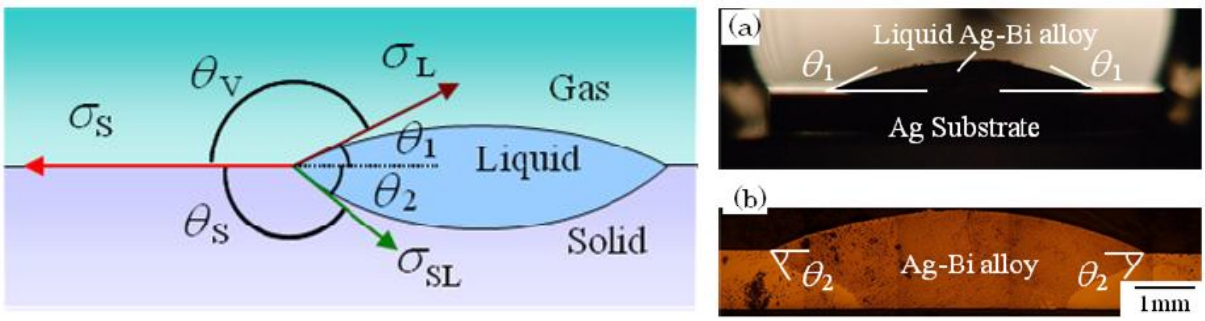

Figure 2.3. The left figure shows the schematic of the experiment set up and analysis, (a) The liquid Ag-Bi droplet on the solid Ag substrate and (b) the cross-section after the experiment [13]

The experiment is carried out by placing a liquid alloy droplet onto a substrate and by considering equilibrium at three phase junction. The equilibrium condition at the junction is shown as

$$\sigma_s = \sigma_L \cos\theta_1 + \sigma_{SL} \cos\theta_2 \qquad 2.3$$

And by using Dupre'sequation[18,19], it can be represented as

$$\frac{\sigma_{SL}}{sin\,\theta_V} = \frac{\sigma_L}{sin\,\theta_S} = \frac{\sigma_S}{sin(\theta_1 + \theta_2)} \qquad 2.4$$

Where σ_L is liquid surface tension, σ_S is the solid surface energy and σ_{SL} is the solid liquid interfacial energy

The solid liquid interfacial energy can be determined by obtaining the value of the liquid surface tension and measuring the dihedral angles of θ_V and θ_S.

This sessile drop method has been used to calculate σ_{SL} for Cu-B and Ag-Bi systems by Fukuda, Yoshikawa and Tanaka[13] of interfacial values of and $1440 \pm 17\mathrm{mN/m}$,and for Al-Si, Al-Al_2O_3 and Fe-C systems[20-22] of$182 \pm 23\mathrm{mN/m}$. In this method the σ_{SL} can change as the alloy droplet changes its composition during the experiment.

The classical method of measuring the contact angle to calculate surface free energy has some limitations, and in the case of a confined or a large surface, it is impossible to measure the contact angle. Also as the sample surface is not always horizontal, there is a need to identify an algorithm to measure the surface energy.

The validity of the technique is also questionable as when measuringθ_{SL}, the grain boundary often is highly contaminated by the liquid phase and the σ_{gb} term cannot be eliminated in the equation 2.2. Also θ_{LV} is hard to distinguish and due to the contamination of the solid phase from the liquid droplet, σ_{SV} is not necessarily constant. The accuracy of the interface value obtained by the sessile drop method is highly dependent on the droplet profile and the geometrical anisotropy of the interface.

2.1.3 Dihedral angle method

Another method which uses interface intersection method described above is the study of dihedral angle of the equilibrium structure of a grain boundary which emerges at the solid, shown in figure 2.4. This method has been used to measure surface free energies in pure metals and alloys and also to evaluate relative magnitudes of grain boundary. The experiment is carried out by directly observing the two phases in equilibrium by observing thin films of the metal using transmission electron microscopy and studying the solid-liquid interface intersection that have low angle tilt grain boundaries of free energy less than $2\theta_{SL}$.

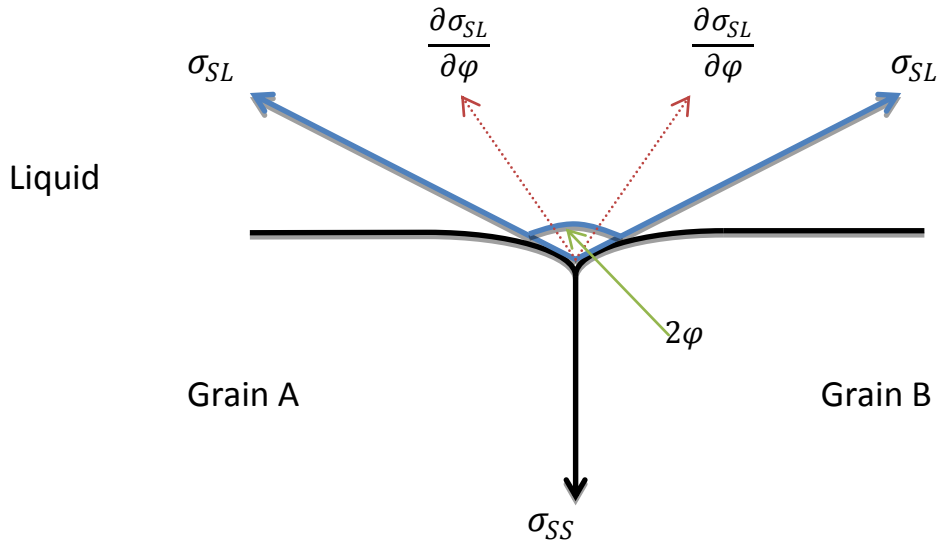

Figure 2.4. Schematic of the forces acting in the groove at the intersection of a symmetrical boundary

This method was used by Glicksman and Vold[23,24] to measure solid-liquid interfacial energy of bismuth of values $61\ \mathrm{erg/cm^2}$. The specimen was made with a thin (2000 Angstrom) vapour deposited film of bismuth in between thin carbon films, which was mounted on the hot stage of an electron microscope. The sample was prepared this way so that a radial temperature with the highest temperature at the centre was imposed on the specimen in the region of field of view. The symmetrically tilted low angle grain boundaries intersecting the solid-liquid interface will form cusp-like depressions and by measuring the angles of the cusp, the solid-liquid

interfacial energy can be calculated. In figure 2.4, can be applied to all boundaries not only tilt boundaries but by choosing symmetrical tilt boundaries, the torque terms for the solid-solid interface can be eliminated and the equilibrium can be represented as,

$$\sigma_{SS} - 2\sigma_{SL}cos\varphi - 2\frac{\partial\sigma_{SL}}{\partial\varphi}sin(\varphi) = 0 \qquad 2.5$$

In the experiments, the dihedral angle of the groove in the solid-liquid interface, 2φ, and the tilt angle of the solid-solid boundary θ, were measured. The solid-liquid interfacial energy can be deduced by calculating the σ_{SS} from free energy of edge dislocations in the solid.

This method is not common due to the experimental difficulties. Many materials globulate or rapidly evaporate at elevated temperature, especially under high vacuum condition in the electron microscope. More fundamentally, it is difficult to obtain grain boundary without mis-orientation. Thus this method cannot be applied to alloys due to the fact that alloys usually have high tilt boundaries as a result of segregation effects at the grain boundary.

2.2 Direct application of the Gibbs Thomson equation

A more powerful method of experimentally measuring σ_{SL} is based on the direct application of the Gibbs Thomson equation. The Gibbs Thomson equation is obtained by combining the condition of chemical equilibrium and the condition of mechanical equilibrium of a curved interface. For the case when all other intensive variables such as pressure, composition and strain energy remains constant, a solid bounded by interface with principal radii of curvature r_1 and r_2 will be in equilibrium with its liquid at a temperature T_r, which is not equal to the liquidus temperature in the phase diagram, T_m. The Gibbs Thomson for this can be written as

$$T_m - T_r \equiv \Delta T_r = \frac{\sigma_{SL}}{\Delta S_f}\left(\frac{1}{r_1} + \frac{1}{r_2}\right) \quad \textbf{2.6}$$

Where ΔT_r is curvature undercooling and ΔS_f is the entropy of fusion per unit volume.

The solid liquid interfacial energy,σ_{SL} can be measured if the value of ΔT_r is measured for known r_1 and r_2 and ΔS_f is independently calculated. The assumption that is taken when using the equation 2.6 is that this applies when the interfacial energy is isotropic, and does not consider anisotropy of the interfacial energy, as most of the literature use this assumption when experimentally applying Gibbs Thomson equation, more future work is needed to take into account the anisotropy.

Although this is the most commonly used method, there still are several practical difficulties in using the Gibbs Thomson equation. When a single solid crystal is surrounded by its liquid at the equilibrium temperature, the equilibrium condition is very unstable as small fluctuations in temperature can cause either complete melting or solidification. Thus it is very difficult to obtain equilibrium condition and also the temperature control is very difficult. For the case where r_1 and r_2 are small (≤0.1µm) and large ΔT_r values (a few ℃), the intensive variable do not need careful control but the surface forces from the container my effect σ_{SL} due to the small r values.

In the case where r_1 and r_2 are large (≥0.1µm) the surface forces are not important but as ΔT_r values are small (≤0.1 ℃), the temperature needs to be controlled to high degree accuracy. The following techniques were attempted to overcome these difficulties.

2.2.1 Skapski's method

The first successful method used to measure σ_{SL} by direct application of the Gibbs Thomson equation was carried out by Skapski, for transparent materials such as acids, benzene$22 \pm 2\ \mathrm{mJ/m^2}$ and ice water system$44 \pm 10\ \mathrm{mJ/m^2}$[24-27].$\Delta T_r$, r_1 and r_2 are measured by setting up a wedge shaped apparatus to observe the capillary effect. The schematic of the setup of this apparatus is shown in Figure 2.5 and this gives a stable temperature even with small fluctuations in temperature. When the temperature of the system decreases, the solid will grow so the curvature of the solid liquid interface will increase to restore the equilibrium as shown in equation 2.6 and similarly for small increase in temperature. This means that there should be no temperature gradient and the temperature must be very stable.

The Skapski et al[26] then employed a tapering capillary cylinder to eliminate the liquid vapour meniscus. The presence of this meniscus can cause the solid liquid system to have less than one atmosphere and this could lead to a related change in T_m. The schematic of this setup is shown in Figure 2.6 and has a transparent tapering cylinder to allow r_1 and r_2 to be measured directly. The downside to this Skapski's method is that it can only be applied to pure materials. For impure materials, impurities tend to segregate into the thin part of the wedge and tapered cylinder causing it to have lower melting points thus leading to an error in ΔT_r and subsequently in σ_{SL}.

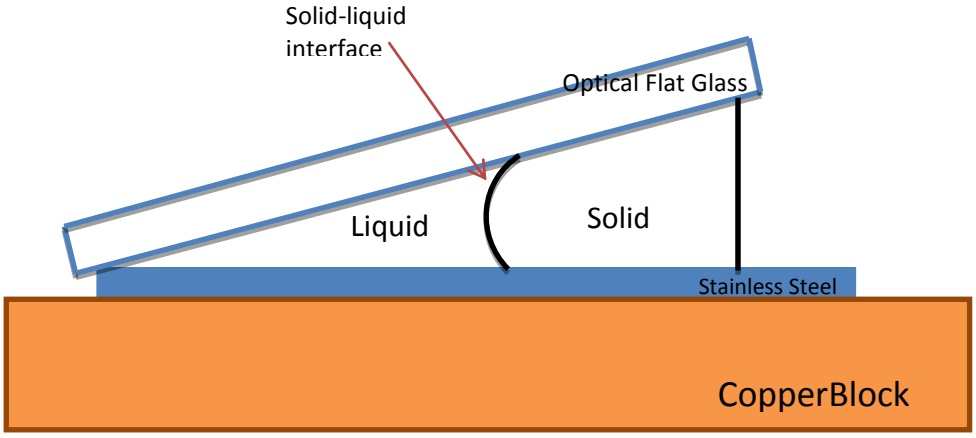

Figure 2.5. The wedge shape set up used by Skapski

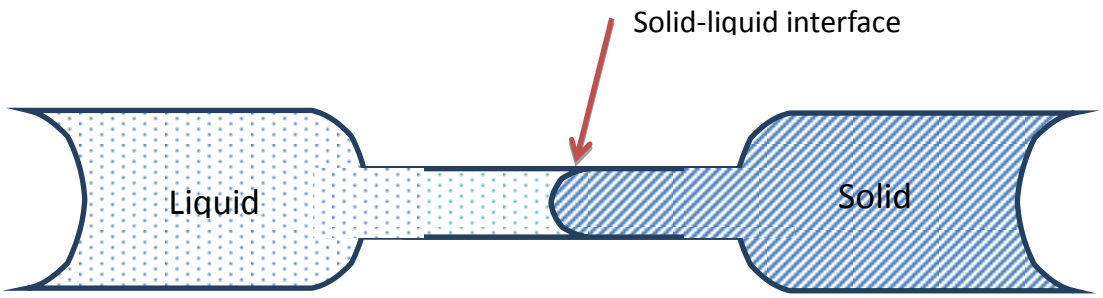

Figure 2.6. The tapered cylinder set up by Skapski [26]

2.2.2 The melting point of small crystals

Another method of applying the Gibbs Thomson equation is the measurement of the melting point of small crystals. A small solid crystal is heated and the melting occurs at the solid-vapour interface, and a thin skin of liquid surrounds the solid. The equilibrium condition is achieved when the liquid skin surrounding the solid has a critical thickness, so that it can be considered to have the properties of its bulk phase. If σ_{SL} is isotropic, for solid-liquid interface of a small solid crystal at equilibrium, the Gibbs Thomson equation can be written as

$$T_m - T_r \equiv \Delta T_r = \frac{2T_m}{L}\left[\frac{\sigma_{SL}}{\rho_S(R-t)} + \frac{\sigma_{LV}}{R}\left(\frac{1}{\rho_S} - \frac{1}{\rho_L}\right)\right] \qquad 2.7$$

Where $\rho_S$and ρ_L are the densities of the solid and liquid phases, t is the critical thickness of liquid and R is the initial radius of the solid

The experimental studies using this method have been carried out by Wronski[28] for tin, $62 \pm 10\ \mathrm{mJ/m^2}$, Kanig[31] for naphthalene, $69\ \mathrm{mJ/m^2}$, Sambles[30] for gold, $270 \pm 10\ \mathrm{mJ/m^2}$ and Coombes [29] for bismuth and lead, $40.7 \pm 7\ \mathrm{mJ/m^2}$, by observing the melting point depressions of small crystals. The experiments were carried out by forming small crystals of metal or bismuth (usually 10 to 100nm in size) on carbon or silicon monoxide substrate by vapour deposition in vacuum. The start of melting was detected either by measuring the changes in the rate of evaporation or by electron diffraction. The equation 2.7 was found to be

appropriate for the above metals but not bismuth. This method has major source of uncertainty in that it assumes the melting occurs by uniform melting.

Kubelka and Prokscha[32] attempted to measure σ_{SL} using related method, by measuring the depression of the melting point of solid benzene, ice and ethylene dibromide absorbed in porous media for example silica gel. Puri and his colleagues[33, 34] also used this method for similar experiments. Jones later recalculated σ_{SL} for benzene from their data[35].

However, this method was found to be unreliable in that firstly, the value of σ_{SL} obtained for a given material varied from experiment to experiment, secondly, the setup has one end of capillary closed, which alters the vapour pressure considerably and thus the R values may be in error. Lastly the surface forces on material adsorbed in a capillary may have a very large effect on the result.

2.2.3 The grain boundary groove shape in a temperature gradient

In recent experiments to measure the solid-liquid interfacial energy, the most common and powerful method considered to be used are the grain boundary groove shape in a temperature gradient method. The solid-liquid interface is obtained by equilibrating with a grain boundary in a temperature gradient, and the solid-liquid interfacial energy σ_{SL} can be calculated by observing the equilibrium shape of the grain boundary groove profile. The grain boundary groove shape is formed at the intersection where planar grain boundaries meet with planar solid-liquid interface, in an applied temperature gradient. The groove curvature becomes zero at large distance away from the grain boundary groove and thus the interface becomes planar. According to the Gibbs Thomson equation, the groove curvature towards the root of the groove increases to balance the decrease in interfacial temperature (increasingΔT_r). Near the grain boundary groove, the local curvature is $\frac{1}{r} = \frac{1}{r_1} + \frac{1}{r_2}$ where r_1 and r_2 are the principle radii of curvature. When considering a planar grain boundary intersecting a planar solid-liquid interface, $r_2 = \infty$ and the remaining curvature $\frac{1}{r_1}$ is related to the curvature undercooling

temperaturewhich is the temperature difference ΔT from the zero curvature temperature. From chapter1 the Gibbs Thomson equation is given as

$$T_{(\infty,0)} - T_{(x,y)} \equiv \Delta T_r = \frac{\sigma_{SL}}{\Delta S_f r_{(x,y)}} \quad \textbf{2.8}$$

Where ΔS_f is the entropy of fusion per unit volume

The equilibrium grain boundary groove shape in an applied temperature gradient was calculated by Bolling and Tiller[36] for $K_S = K_L$ and calculated by Nash and Glicksman[37] for $K_S \neq K_L$ where K_S is the thermal conductivity of solid and K_L is the thermal conductivity of liquid. This was observed experimentally by Singh and Glicksman[38], Jones[39,40], Jones and Chadwick[41, 42], Nash and Glicksman[37], Schaefer et al[43] and Hardy[44] for transparent organic materials in situ. And Gündüz and Hunt[45, 46] for binary alloys.

There are 3 experimental set up that is mainly used and the three are as follows.

2.2.3.1 Bridgman type apparatus

It is similar to directional solidifying apparatus where the crucible is held in a furnace with cooling jacket placed below the furnace. The crucible is placed on a holder and it has a central hole where the thermocouples are placed in a sheath and the thermocouples can descend into the cooling jacket by a motor. The liquid metal is poured into the crucible and the thermocouples placed in the crucible. The grain boundary groove can be achieved when the specimen is directionally grown by turning the motor on to draw liquid alloy. This apparatus is also used to measure the thermal conductivity ratio of the liquid phase. When the thermocouples descend by the motor, the temperature change over the time can be recorded and the thermal conductivity ratio can be obtained. The schematic diagram of this apparatus and the thermal conductivity ratio curve is shown below. [47-50]

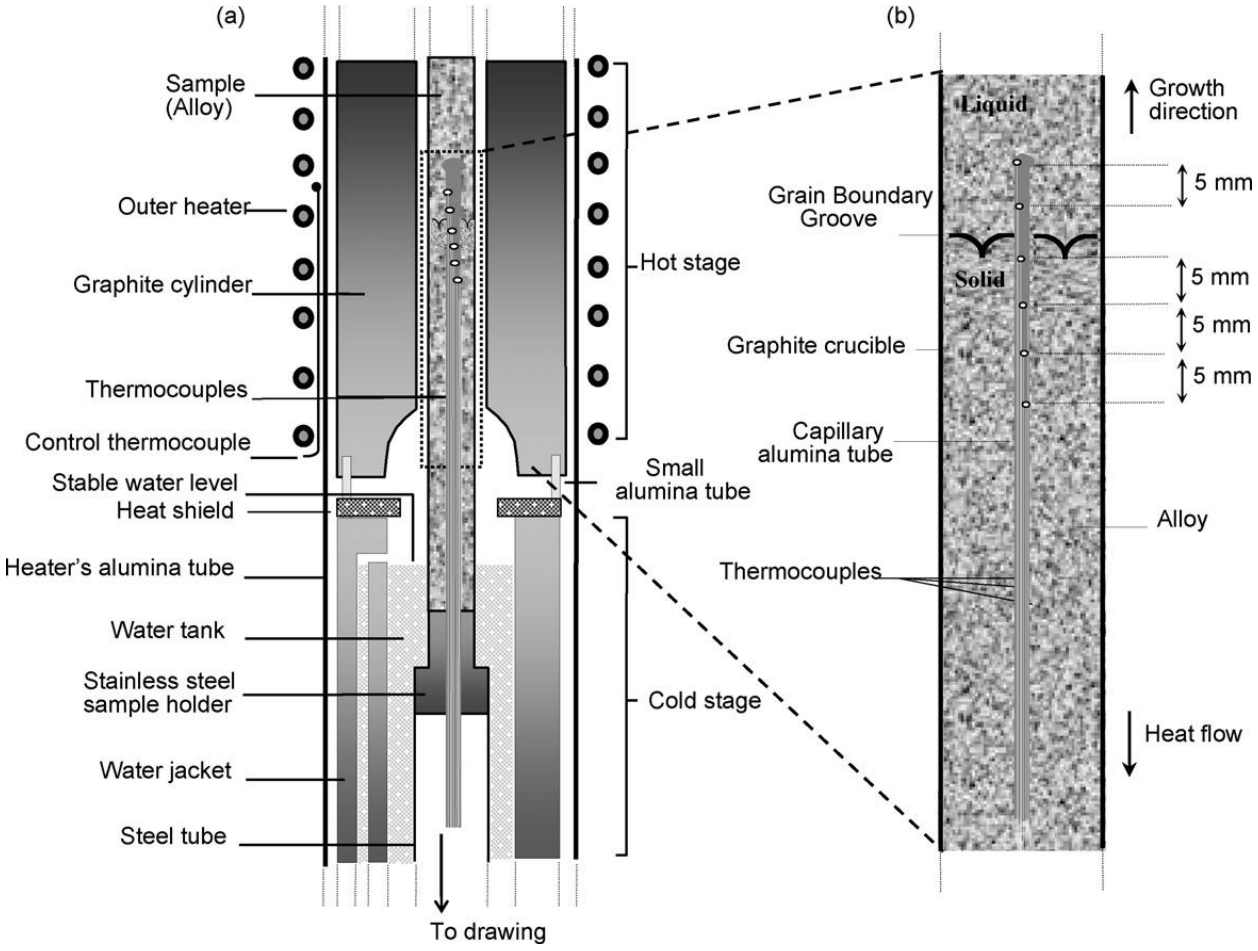

Figure 2.7 Schematic diagram of Bridgman type apparatus[47]

By recording the cooling rate, the thermal conductivity ratio value can be obtained as shown below

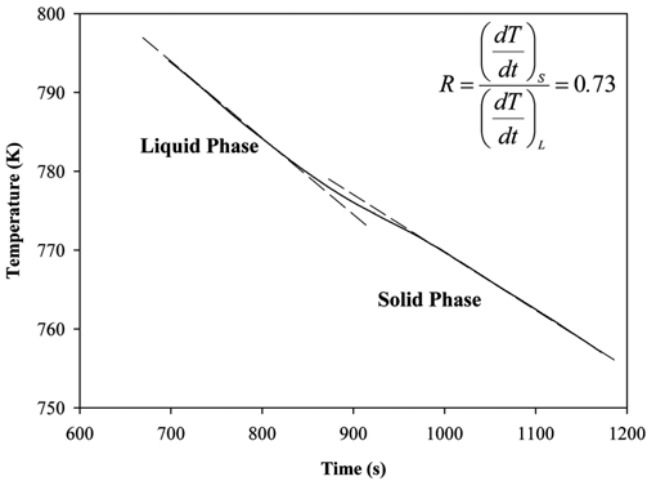

Figure 2.8 an example of the cooling rate curve of liquid and solid phase of an alloy [47]

2.2.3.2 Horizontal temperature gradient apparatus

Bayender [51] used this horizontal temperature gradient method. The equilibriated grain boundary groove can be obtained for transparent alloys as well as the organic materials. The molten sample is placed between thin plates of glass where the glass plate is then placed on a horizontal temperature gradient, with one end the heating system and the other end the cooling system to provide the temperature gradient. This method can directly observe the grain boundary groove shape. However this method has the limitations of only being able to operate in low to medium temperature. Also the preparation of the sample is difficult. [52-64]

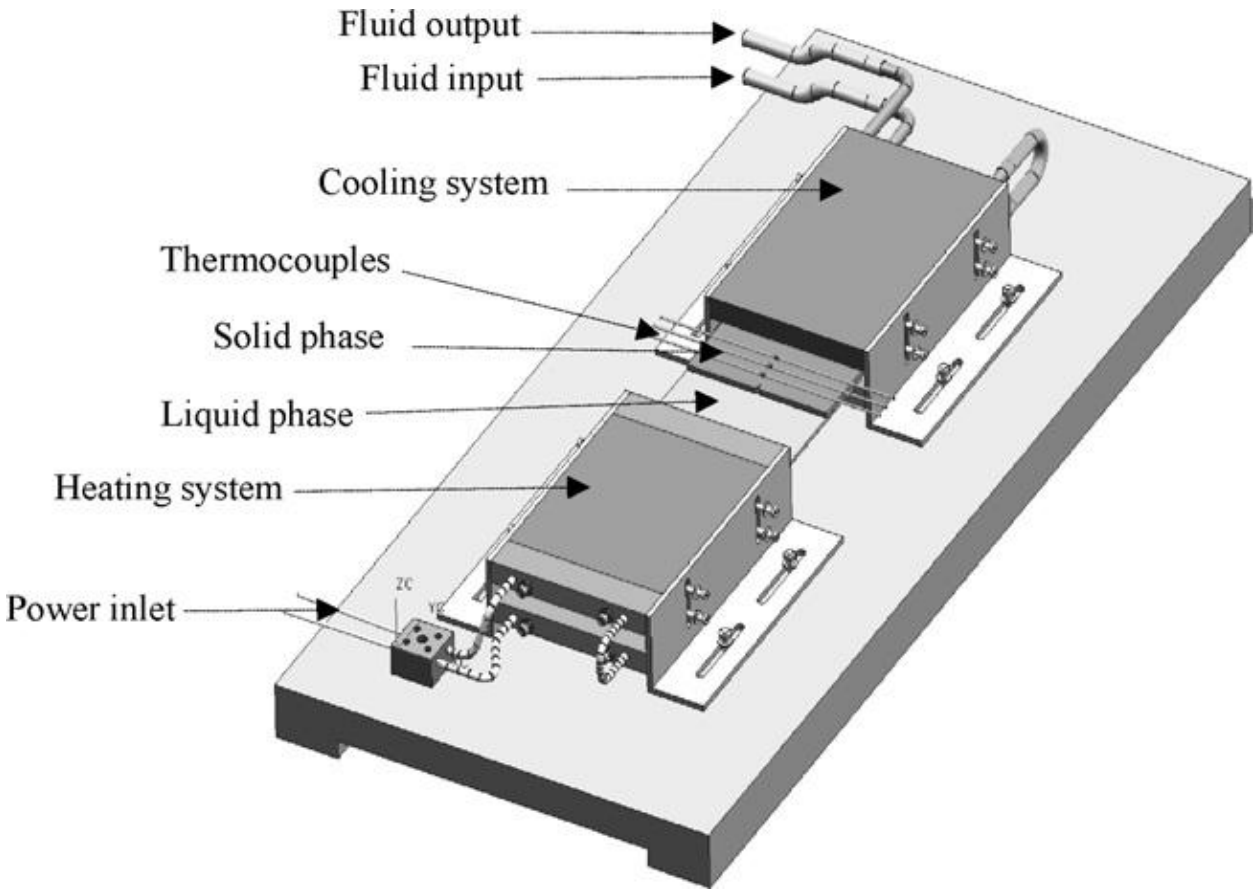

Figure 2.9. Schematic of the horizontal temperature gradient apparatus [51]

2.2.3.3 *Radial heat flow apparatus*

This is the most commonly used set up to measure the solid liquid interfacial energy and the more detailed set up will be discussed in the next chapter.

By reviewing the papers over the last decade, it is clear that the Radial heat flow apparatus is the most used set up as this provides higher temperature application and also provides radially symmetric crucible which enables also the measurement of thermal conductivity of the solid phase. [65-75]

The radial heat apparatus being introduced in the report has been modified to have the main crucible body made of alumina to prevent alloy reacting with the container, and this alumina crucible body will allow the crucible to withstand higher temperature. The main crucible has

been shortened to as this would mean having a shorter central heating element, as the heating element is more likely to burn out if the length is too long.An electromagnetic shielding will be built to reduce the error in temperature control and measurement by protecting thermocouples from picking up noise signals.

2.3 Calculation of solid-liquid interfacial energy from classical nucleation theory

The concept of solidification can be understood by two phenomena, which are nucleation and growth of crystals from its melt. When the temperature of liquid is lowered below its equilibrium liquidus temperature, T_m, the solid becomes the thermodynamically stable form and the liquid starts to transform into solid. This change of state corresponds to a reduction in total free energy ΔG which is a combination of volume free energy and the solid-liquid interfacial energy. The state which has lower free energy is the stable state and this is represented in Figure 2.10 as shown below.

At temperature above T_m, the liquid phase has lower free energy thus the liquid is the stable phase. And at temperature below T_m, the solid state has lower free energy so solid state is the stable phase. The melting temperature T_m is the thermodynamic temperature at which solidification should occur theoretically but this is not the case as nucleation and growth must overcome a kinetic barrier. Thus undercooling of liquids below their equilibrium freezing point is possible.

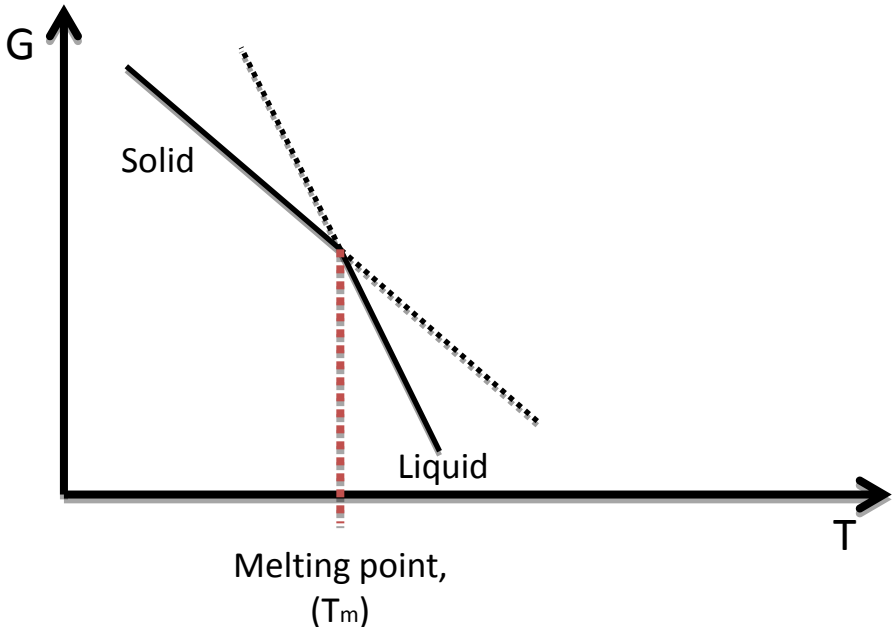

Figure 2.10. Gibbs free energy graph showing stable phase above and below the melting point

2.3.1 Calculating the solid-liquid interfacial energy in homogeneous nucleation

The theories to explain the kinetics of homogeneous nucleation of liquid in supersaturated vapour were developed by Volmer and Weber[76], becker and Doring[77] and Chalmers[78]. These theories have been the basis for most of the theories of nucleation in condensed phases. The difference in free energy ΔG between the solid and the undercooled liquid is called the driving force for the transformation. The total change in free energy is given by two parts which are the increase in surface free energy and the decrease in volume free energy.

$$\Delta G = V\Delta G_V + A_{SL}\sigma_{SL} \qquad 2.8$$

Where V is the volume of solid, ΔG_V is the volume free energy change per unit volume of material, A_{SL} is the solid-liquid interface area

The volume free energy per unit volume of material ΔG_V can be approximated by

$$\Delta G_V = \frac{L\Delta T}{T_m} \quad \textbf{2.9}$$

Where L is the latent heat of fusion, T_m is the melting point and ΔT is undercooling

If a solid of spherical shape with radius r is considered, then the total free energy change is given by

$$\Delta G = -\frac{4}{3}\pi r^3 \Delta G_V + 4\pi r^2 \sigma_{SL} \quad \textbf{2.10}$$

The value of ΔG increases and reaches a maximum value of r called critical radius for nucleation r^* before decreasing. This is where the maximum of ΔG is reached and this is called the activation energy for nucleation ΔG^*. This activation energy barrier must be overcome in order for the newly formed phase to grow with a decrease in ΔG. This is represented in Figure2.11.

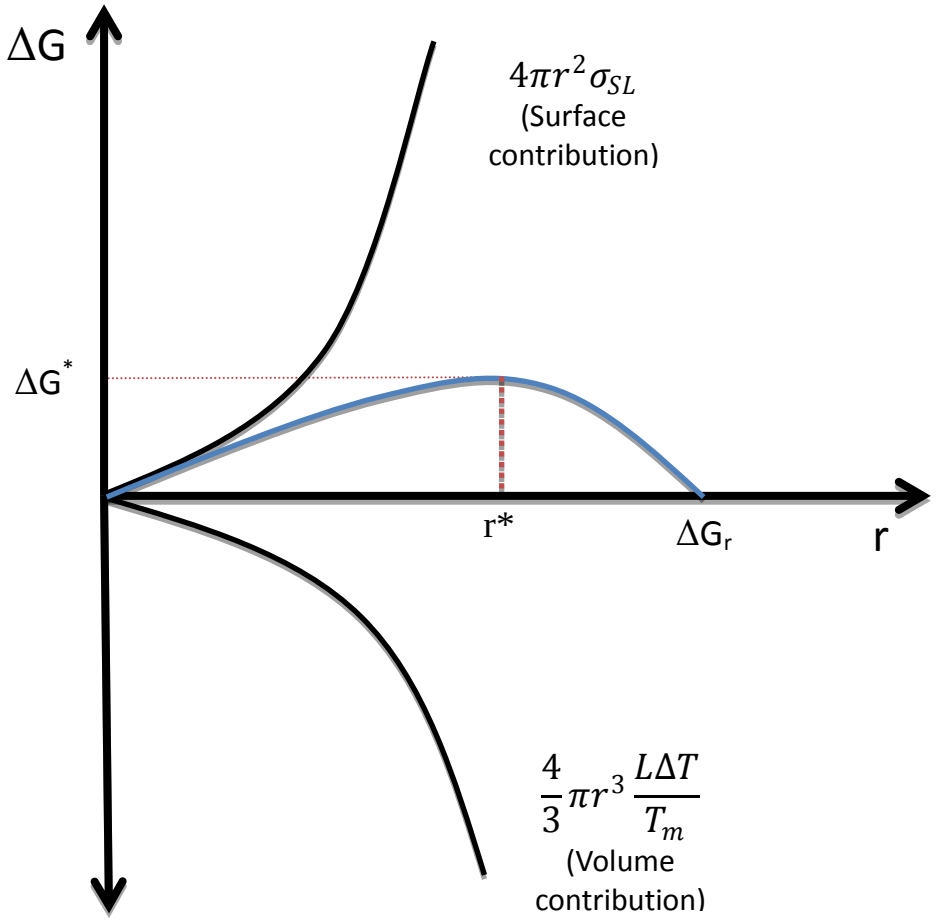

Figure 2.11 Nucleation curve showing the critical radius for nucleus to form and grow

The value of $r^*$is given by maximising ΔG with respect to r, so

$$r^* = \frac{2\sigma_{SL}}{\Delta G_V} \qquad \textbf{2.11a}$$

And by substituting ΔG_Vinto equation 2.9,

$$r^* = \frac{2\sigma_{SL}T_E}{L\Delta T} \qquad \textbf{2.11b}$$

The value of σ_{SL}, can be obtained from critical radiusr^*, nucleation temperature and latent heat required for the nucleation (solidification) using the following equation 2.12,

$$\sigma_{SL} = \frac{(r^* L \Delta T)}{2T_E} \qquad \textbf{2.12}$$

Because the challenges in measuring the small size of critical nucleus, this method has not been used in experiments. However in the last decade, this method has been adopted to calculate the solid-liquid interfacial energy in molecular dynamics simulation, for example, a recent study at the University of Leicester by Liu, Davidchack and Dong [95].

In conclusion, the direct application of Gibbs Thomson equation to the grain boundary groove shape obtained in a temperature gradient was found to be the more powerful method present in experimentally calculating solid liquid interfacial energy. This method is considered a more powerful as groove method can be applied to pure, opaque and transparent materials and also to multi component systems, and to any grain boundary groove shape obtained.

3 Design and Construction of a Radial Heat Flow Apparatus

The Radial heat flow technique has been used in the recent years to experimentally measure the solid liquid interfacial energy for alloys, and it is based on the works by Gündüz and Hunt [7, 45, 46]. The radial heat flow apparatus was developed to observe the grain boundary groove shape in binary eutectic systems. Also Maraşlı and Hunt [80] improved the experimental apparatus to be used for higher temperature applications. In both experimental apparatus, to obtain a high temperature gradient, the cooling jacket was close to the outside of the specimen to get effective radial cooling. The high temperature gradient is useful in obtaining equilibrated grain boundary groove shapes in a shorter annealing time.

The practical difficulties in applying the Gibbs Thomson equationon grain boundary groove shape was to obtaining the equilibrated groove shape. The equilibrium condition is very unstable as small fluctuations in temperature can cause either complete melting or solidification. Thus the temperature control of the apparatus needed to improve on temperature control. The existing design implemented single wire heating element with mains power source needed to supply power to the element. This design has limitations in the longevity of the element and the temperature capabilities as well as safety concerns regarding using mains power. These were major limitations concerning the control of the temperature, which is the most important part. The new modification was done to the existing design to improveon these limitations by applying coiled central heating wire to improve the temperature control by 50% from the previous work by Maraşlı and Hunt, and also power system was set up to accommodate the use DC power supply rather than mains AC to vastly improve safety aspect of the apparatus.

The main aim of this study is to design and construct a Radial heat flow apparatus and then to commission and test using a commercial Al alloy. In this chapter, the design and construction process will be described in following sections.

A CAD drawing of the apparatus is shown in Fig 3.1.

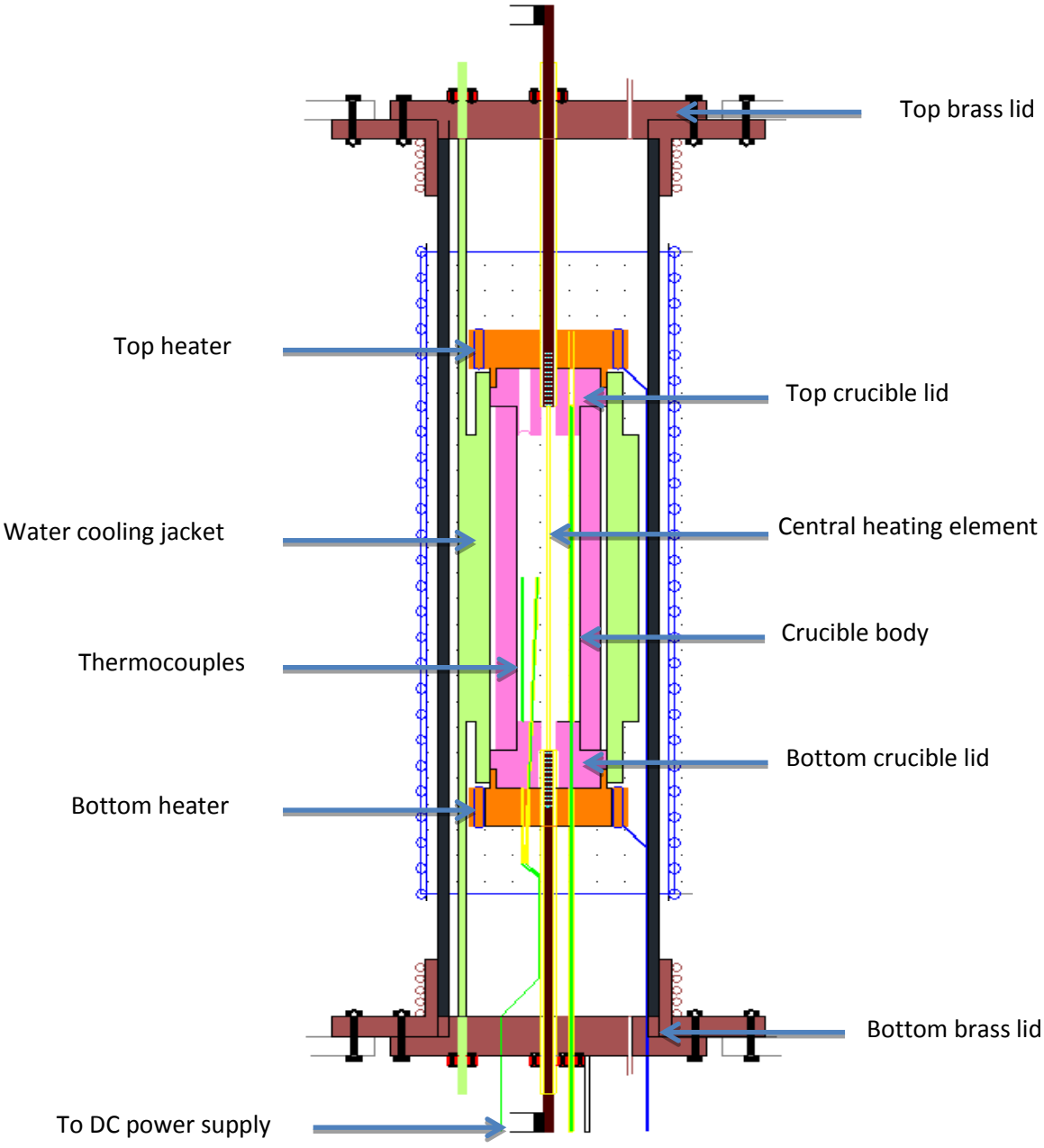

Figure 3.1. AutoCAD drawing of the schematic of the radial heat flow apparatus

3.1 Main crucible

The main crucible of the apparatus was originally designed with graphite, however, a machinable alumina was considered a better option to replace the graphite as the graphite burns at high temperature and lose weight and also to prevent alloy reacting with the container. The machinable alumina was supplied by Aremco and the product was bisque-fired alumina with maximum working temperature of 1400℃. The crucible was made of three parts; crucible body, top and bottom lids. The main crucible body was made from machinable alumina of cylindrical tube of OD 46mm and ID 30mm, with the length 100mm. The crucible lids were also made from machinable alumina.

3.1.1 The bottom crucible lid

The bottom crucible lid was made to fit into the crucible body. The top of the bottom lid was machined to be inserted into the crucible body, which was of diameter 30mm and height of 15mm. The middle part was where the crucible body would sit, which was of diameter 48mm and height 10mm. The bottom part of the lid was machined so that the lid would be fitted to the bottom heater holder, and was of diameter 46mm and height 10mm and further cut to diameter 41mm and height 2.5mm. From figure 3.2, it can be seen that there are 5 holes to be machined into the bottom lid.

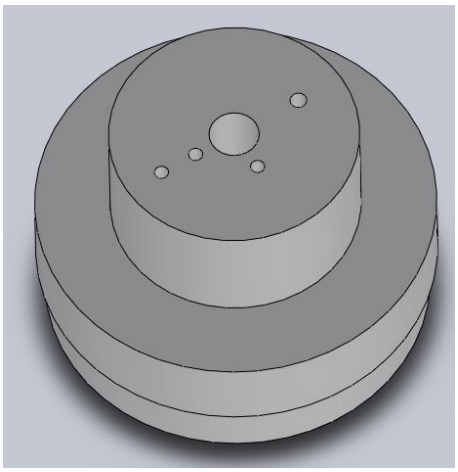

Figure 3.2. Isometric view of the bottom crucible lid

The central hole of diameter 6mm was cut through to fit alumina tube for the central heating element. The schematic of the top view of the bottom lid is shown in figure 3.3 and this shows the four holes for the thermocouples.

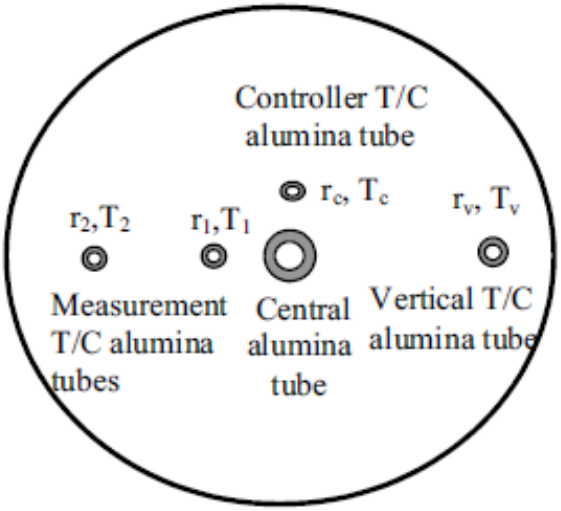

Figure 3.3 Schematic of the bottom lid and the holes for the thermocouples

The two holes to the left of the central bore were to fit the alumina tubes for the measurement thermocouples at two different distances from the centre, in order to measure temperatures for thermal conductivity calculation. The r_2 hole was 12mm away from the centre of the lid with diameter 1.7mm. The r_1 hole was drilled at an angle of 87 degrees from the central axis, drilling was initiated from the bottom of the lid, 9mm away from the centre bore.

The hole to the right of the central bore was to fit the alumina tube for the vertical thermocouple. The hole of diameter 2mm was drilled at 11mm away from the centre.

The hole above the centre bore was to fit alumina tube for the control thermocouple. At r_C, the hole of diameter 1.7mm was drilled at an angle of 87 degrees from the centre axis, initiated from the bottom of the lid, 9mm away from the centre. The control thermocouple hole was drilled at an angle to allow the thermocouple to be as close to the central alumina tube to control the temperature as accurately by having faster response.

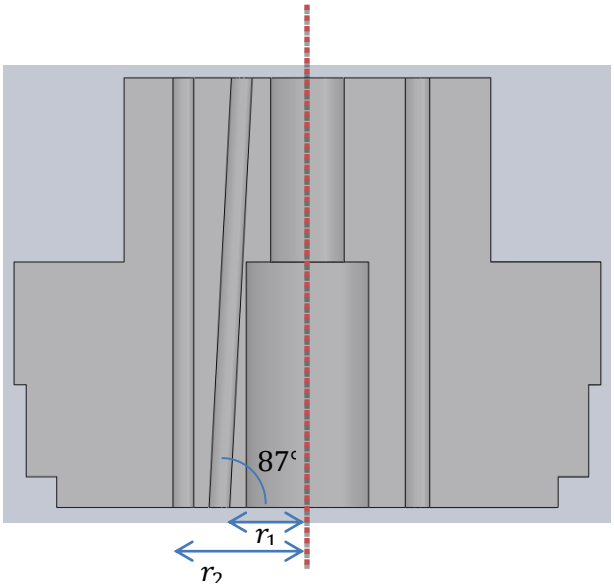

Figure 3.4 Cross section view of the bottom crucible lid showing holes for the thermocouples

From the front section view shown in figure 3.4, it can be seen that the central hole of diameter 6mm where the alumina tube for the central heating element would fit. The larger bore of diameter 10mm with depth 20mm is machined to the centre bore to allow room for the connections from the central heating element to the copper wire. The section view clarifies how the holes are machined, showing two holes to the left of the central hole with the hole at r_1 machined at 87degrees. Apart from the central bore where the heating element will be placed, the four holes are for the thermocouples, three for measuring and one for control.

3.1.2 The top crucible lid

The top crucible lid was also made into three sections, where the top section would be inserted into the crucible body, has a diameter 30mm and height 15mm. The middle part has diameter 48mm and height 10mm where the crucible body will seal. The bottom part where the top heater holder would sit has diameter 46mm and height 10mm which is further cut in to diameter 41mm and height 2.5mm. The isometric view of the top crucible lid is shown in figure 3.5.

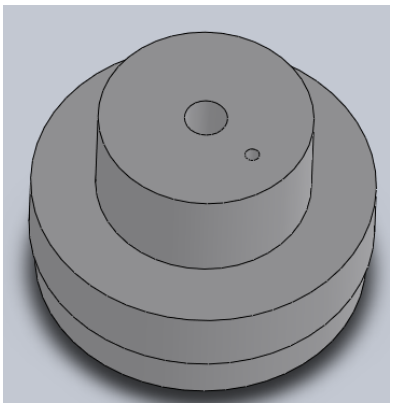

Figure 3.5 Isometric view of the top crucible lid

The top crucible lid has central bore of diameter of 6mm and has larger bore of diameter 10mm and depth 20mm machined from the bottom of the lid, which is the same as the bottom crucible lid to allow room for the connection between the heating element and copper wire to the power supply. The hole to the right of the center hole is for the vertical thermocouple and is machined 11mm away from the centre bore with diameter is 2mm.

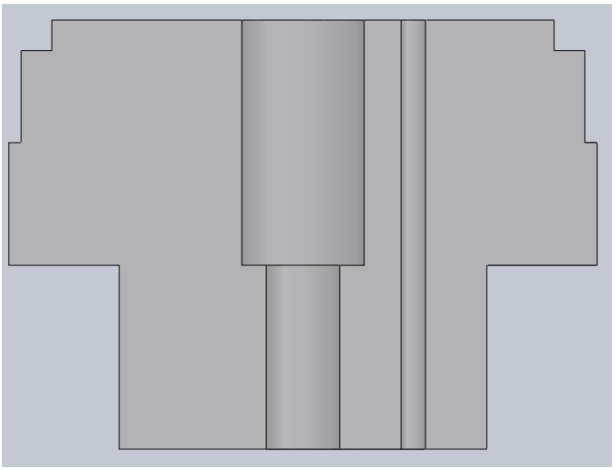

Figure 3.6 Section view of the top crucible lid

3.1.3 Crucible container assembly

Before the crucible body is placed, first the alumina tubes are fitted onto the bottom crucible lid. The alumina tubes are used to shield both the central heating element and the thermocouples. The alumina tubes were supplied by Umicore. The total length of the crucible container with the body and both lids were 140mm. The central alumina tube for the central heating element had outer diameter 6mm and inner diameter 5mm and was cut to length of around 130mm. The alumina tubes for the measurement and control thermocouples had outer diameter 1.7mm and inner diameter 1.1mm and was cut to length of around 70mm. The alumina tube for the vertical thermocouple had outer diameter 2mm and inner diameter 1.2mm and was cut to the length of around 130mm. All of the alumina tubes were cut using a cutter with a diamond tip blade. All of the alumina tubes were secured in place and sealed using ceramic adhesive supplied by Aremco. The schematic of the completed assembly of the crucible container is shown in figure 3.7.

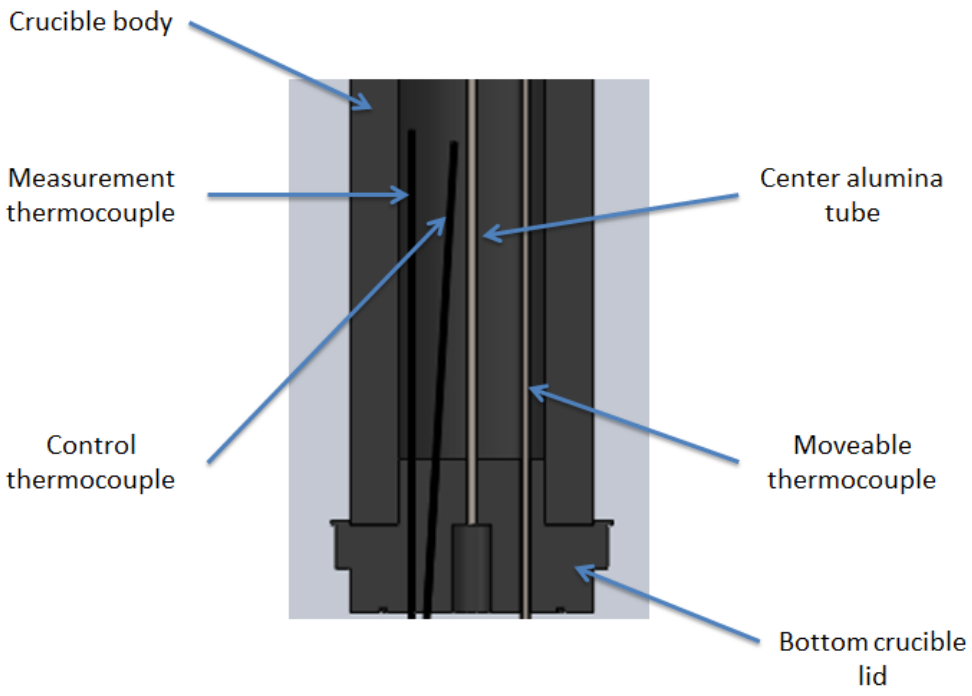

Figure 3.7. Schematic of the fitted alumina tubes for the heating element and the thermocouples

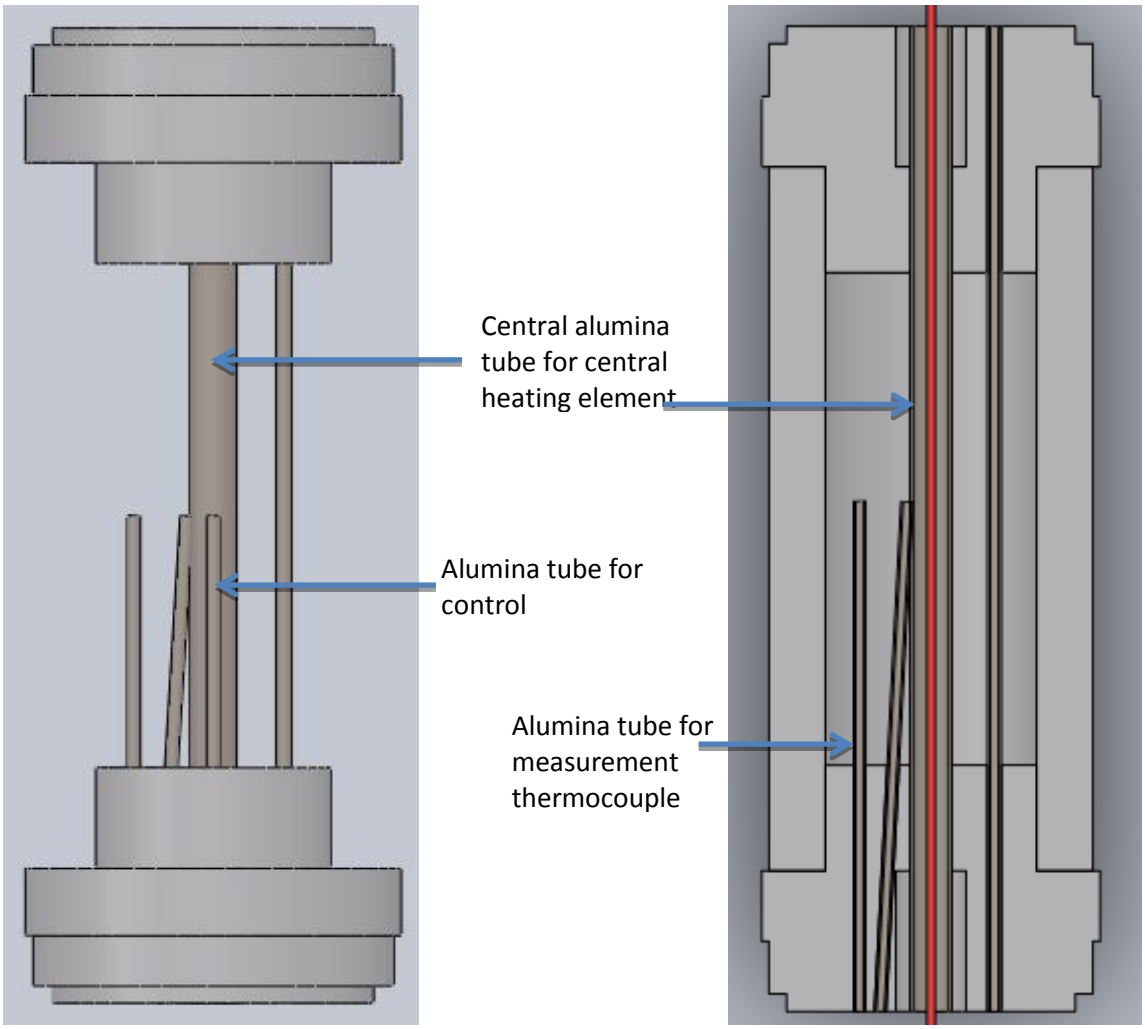

Figure 3.8 a) A section view of the complete assembly of crucible container with central heating element (red)

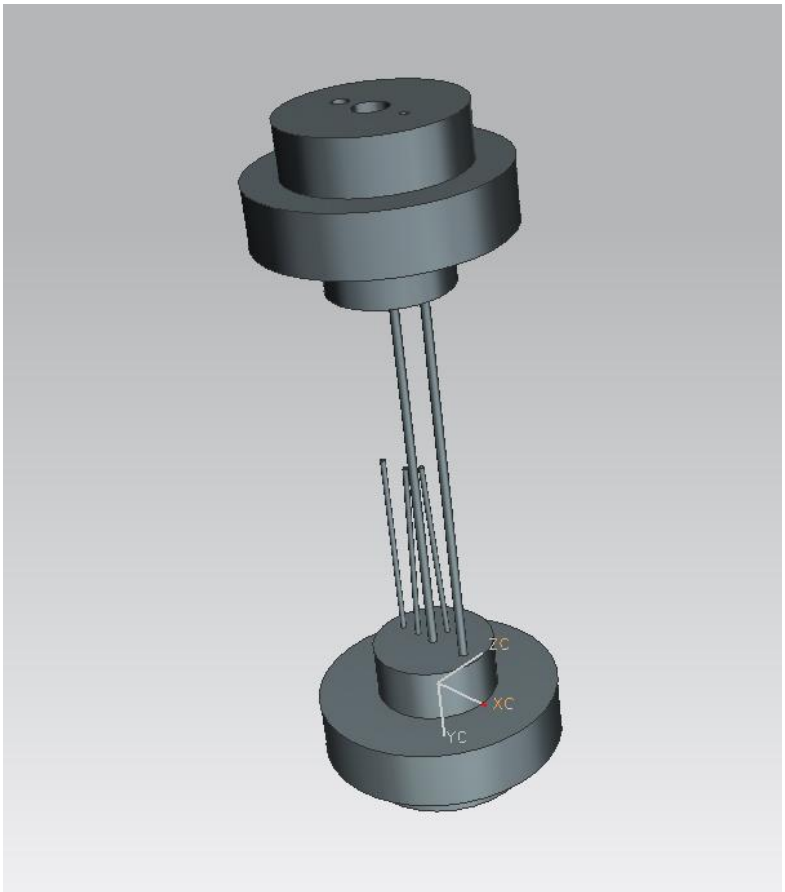

Figure 3.8 b) Isometric view of the assembly of crucible container with alumina tubes for the thermocouples

3.2 Radial heat flow apparatus assembly

3.2.1 Top and bottom heater holder

During the experiment, it is crucial that the temperature gradient is only occurring in the radial direction and not in the y-axis direction. To be able to achieve this, top and bottom heaters were used.

The top and bottom heater holder were also made of machinable alumina. The holder was machined from a cylinder of outer diameter 50mm and inner diameter 34mm. The top of the holder was machined to depth of 2.5mm and diameter 41mm so the top and bottom lids fit securely. The slot where the resistance heating elements are going to be placed was cut into the cylinder 10mm down from the top of the holder and it was machine cut into the cylinder at depth and height of 5mm. The bottom of the holder was machined down to diameter 45mm and depth 2.5mm so it fitted to the stainless steel stand.

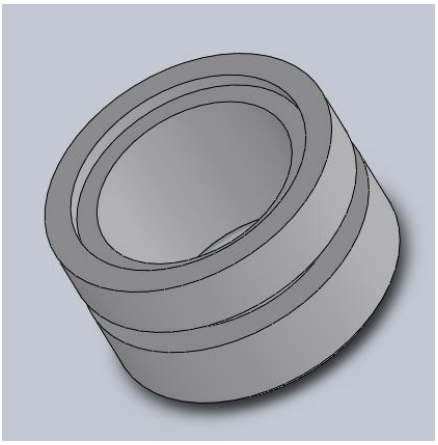

Figure 3.9 Isometric view of the top and bottom heater holder

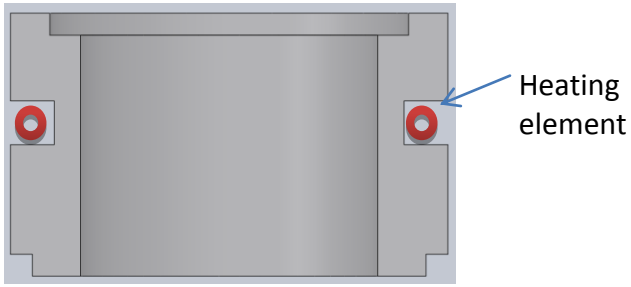

Figure 3.10 Section view of the top and bottom heater holder

3.2.2 Water cooling jacket

When the experiment is run, it is important to have the radial temperature gradient in x-axis, and the water cooling jacket is placed around the crucible container to achieve this. The water cooling jacket was made of stainless steel sheets. A stainless steel sheet was rolled to give inner diameter 50mm by welding with length of 140mm. A second stainless steel sheet was rolled to give outer diameter of 90mm with the same length. The two rolled stainless steel were connected together by welding the both ends of two rolls with a stainless steel disc. This produced a hollow cylinder tank.

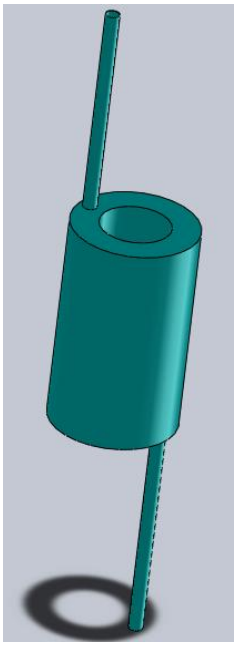

Figure 3.11 Isometric view of the water cooling jacket

The inlet and outlet were drilled into the tank, with inlet drilled with centre at 37mm from the centre of the tank with diameter 10mm, and the outlet were also drilled on the opposite face with the same size hole. The inlet and outlet pipes were also stainless steel tubes of outer diameter 10mm and inner diameter 8mm and were welded to the inlet and outlet holes drilled earlier.

3.2.3 An assembly with crucible container and water cooling jacket

The assembly is done in a step and the apparatus was built from inside out, starting from the crucible container and then the top and bottom heater holder and the stainless steel water cooling jacket were assembled. This is represented in figure 3.12.

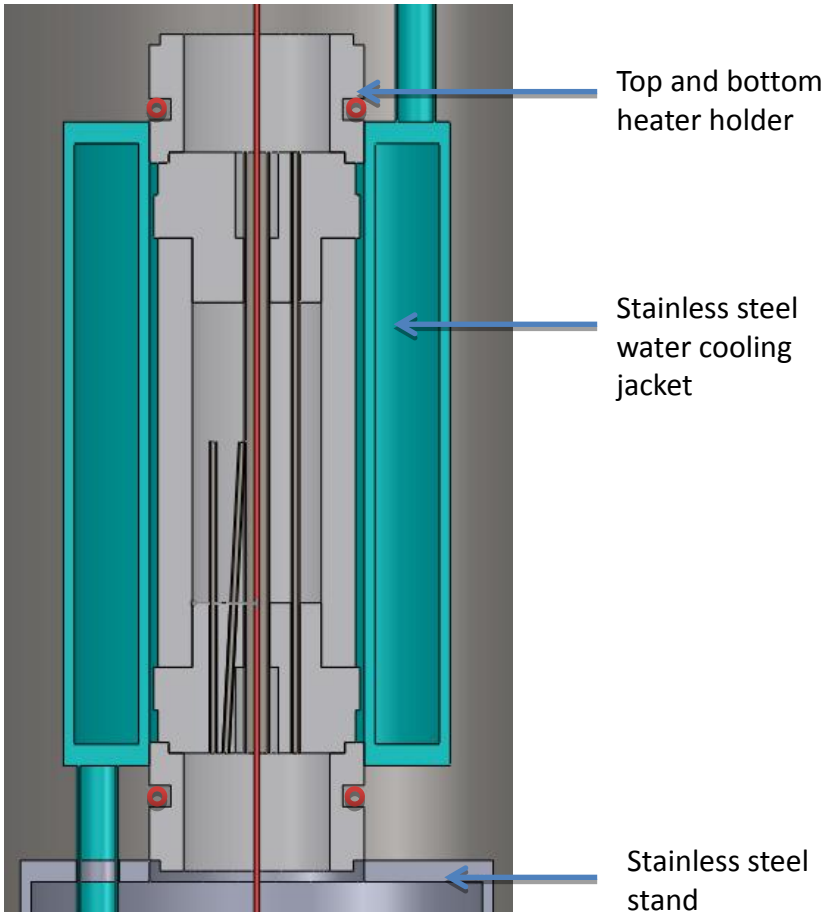

Figure 3.12 Cross section of assembly of crucible container and water cooling jacket

3.2.4 The apparatus casing with brass lids

The final part of the apparatus is the outer casing for the radial heat apparatus. The outer casing was made of aluminium tube of length 400mm with inner diameter 130mm and outer diameter of 140mm. This outer aluminium casing was coated with copper sheet to provide electromagnetic shielding from noise. The top and bottom of the casing was fitted with brass plates which fit onto the aluminium casing to seal the apparatus making it air tight.

The bottom brass lid was made from a brass disc of diameter 150mm and height 22.5mm. The top part of the lid was machined down to diameter 105 and height 2.5mm, which was to secure the steel stand that holds the crucible container and water cooling jacket. Then it was machined down to diameter 130mm and height 10mm to fit in to the aluminium casing. A groove was machined into the side of this part of the lid to hold a rubber O ring to give air seal. The centrebore was machined at diameter 10mm through all. This hole was to house a spark plug, which was used to supply power to the central heating element.

To the left, a hole of diameter 10mm was also machined 37mm away from the centre. This was for the water cooling jacket inlet. To the right another hole was drilled with diameter 10mm, 30mm away from the centre. This was for the thermocouple wires to feed through.

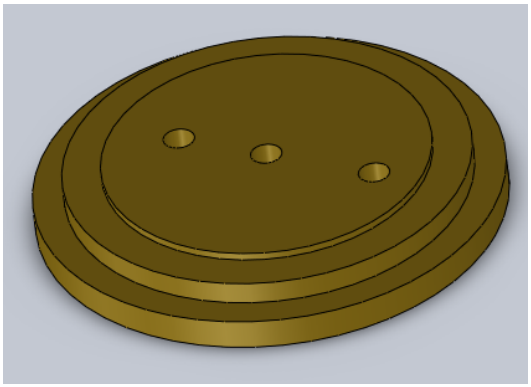

Figure 3.13 Isometric view of the bottom brass lid

The top brass lid was also made from a brass disc of diameter150mm and height 20mm. The top part of the lid was machined down to diameter 130mm and height 10mm to fit into the aluminium casing. A groove was also machined to this part of the ring to hold a rubber O ring. The centre hole was drilled at diameter 10mm through all for the heating element outlet. The hole to the right, was drilled 37mm away from the centre at diameter 10mm which was for the outlet pipe of the water cooling jacket. The two holes were machined for the argon inlet and outlet, an inlet to the left of the centre bore at 30mm away from the centre at diameter 10mm and an outlet to the top of the centre bore at 30mm away from the centre at diameter 10mm.

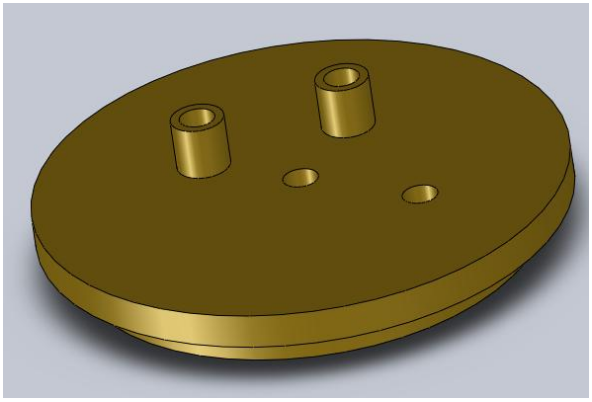

Figure 3.14. Isometric view of the top brass lid with argon inlet and outlet

3.3 The complete assembly of the radial heat flow apparatus

The schematic of the completed assembly of the radial heat flow apparatus is shown in figure 3.15.

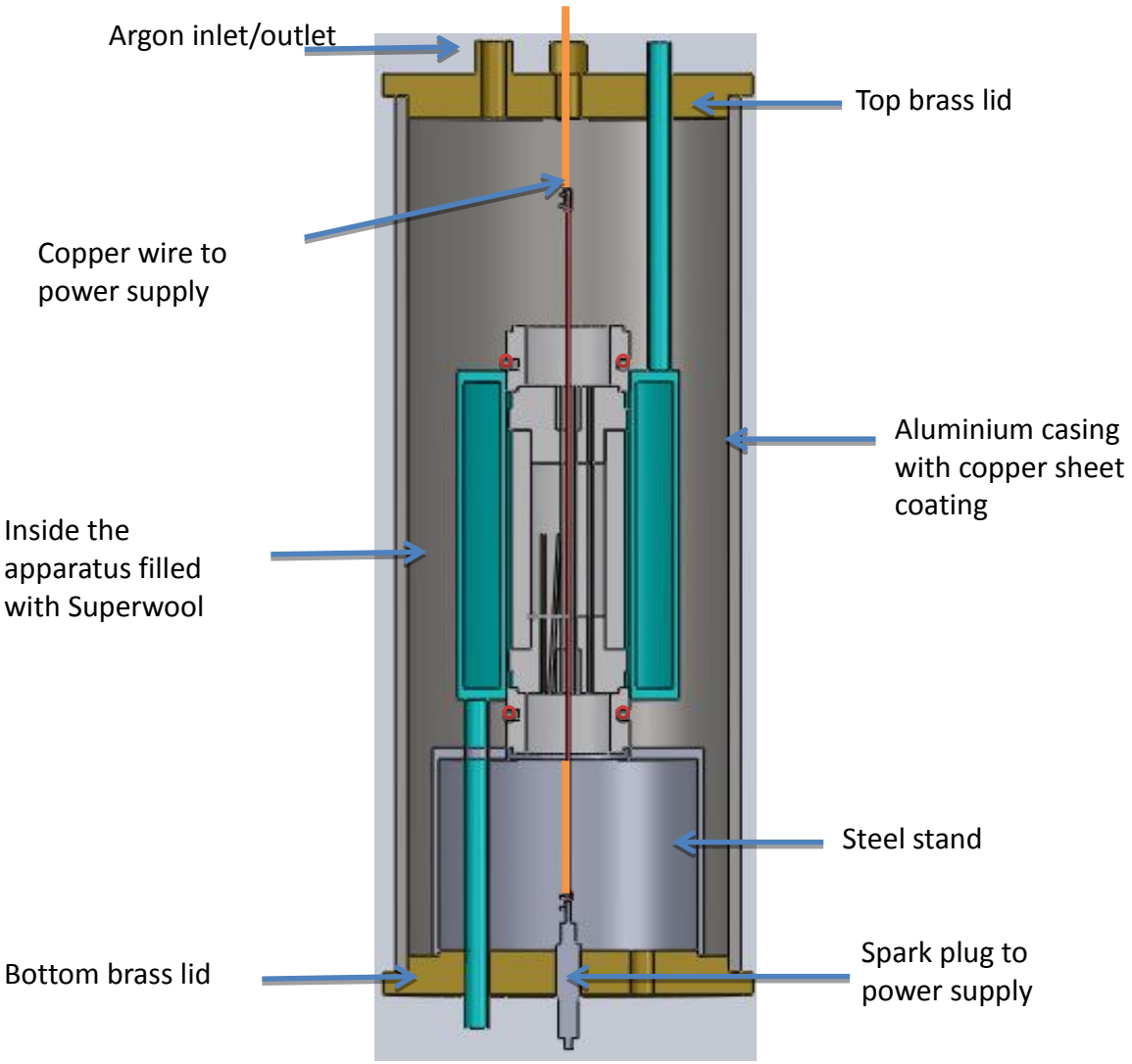

Figure 3.15 CAD drawing of the completed assembly of the radial heat flow apparatus

3.4 Thermal analysis on the radial heat flow apparatus

Thermal analysis was carried out on whole of the apparatus system to visualise the heat distribution within the apparatus. The software package NX8.0 from Siemens was used to represent the apparatus in 3D and to also carry out the simulation.

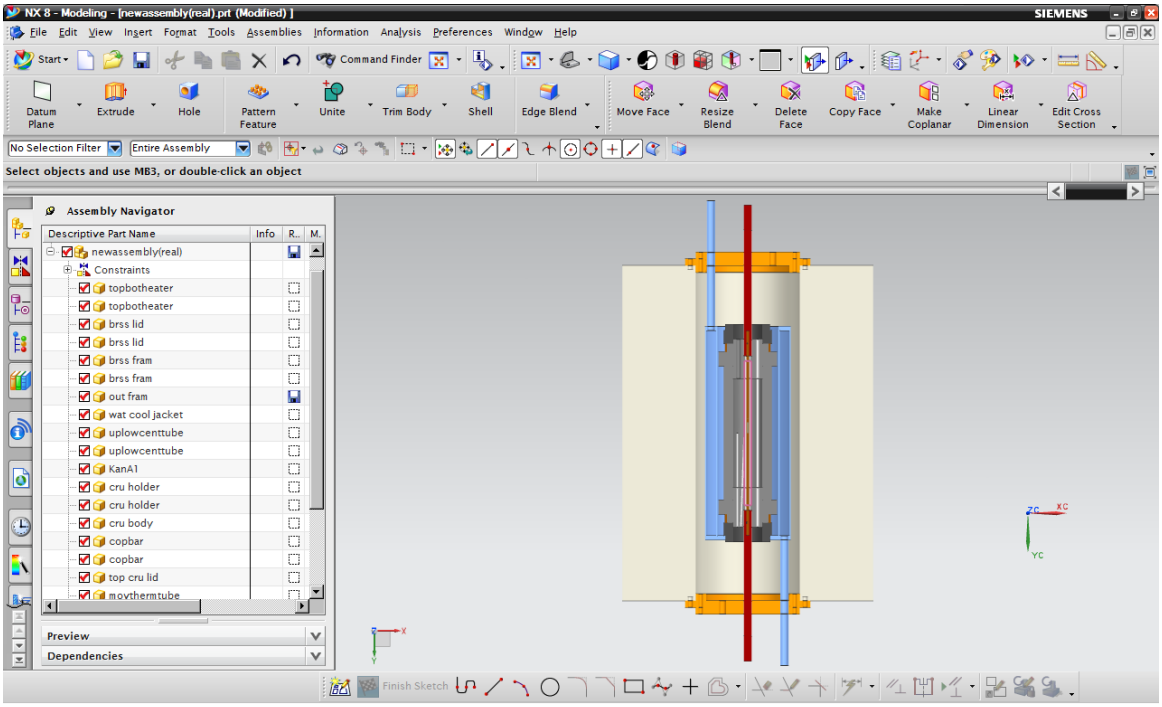

Figure 3.16 NX 8.0 drawing and assembly is used to model thermal distribution

The 'model' parts are drawn separately and the 'model' parts are then assembled together to give the final assembly 'model' apparatus. To carry out the thermal analysis, each part needs to be created into a 'FEM' parts. Each 'model' parts are assigned with their material properties, according to the material that was used to build that part,i.e. densities, melting point and etc. For example the material for the crucible body was machinable alumina, so the material properties for the machinable alumina from the product data sheet were inputted to the program. The next step is to apply 3D tetrahedral mesh to the part. Once this is done, the 'model' part becomes a 'FEM' parts. If this has been done for all of the 'model' parts that is in the apparatus, then the new 'FEM' parts that are created can be assembled together to

produce a final assembled ‘FEM’ model. This final assembled ‘FEM’ part is then ready to be used for the thermal analysis. The steps are shown in Figure 3.17 and 3.18 below.

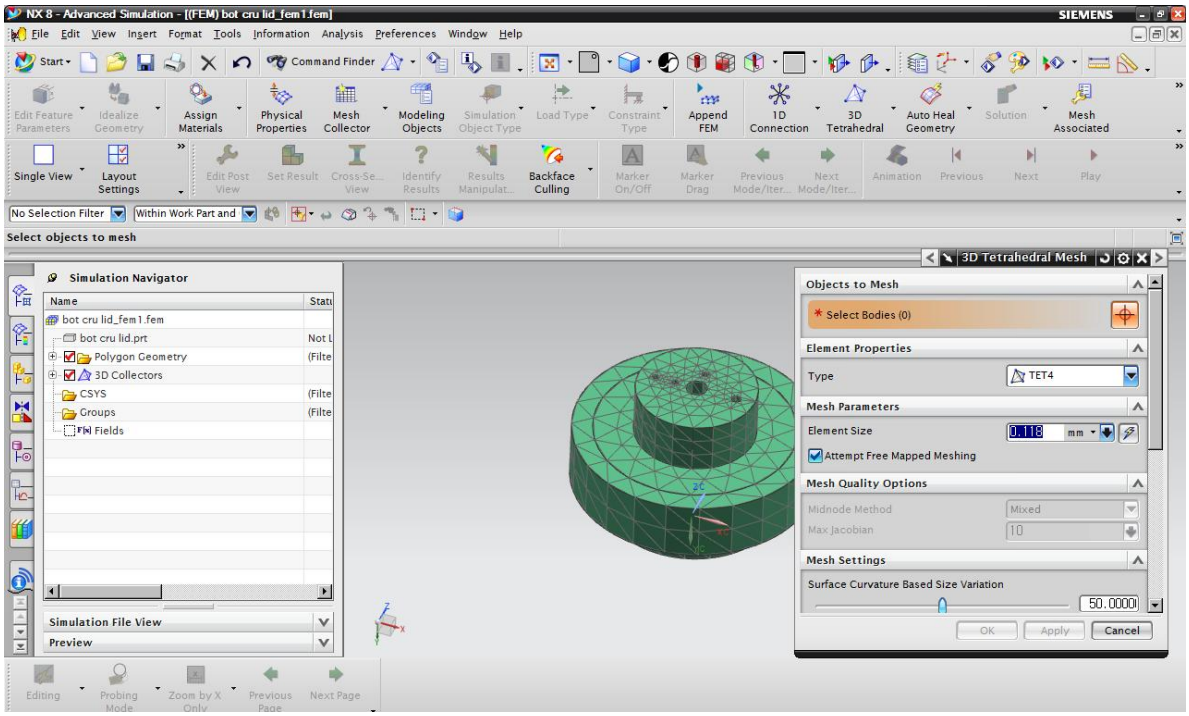

Figure 3.17 Creating FEM part for each component used in the full assembly, in this case bottom crucible lid.

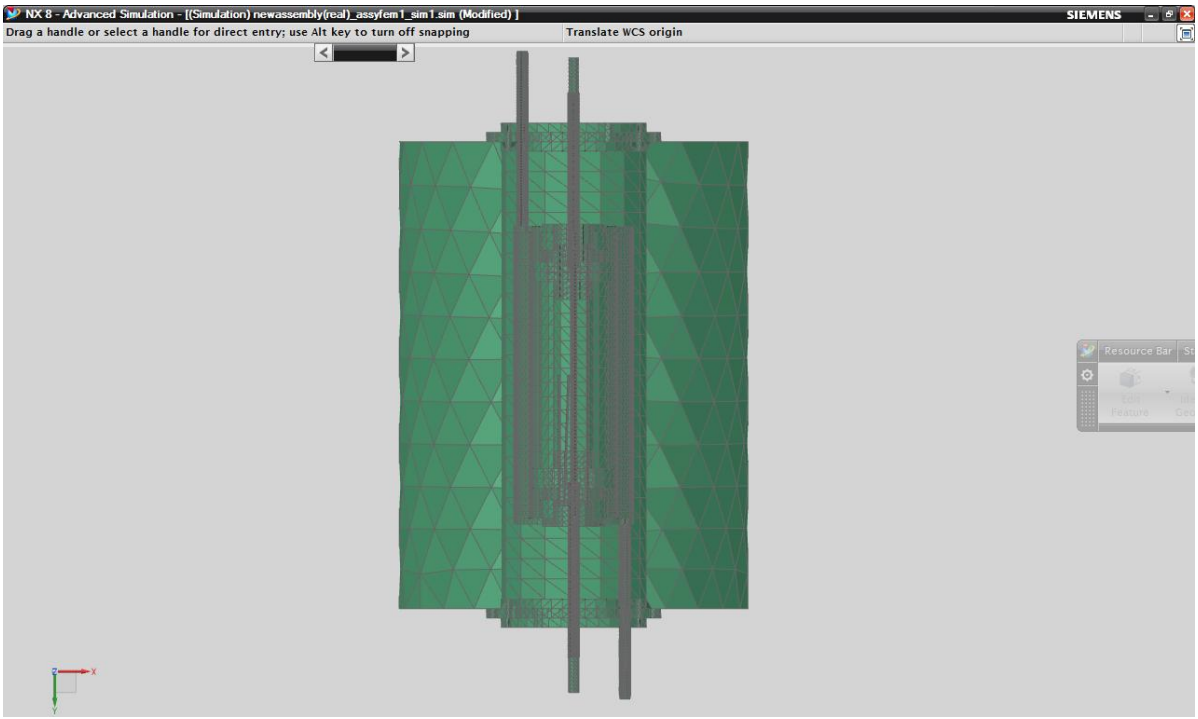

Figure 3.18 Creating FEM assembly of the whole system by putting together each FEM part of the apparatus

The thermal analysis is done so that it starts from the heat source and then outwards. In the 'FEM' assembly, thermal load can be applied to the central heating element, and the heat load value is inputed as 2000W as tested in the testing rig. Then the 'thermal coupling' is applied to represent the conduction of heat between each touching parts, this is essential as the heat dissipates through each touching part. In this case the conductance value was set to 100W/C. After this the temperature was set using 'constraint', and on the water cooling jacket, the temperature was set at 25^{o}C, and to speed up the process, the environment was assumed to be at 30^{o}C rather than using radiation to environment. The final step was to set up 'radiation thermal coupling' between the parts that were not touching, but still worked as a heat sink.

Once all the parameters are set as above, the thermal analysis can be left to run. The following figures show the results from the analysis.

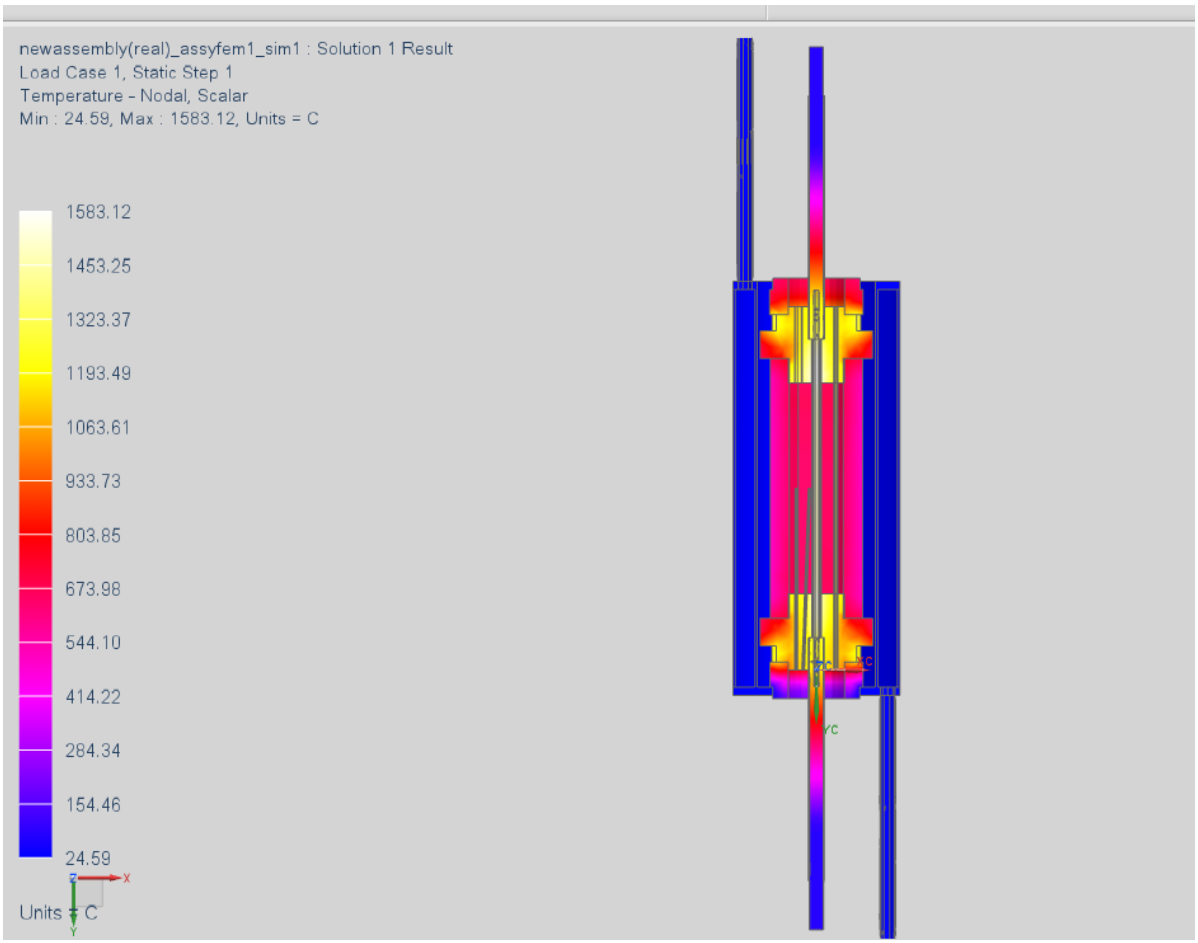

Figure 3.19 Thermal analysis of crucible container with water cooling jacket

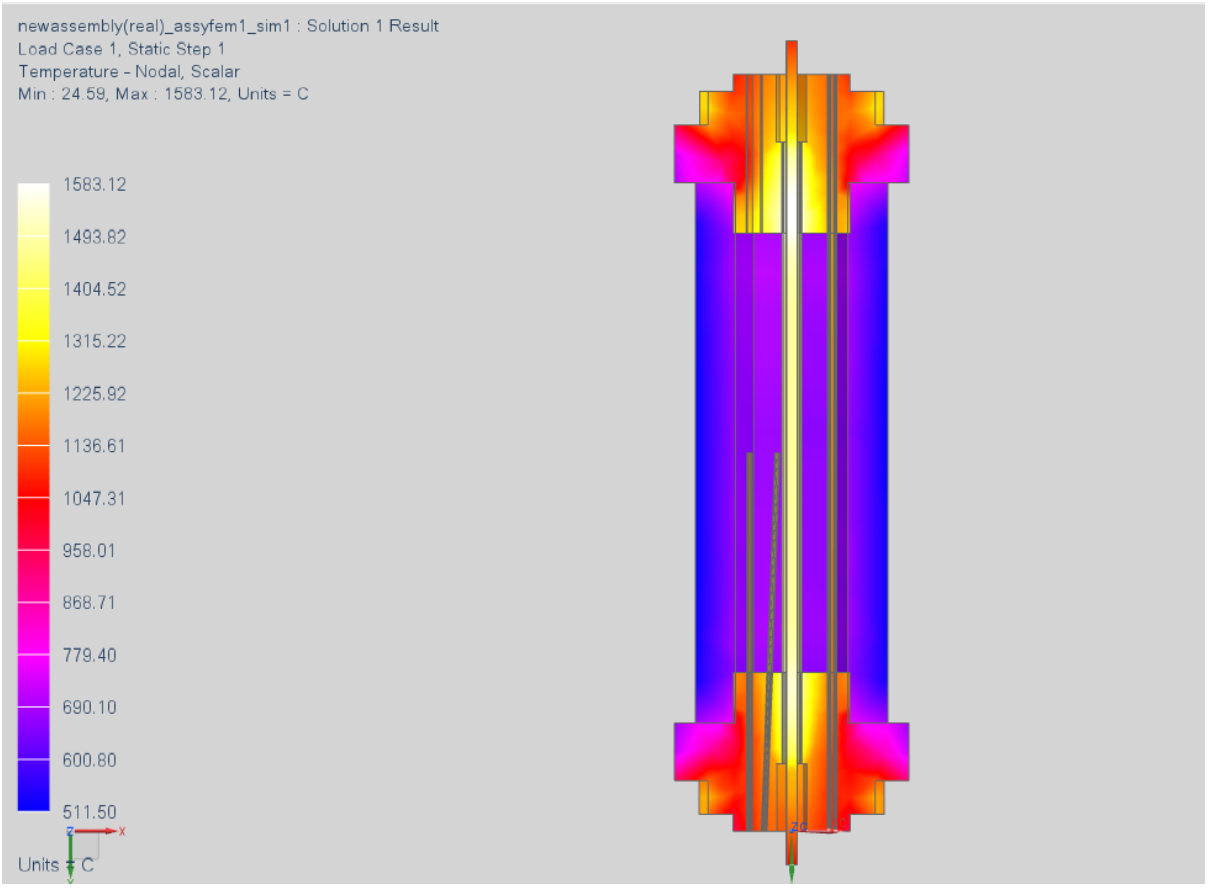

Figure 3.20 Thermal analysis showing temperature gradient in radial direction

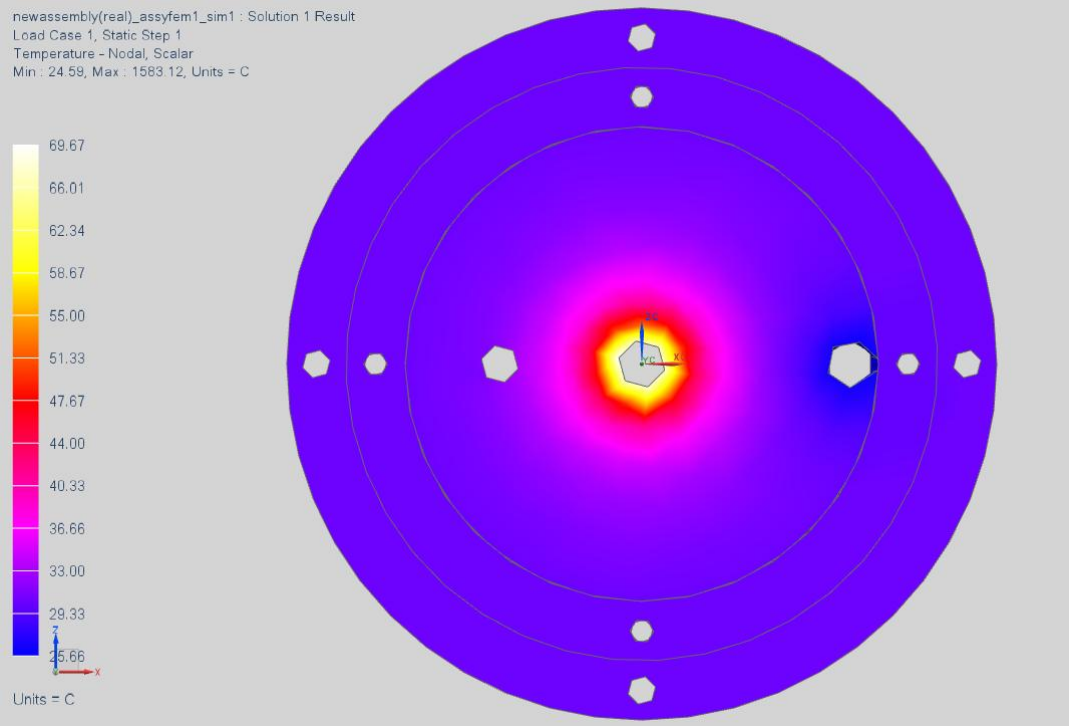

Figure 3.21 Thermal analysis on the brass lid on the outside of the apparatus

The thermal analyses indicate that the design is sufficient in order to achieve the purpose of the experiment, which is to have thermal gradient in horizontal direction and avoid temperature gradient being applied vertically. As can be observed in figure 3.20, the stainless cooling jacket works well to take the heat away from the crucible container in order to obtain high temperature gradient which is desirable.

3.5 Testing of the heating element

The testing rig was set up in the Chemistry Department at the University of Leicester, with a very simple quatz glass tubing. The heating element in a alumina tube was placed in the glass tube with the heating wire connected at either end by copper rods. A copper connector was designed so that the heating element could be fixed to the copper rod by the use of grub screws. The copper rod also had a plate connector which were connected to the power supply. The plate design prevented the copper rod from melting due to the build up of heat at the connection, by dissipating heat over a surface. The glass tube was flushed with nitrogen gas from one inlet and also had another inlet for the thermocouple.

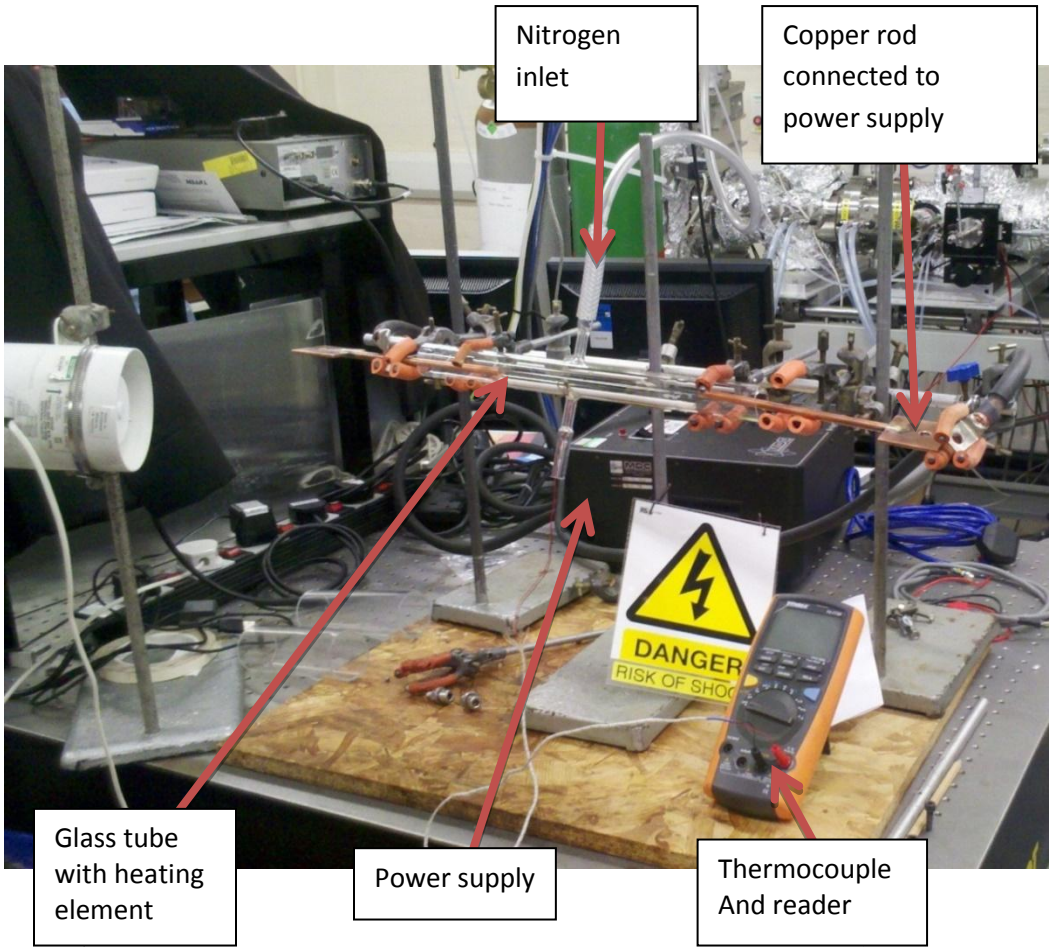

Figure 3.22 Experiment set up to test heating element

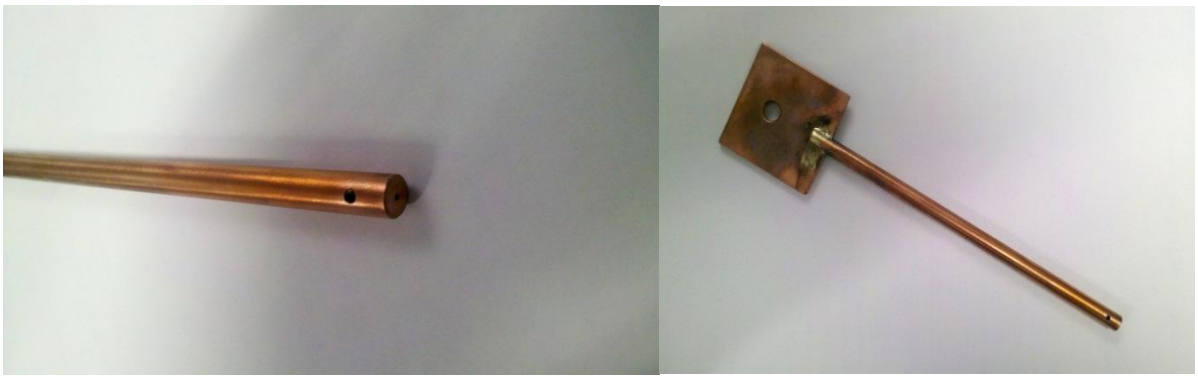

Figure 3.23 A design of copper connector; Left is a hole to place heating element wire and fix with grub screw, Right is the connecting plate which will hold connector of a high current power supply.

The first test started with the testing of Kanthal A1 wires of length 200mm. The first test was using the wire of diameter 2.65mm and the second was using the wire of diameter 3.5mm as shown in figure 3.24. It was logically assumed that as the length of wire is so short for the required power generation (i.e around 2-4KW), the power supply would need to supply a very large amount of current.

The power supply used was 12V/200A with a varying amount of voltage supplied. As the heating element needed to be heated up to the temperatures of above 1000^{o}C, the voltage and current was noted from the 500^{o}C onwards. For the wire of diameter 3.5mm,

-At 65% of 12V, the current supplying meter showed 100A and the temperature was 500^{o}C.

-At 75% of 12V, the current supplying meter showed 125A and the temperature was 700^{o}C.

The power supply was nearing the end of its maximum power and the heating element was struggling to reach near 1000^{o}C, and,

-At maximum 12V, the current supplying meter showed 180A to 190A and the temperature was 890^{o}C.

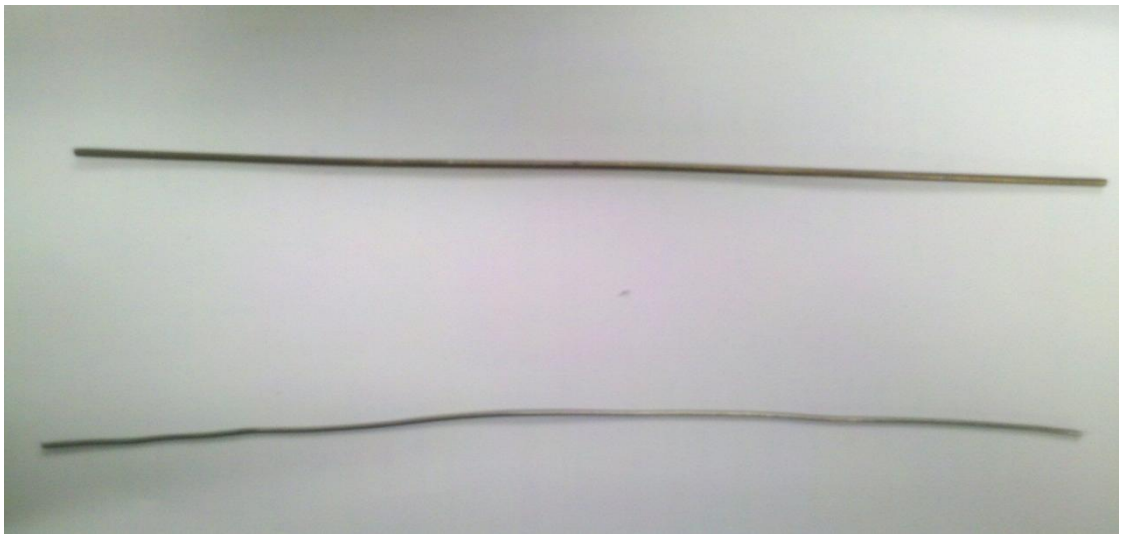

Figure 3.24 A single wire of Kanthal A1 was tested with wire diameter; Top, 3.25mm and Bottom 2.65mm

As this was the maximum power that could be supplied, the test was ended by turning off the power supply. The test for wire of diameter 2.65mm was done but the test was abandoned as the heating element struggled to produce any significant amount of heat to reach temperature above 600^{o}C.

The post-test pieces of the Kanthal A1 wires are shown in figure 3.25, and these provide clear evidence that the use of a single straight wire heating element is unsuitable. Although the testing was run only a short duration, the heating wire showed signs of elongation upon reaching high temperature, and in one case, broke the alumina tube that it was housing.

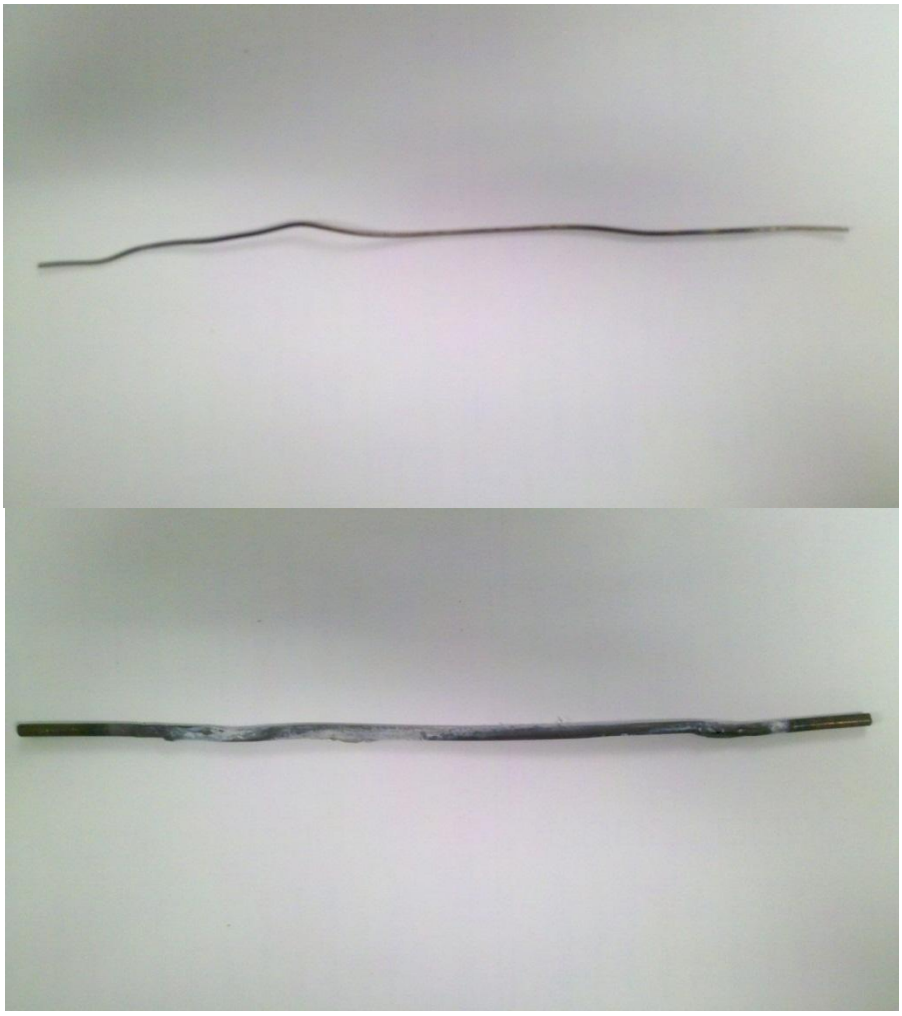

Figure 3.25 Post-test pieces of single heating element wire Kanthal A1 with diameter; Top 2.65mm and Bottom 3.25mm

Also Figure 3.26 shows oxidation around the heating element and in some areas of the wire, there was evidence of blow out due to the air trapped in the wire caused by a defect blowing out in high temperature causing the heating element to split.

Figure 3.26 Kanthal A1 wire showing oxidation and split of the wire due to ‘blow out’

This result has clearly shown that a new heating element design is needed to be implemented, and by consulting technicians and fellow students, it was thought that a coiled heating element would be the best approach.

A tantalum wire of diameter 0.5mm was tested as it could provide a very high temperature and is also very flexible and soft so it can easily be coiled. The below in figure 3.27 show the coiled tantalum wire in an alumina tube.

Figure 3.27 Showing a coiled tantalum heating element wire

The tantalum wire had a resistance of 3ohms, and the power supply used was 120V/40A power supply with variable amperage.

Amperage (A)	Voltage (V)	Temperature (^{o}C)
1	2.73	31.5
2	7.3	74
3	16.4	178
4	30	373
5	47	580
6	72.6	720
7	104.3	860
7.2	120	890

Table 3.1 A test result for the coiled tantalum heating element wire

The result shows that the wire requires much lower amperage compared to the single wire heating element as it is longer in length, thus it was much safer than using high current power supply. However, the challenge this time was that the voltage required would need to be very high in order to drive the current through the thin wire. The next test was to use 240V transformer and rheostat to connect directly to the mains to control the voltage. This set up gave the following results in table 3.2.

Amperage (A)	Voltage (V)	Temperature (^{o}C)
5.83	102.9	800
7	133.7	900
7.5	150	1000
7.7	170	1060
8	183	1100

Table 3.2 A test result for the tantalum wire with higher voltage

The temperature it reached was promising however due to the safety of the test set up and the continuous blowing of fuse, the test was ended. The post-test tantalum wire was observed and

it was not very promising as the heating element was too malleable causing it to lose shape and the element was prone to oxidation and often broke after few hours of run. This was especially not suitable as the heating element set up in the radial heat flow apparatus needed to be vertical. However it was still a productive testing to show that the use of single wire heating element design used in the previous literature was not the best. The single wire set up had very nominal resistance and to heat up the element required a very powerful high ampage power supply. This set up of supplying high current was considered too dangerous and an alternative set up was needed.

The use of heating element that was too thin was also ruled out as it required a very high voltage set up and would need to be run with a mains power supply. This too was considered very dangerous set up.

Thus it was decided that the suitable heating element would use this set up similar to coiled tantalum heating wire, but with thicker wire and with better oxidation resistance.

The Kanthal A1 wire was chosen to replace the previous design of single wire set up. The wire was also thicker at around 1.2mm and coiled to give more resistance to the heating element. This allowed the power supply to be replaced from mains AC power to a more safe 30Volt/30Amp DC power supply.

3.6 Parts list to build radial heat flow apparatus

The apparatus was built from inside out, building from centre to outside. Firstly, central heating element wire was chosen to be Kanthal A1 (FeCrAl alloy) supplied by Kanthal, as it had high working temperature and was also able to continue working at high temperature without oxidation in air. The alumina tubes were supplied by Umicore and the machinable alumina for

the crucible container was supplied by Aremco. The thermocouples were chosen to be type K thermocouples with nickel sheath around it that could withstand high temperature furnace application.

Description	**Material**	**Supplier**
Central heating element	Kanthal A1 (FeCrAl alloy)	Kanthal
Alumina tubes for the central heating wire and thermocouples	Alumina	Umicore
Thermocouples (nickel sheathed, outer diameter 1mm, length 300mm)	Type K (Chromel/Alumel)	TC direct
Machineable alumina for crucible container	Bisque-fired alumina	Aremco
Ceramic adhesive	Alumina	Aremco
Water cooling jacket	Stainless steel	University store
Aluminium casing	Aluminium	University store
Brass lids	Brass	University store
Superwool to use as insulation in the apparatus	Ca-Mg-Silicate	Morgan advanced materials
Rubber bungs to seal inlets	Rubber	Rapids
High temperature connector to connect copper wire to power supply	Ceramic/ nickel coated	RS components
High temperature crimps to connect heating element to copper wire	Nickel	RS components

Table 3.3 A Parts list to build radial heat flow apparatus

3.7 Temperature Control

The simplest type of temperature control is on/off control, where the heating power is fully on when the temperature is below the set point and when the temperature is above the set point, the power is fully off. This means that the temperature oscillates about the set point and as a result the average temperature may be offset from the set point. The time period and the amplitude of the oscillation is a function of the thermal lag between the temperature sensor and the heating element[81].

For applications which do not require critical temperature control, the on/off control is satisfactory as some oscillation from the set point is permissible. However for applications where a very stable temperature control is required, then PID control is applied.

In PID control, P stands for Proportional, I for Integral and D for Derivative[82-84], and the combination of the three terms is the output of the PID control.

3.7.1 The proportional control

In proportional control, the controller output power O_p is made proportional to the temperature difference called the error term, e which is equal to the difference between the set point T_s and the measured temperature Tthus $\mathrm{e} = T_s - T$. The controller output can be written as,

$$O_p = e \times K_C = e \times \frac{O_{pmax}}{P_B} \qquad 3.1$$

Where K_C is the proportional gain, which determines the ratio of output response to the error signal. The control system response can be improved by increasing the proportional gain, however if the gain is too large, the temperature will oscillate off the set point and oscillate out of control. [85]

In practice K_C is replaced with the maximum available power, O_{Pmax} divided by a proportional band P_B. The temperature $T_s - P_B$ is where the maximum of the available power is used and below this temperature, the power is fully on. The power is proportional to e where the temperature is between T_s and $T_s - P_B$. For a wide proportional band, to maintain a constant temperature, the temperature increases slowly until the power is sufficiently reduced. This will cause the temperature to be below the set point, and the size of this offset will depend on the power required. The offset value will vary as the required power varies. By narrowing the proportional band, the amount of temperature variation is reduced however if the proportional band is too narrow, the controller will work as an on/off controller.

3.7.2 The integral and derivative term

The control can be improved by including integral and derivative terms. The terms can be added in different ways and the equation below is referred to as the ideal and is used in the present work[86].

$$O_p = \frac{O_{pmax}}{P_B}\left(e + \frac{1}{I}\int e\,dt + D\frac{de}{dt}\right) \qquad 3.2$$

The integral term will sum up the error term e over time. The additional output is proportional to the integral of the error term with time. This is,

$$\frac{1}{I_t}\int e\ dt \qquad 3.3$$

Where I_t is the integral time constant

When initially the temperature is too low and the error term e is positive, the power supplied to the system will increase. The temperature will gradually increase until it reaches the set point if the I_t term is large enough. If the I_t term is smaller, the temperature can oscillate about the set point. The integral term can be used with on/off and proportional control to eliminate the temperature offset.

The derivative term will cause the output to decrease when the temperature error is increasing. When the term is used, the output is made proportional to the rate of change of the error in temperature. The derivative term is,

$$d_t \frac{de}{dt} = -d_t \frac{dT}{dt} \qquad 3.4$$

Where d_t is the derivative time constant

The overall control system response can be sped up by increasing the derivative time term as this causes the control system to react faster to changes in error. When the temperature is rising towards the set point, $\frac{dT}{dt}$ term is positive ($\frac{de}{dt}$ is negative), by adding a derivative term will reduce the power.

3.7.3 Temperature tuning

The Ziegler-Nichols method can be used to tune the temperaturecontroller[87]. The tuning is performed by firstly turning off the integral and derivative terms. The set point is specified, and the proportional gain K_p is then gradually increased from zero. From the figure 3.28 below the tuning starts by adjusting the set point and inputting proportional gain from zero. When the oscillation starts to dampen, then the proportional gain K_p is increased, and when the

oscillation about the set point start to oscillate out of control, the K_p value is decreased. This process is repeated until the temperature has constant amplitude oscillation about the set point, where the K_p is taken and this value is considered the ultimate gain K_u. When the ultimate proportional gain K_u is obtained, the ultimate oscillation period T_u is also noted, which is the time for one oscillation to complete.

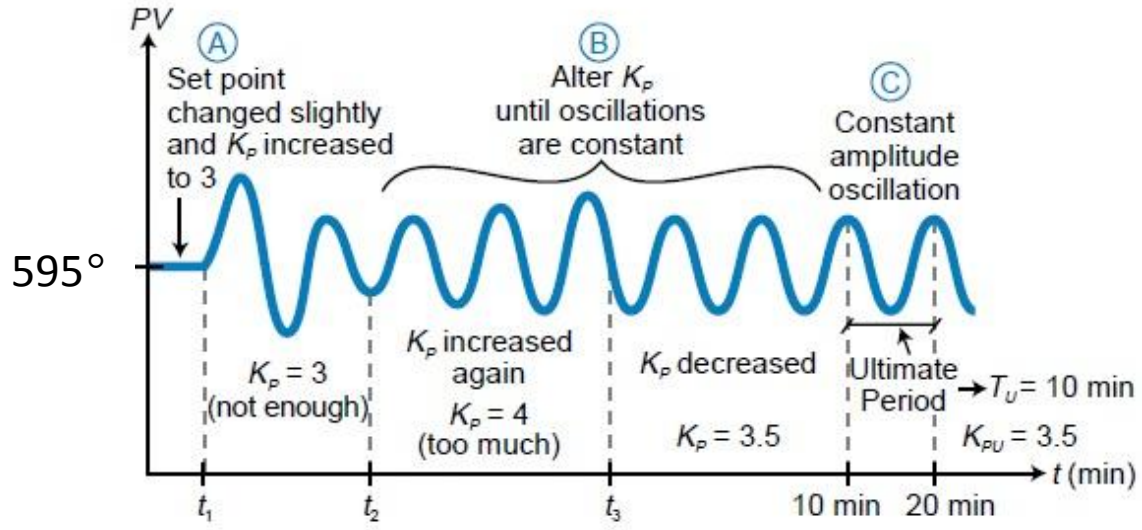

Figure3.28. An overview of the tuning process in simplified graph[88]

The value of K_u and T_u are then used to set the proportional, integral and derivative gains for the type of controller used using the Ziegler-Nichols coefficients below,

Ziegler-Nichols Method			
Control type	$\boldsymbol{K_p}$	$\boldsymbol{T_i}$	$\boldsymbol{T_d}$
P	$0.5K_u$	-	-
PI	$0.45K_u$	$T_u/1.2$	-
PD	$0.8K_u$	-	$T_u/8$
PID	$0.6K_u$	$0.5K_u$	$T_u/8$

Table3.4 Ziegler-Nichols coefficient to obtain PID values for input.[89]

The value of the gains for each P,I and D can be obtained from the coefficients above, and can be inputted for the temperature setting.

Another method of tuning the PID gains is called ‘half decay method’, where it follows a similar tuning method to the Ziegler-Nichols method. The ultimate gain value slightly modified K_u is found using the same method as Ziegler-Nichols, but then this K_u value is halved and inputted into the proportional gain input. Then the integral gain can be found by gradually increasing its value from zero until constant amplitude oscillation is obtained. And this is repeated for the derivative gain until the PID tuning is satisfactory for the accurate temperature control.

3.8 Experimental procedure

The figure below shows the schematic diagram of the set up that will be required to run the experiment.

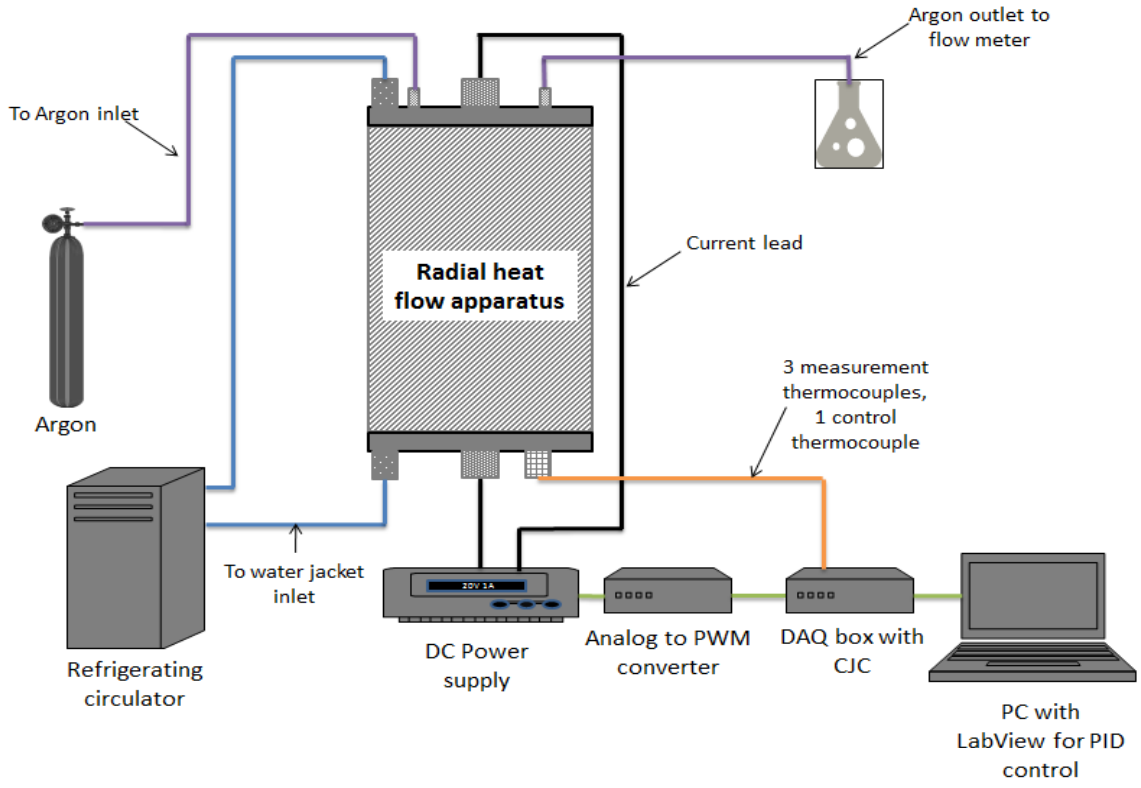

Figure 3.29 A schematic diagram of the complete system to run radial heat flow apparatus

The radial heat apparatus with capabilities of holding the specimen temperature to within ±0.05K for the duration of the experiment was required. This apparatus could operate at radial high temperature gradient mode of 10 to 20 K/cm, and at radial low temperature gradient mode of 0 to 1 K/cm. The high temperature gradient mode was used to run the experiment and to equilibrate the specimen, and the low temperature gradient mode was used to calibrate the thermocouples.

During the high temperature gradient mode to equilibrate the specimen, the specimen was heated by the central heating element which is a coiled Kanthal A1 wire of diameter 1.2mm inside a central alumina tube of inner diameter 5mm and outer diameter of 6mm and length 130mm. The central heating element was connected to a thick copper wire of diameter 6mm using high temperature connectors or high temperature crimps.

The water cooling jacket was placed outside the specimen to provide temperature gradient in radial direction at around 298K by using refridgerating circulator.

The temperature control was done by a thermocouple placed in the crucible next to the central alumina tube with a Labview software connected to DAQ box supplied by Measurement Computing, and the two thermocouples to the left of the central heating element at different distances away from the center was used to measure the temperature and the temperature was recorded using Labview into Excel. All three thermocouples were type K (Alumel/Chromel) and were sheathed in 1.2mm outer diameter alumina tubes and were placed half way up the sample. To check the vertical temperature gradient, a type K (Alumel/Chromel) thermocouple was used, sheathed in 2mm outer diameter alumina tube, placed on the right side of the central heating element, going all the way along the specimen.

The calibration of the thermocouples was carried out in situ with low temperature gradient mode. During the calibration, the water cooling jacket was empty, central heating element was used to heat the specimen to near eutectic temperature. By controlling the central heating element, the eutectic interface was moved very slowly past the thermocouples in a sequence of melting and freezing. The eutectic temperatures were the average of the two temperatures.

3.9 The final experimental setup

The set up was done in a step by step from inside out. Firstly the alumina tubes were cut and placed according to the size on bottom crucible lid. The alumina tubes were secured by using ceramic adhesives. This was left to harden and after the crucible body was placed on top of the bottom crucible lid, the bottom lid and crucible body was placed in an induction furnace, see figure 3.3. Thefurnace chamber was flushed with argon and the melting of the alloy was done by placing the alloy cubicles into the crucible. The alloy was melted and left to cool to room temperature.

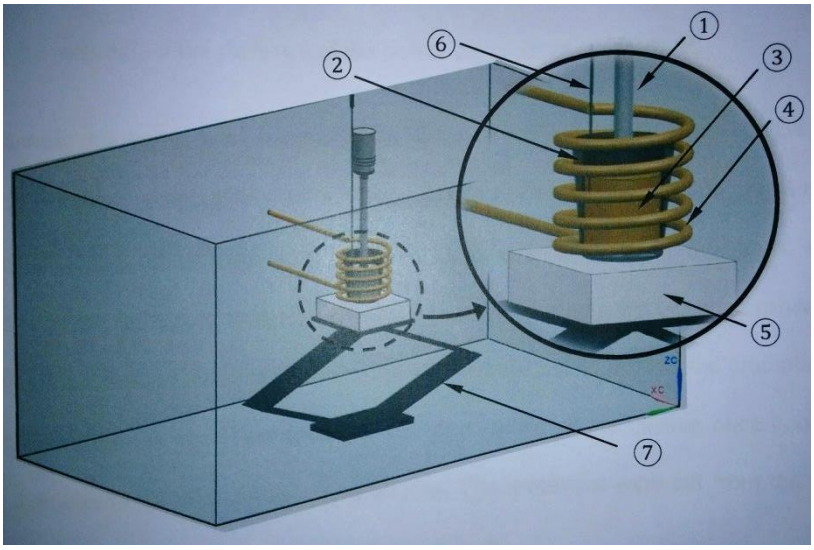

Figure 3.30 Induction furnace chamber with the following; 1) Stirrer, 2) machinable alumina crucible, 3) liquid alloy, 4) induction heating coil connected to power supply, 5) ceramic block, 6) K-type thermocouple, 7) screw jack

Then top crucible lid was placed on top to seal the crucible. The crucible was then removed from the induction furnace and placed inside the radial heat furnace with the thermocouples in place to start the experiment. The thermocouples were type K thermocouples sheathed in nickel alloy as it can measure temperatures of up to 1000 degrees.

The crucible consists of three parts which are the main body of the crucible and the top and bottom lids. The crucible body was machined from machinable alumina with inner diameter of 30mm, outer diameter of 46mm and height 100mm. The two lids were machined also from machinable alumina, to fit tightly onto both ends of the crucible body. The bottom crucible lid has holes drilled to fix alumina tubes for both the heating element and the thermocouples. The heating element was made of Kanthal A1 of diameter 1.2mm and was wound into a coil of 140mm to cover the entire length of the crucible including the lids. This was inserted into the center alumina tube. The three measurement thermocouples were inserted in through the alumina tubes placed in the bottom crucible lid, with one that is vertically moveable, and the other two placed at different distance from the center tube. The vertically moveable thermocouple was inserted to the whole length of the crucible, and the other measurement thermocouple and the control thermocouple was inserted to the half the length of the crucible.

To provide the temperature gradient, the alumina crucible is placed inside a water cooling jacket with a central bore, made of stainless steel. This provides the temperature gradient horizontally. The temperature in the water cooling jacket was kept constant by refrigeration bath. To prevent the temperature gradient from occurring vertically, two heaters are placed to fit onto either side of the crucible. Top and bottom heaters are made of machinable alumina and each holds a coil of Kanthal A1. The heaters are designed to fit onto the crucible lids.

The radial heat flow furnace was controlled by the Labview software which also recorded the temperature data. To be able to give high accuracy temperature control, the software needed to be controlled by PID controller. This was done in the Labview program, however it needed

tuning in order to give very accurate temperature control(±0.05K) over a long period of time (over 10 days). The tuning was done by using the tuning method explained in section 3.7.3.

A simplified schematic of the electrical set up to control the power to the heating element is shown in figure 3.31.

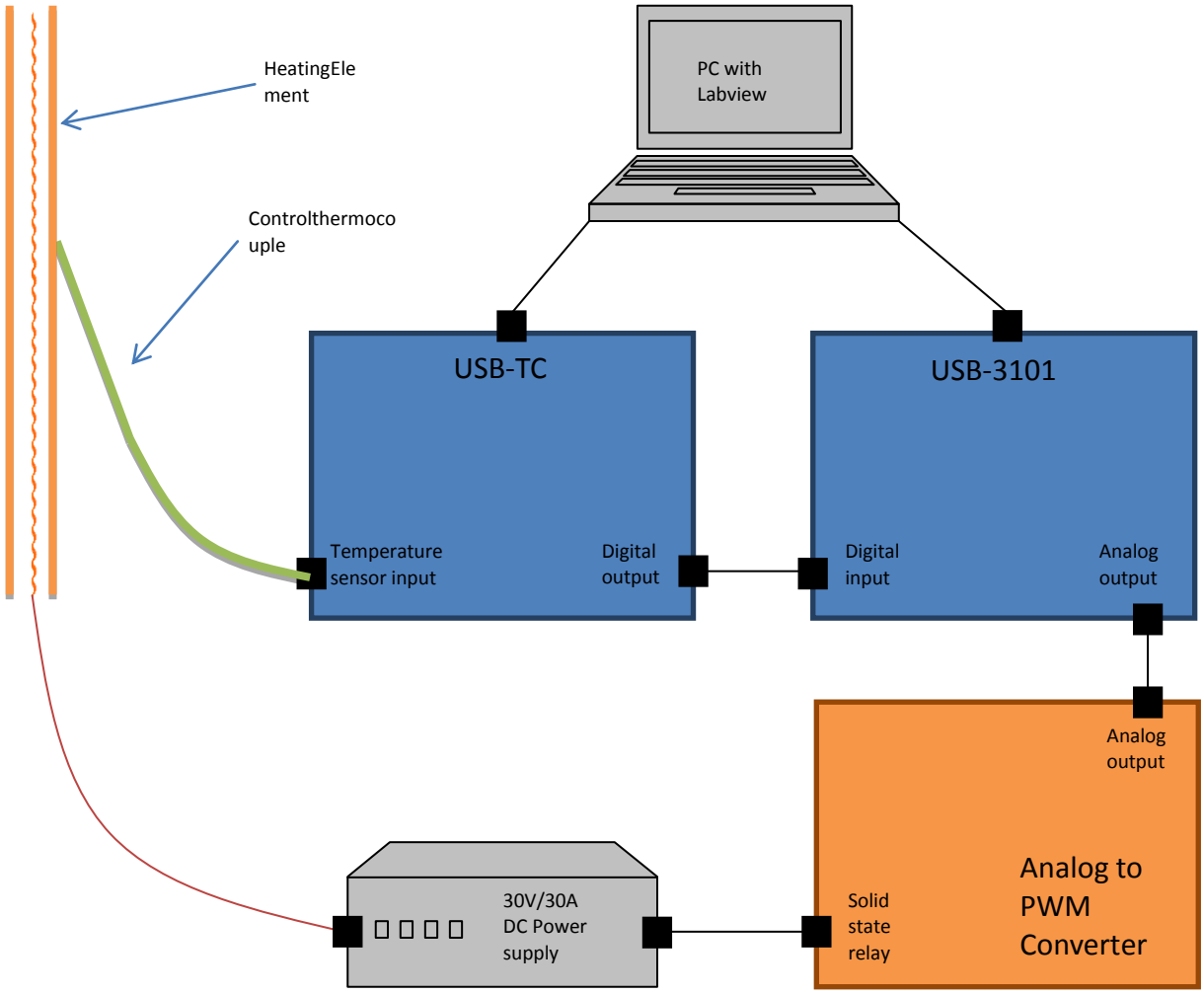

Figure 3.31 simple schematic of the control system used to control heating element

The Labview program was written to control thetemperature of the apparatus and to record the data. The power to the heating element was controlled as shown in figure 3.31. The control thermocouple was connected to a DAQ box from Measurement Computing called USB-TC. This DAQ box had temperature sensor input, which meant the K-type thermocouple could be

directly connected to the input port. Although the convenience of direct sensor input port, the USB-TC only supported digital output where analog output is normally desired. Thus another DAQ box, USB-3101,also from Measurement Computing was used. USB-3101 had digital input port, which could be fed straight from the digital output of USB-TC. Then the analog output from USB-3101 was connected to an 'Analog to PWM converter' which was built with solid state relay inside. This provided pulse output to control the DC power supply by on and off action. This DC power supply then was connected to the heating element to heat up the element. The control of the heating element was done by PID set in LabView.

The measurement thermocouples were connected to USB-TC directly and as USB-TC has direct temperature sensor input, the values were given as temperatures rather than voltages so the data was recorded to Excel using Labview.

The interface of the LabView program is shown in figure 3.32,

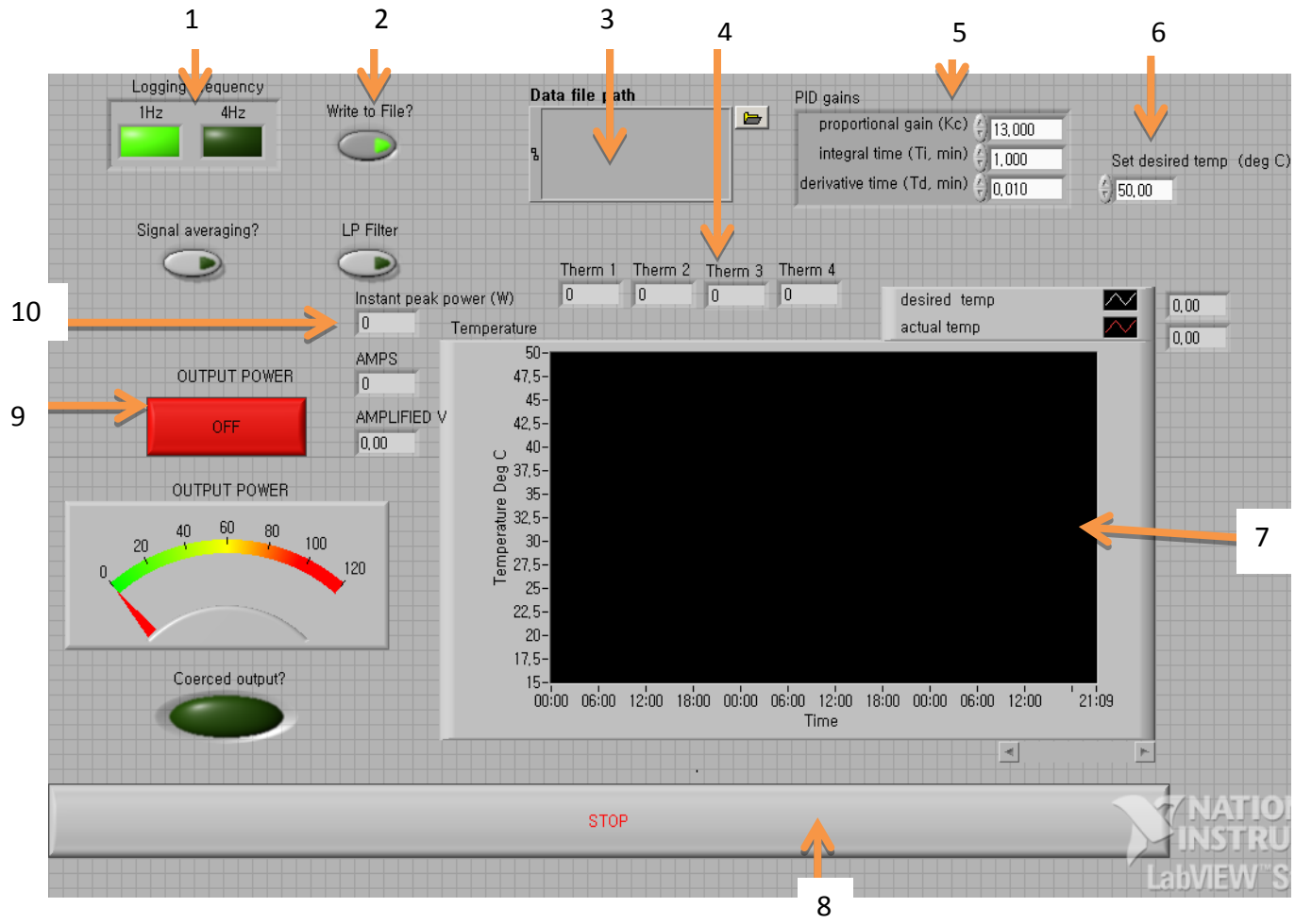

Figure 3.32 the LabView interface used to both control and record temperatures; 1) Logging frequency, 2) Switch to start recording, 3) File path to save data, 4) temperature readings for each thermocouples, 5) PID inputs, 6) Temperature set, 7) Temperature vs Time curve, 8) Stop button to abort all, 9) Output power to heating element On/Off switch, 10) Power supplied in Watts

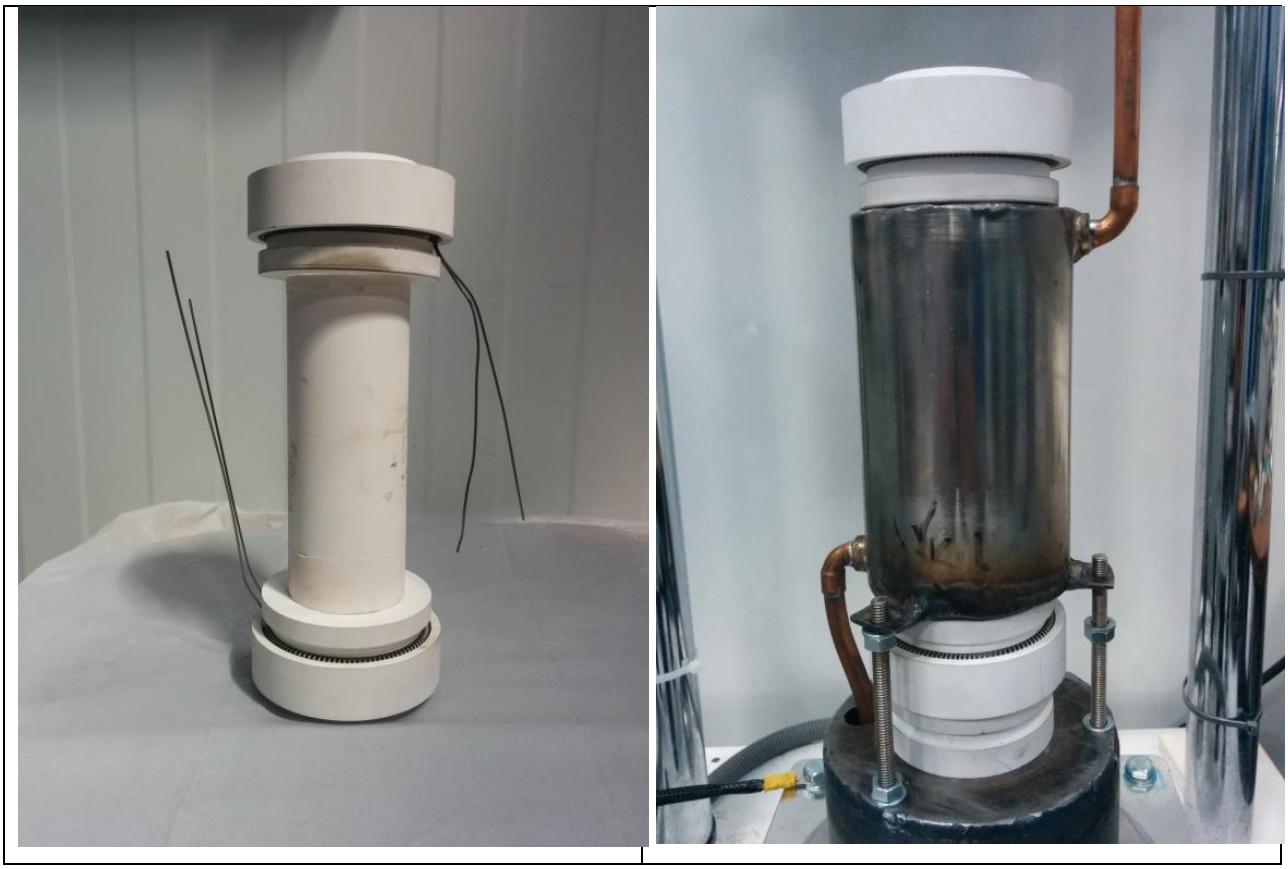

Figure 3.33The left show the crucible with top and bottom lid attached and also with the top and bottom heater, The right show the crucible placed inside the cooling jacket

Figure3.34The left shows the radial heat furnace filled with insulation, superwool, and the right shows the full set up of the experiment with the refrigeration bath

4 Experimental Results and Discussion

The object of this experimental work is to measure solid-liquid interfacial energy of aluminium alloy, LM25 which an aluminium alloy widely used in industry. The chemical concentration is listed in Table 4.1. The measurement of solid-liquid interfacial energy is difficult for both transparent and opaque materials. The most commonly used method in the last decade to measure solid-liquid interfacial energy is the method of observing grain boundary groove shape in a temperature gradient. Many attempts have been made by others based on the work done by Gündüz. This chapter will explain the method used to calculate thermal conductivity of the solid, and also the method to measure the grain boundary groove shape.

Al	Co	Cr	Cu	Fe	Mg	Mn	Ni	Si	Ti	Others
91.1	-	-	0.2	0.5	0.4	0.3	0.1	7.0	0.2	0.2

Table4.1. Chemical composition of LM25[90]

The thermodynamic database Thermo-Calc engine with DICTRA extension databases was used to plot the phase change against temperature of LM25 in equilibrium condition is shown Figure 4.1; the enthalpy change against temperature and heat capacity against temperature for LM 25 under equilibrium solidification condition are shown in Figure 4.2 and 4.3 respectively. The dash lines in the Figure 4.1, 4.2, 4.3 indicate the temperature used in experiments. The calculated equilibrium data will be compared experimental data and then to determine the temperature used in experiments.

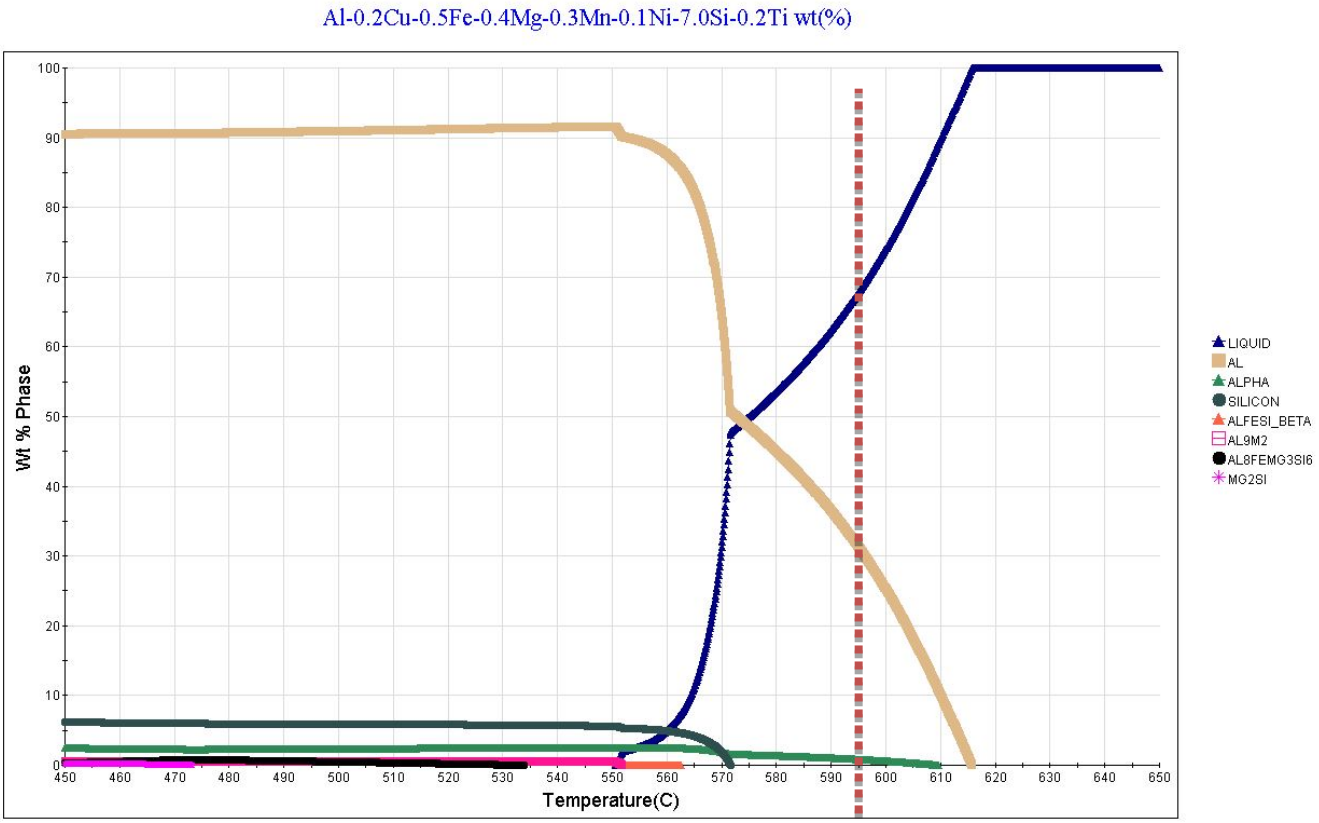

Figure 4.1 Phase change against temperature of LM25 in equilibrium condition

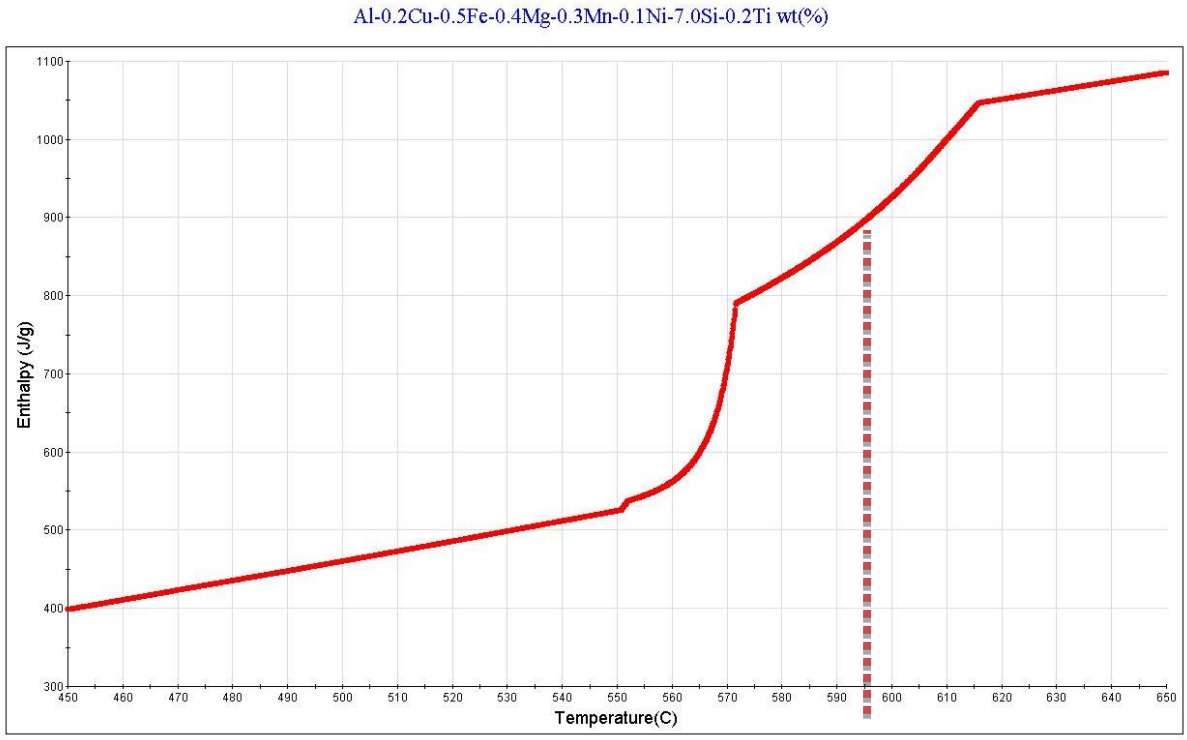

Figure 4.2 Enthalpy change over temperature for LM25

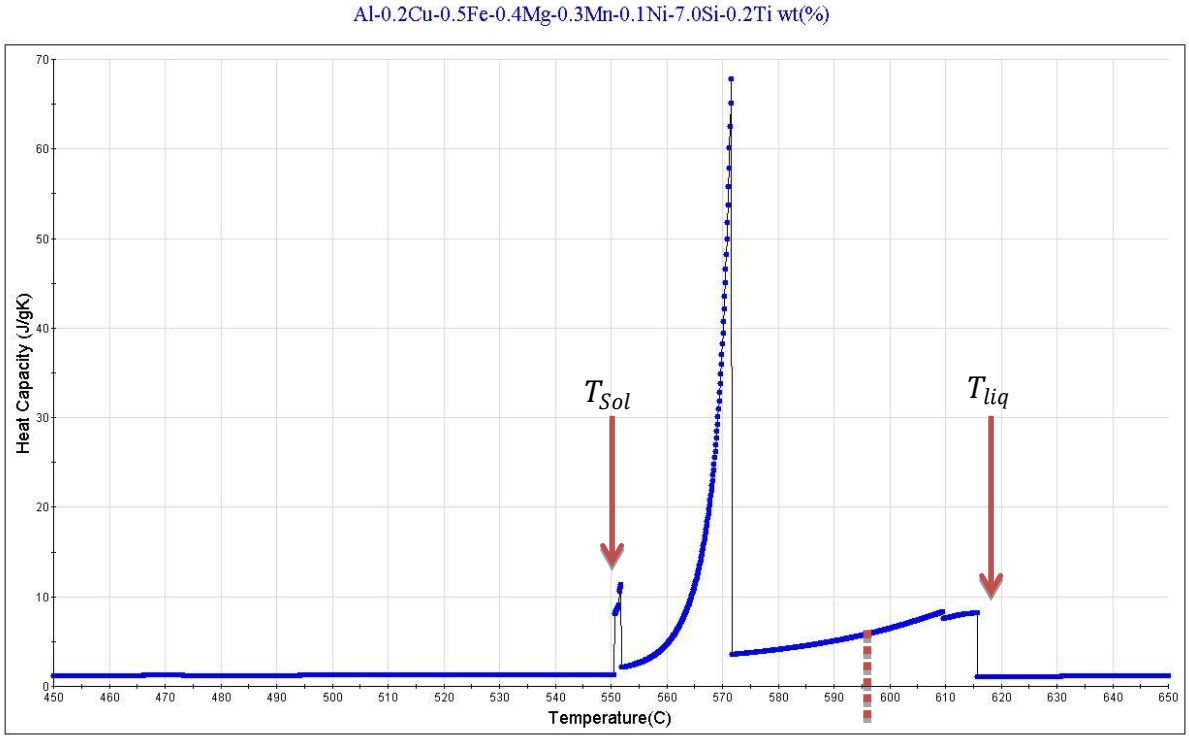

Figure 4.3 Heat capacity graph of LM25

The curves plotted for LM25 of phase diagram, enthalpy change and heat capacity show that it agrees well with the literature values as shown in table 4.2. The red dotted line in each curve represents the temperature at which the experiment was carried out.

T_{Sol}	T_{liq}	
550°C	615°C	[90]
567°C	614°C	[91]
554°C	614°C	[91]
568°C	612°C	Present work

Table 4.2. literature values for phase change temperatures and the value for present work

4.1 The cooling curve of LM25

Before the experiment was started, the thermocouples were calibrated, and this was done by slow heating and cooling to detect the melting point of the pure aluminium. After the calibration, the experiment was carried out on LM25. The radial heat furnace was heated up above the melting point of the alloy and after the furnace reached the desired temperature, the power was switched off and the cooling temperature curve of the alloy was recorded. The cooling curve is recorded and the phase change temperature was compared to the results in the literature. The phase change temperature obtained by this process was in good agreement with the values in the literature and the calculated values in equilibrium condition (very slow cooling).

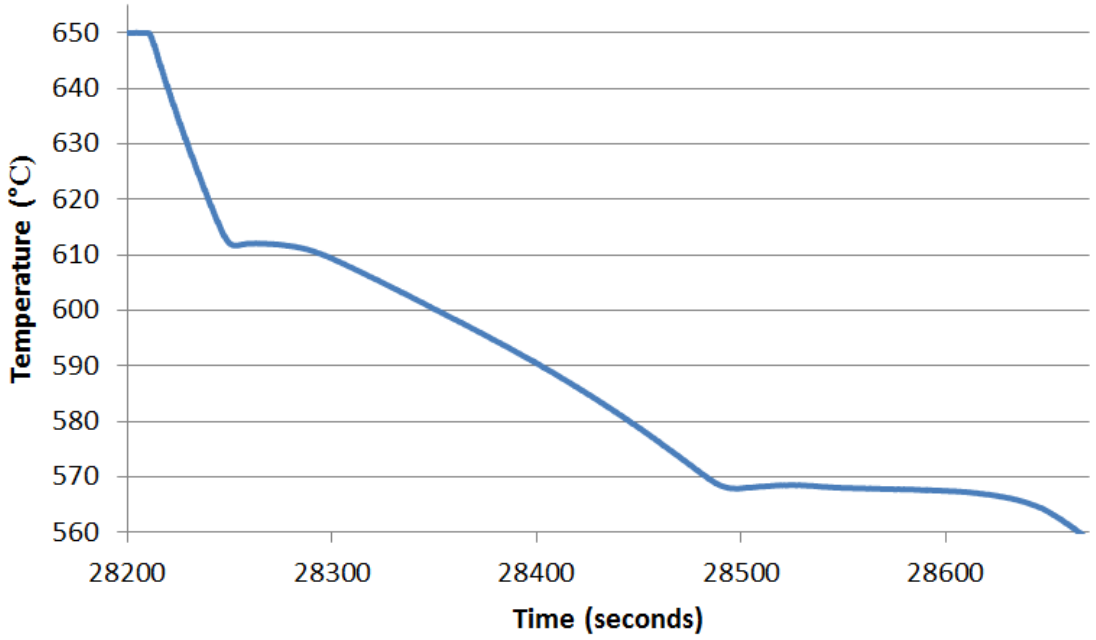

Figure 4.4 The cooling curve of LM25 from above the melting point to below the solidifying temperature

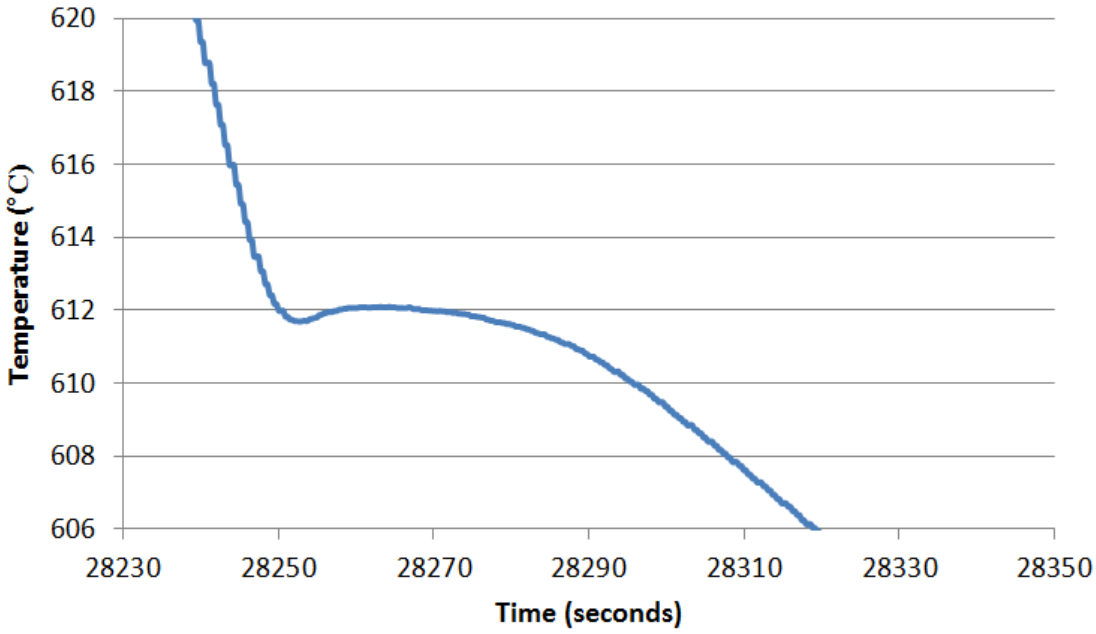

Figure4.5. The cooling curve at the melting temperature of LM25

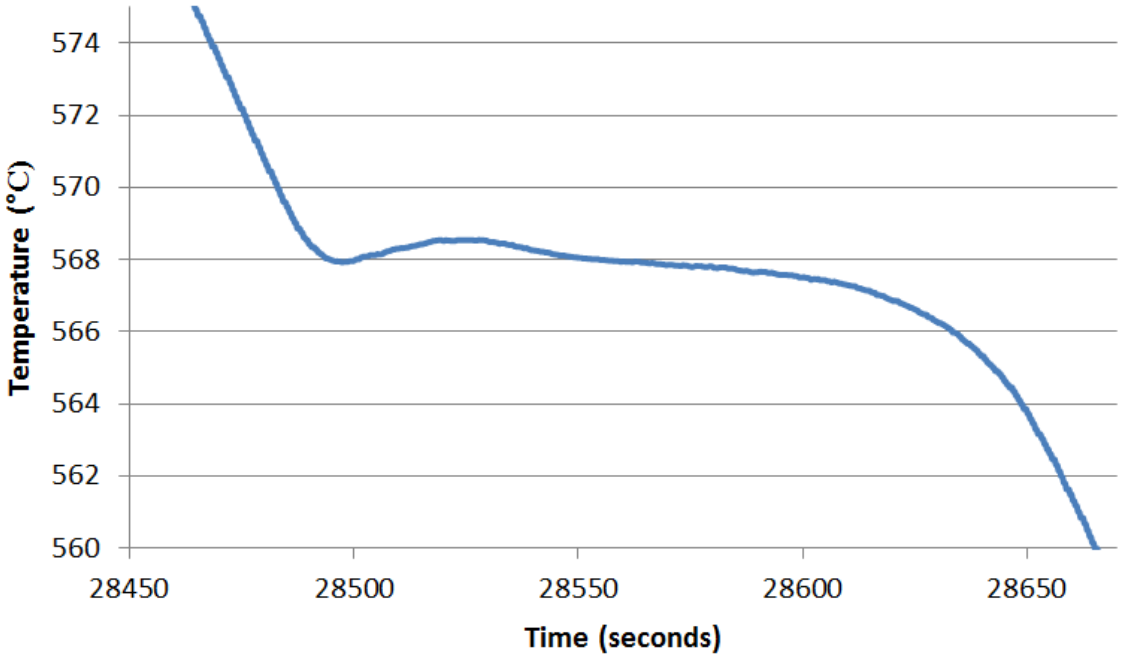

Figure 4.6 The cooling curve at the solidification temperature

4.2 Obtaining the equilibrated grain boundary groove shape

The purpose of the experiment was to obtain a thin liquid layer in the centre of the crucible, and establish a radial temperature gradient to get the solid liquid interface and groove shape. The central heating element was made of Kanthal A1 wire and controlled by Labview using K type thermocouple placed next to the heating element. The temperature in the sample was controlled to a very high accuracy (±0.05K) over the duration of the experiment which was more than 10 days. The solid liquid interface shape was obtained by rapidly cooling the sample at the end of the annealing time, by switching off the power.

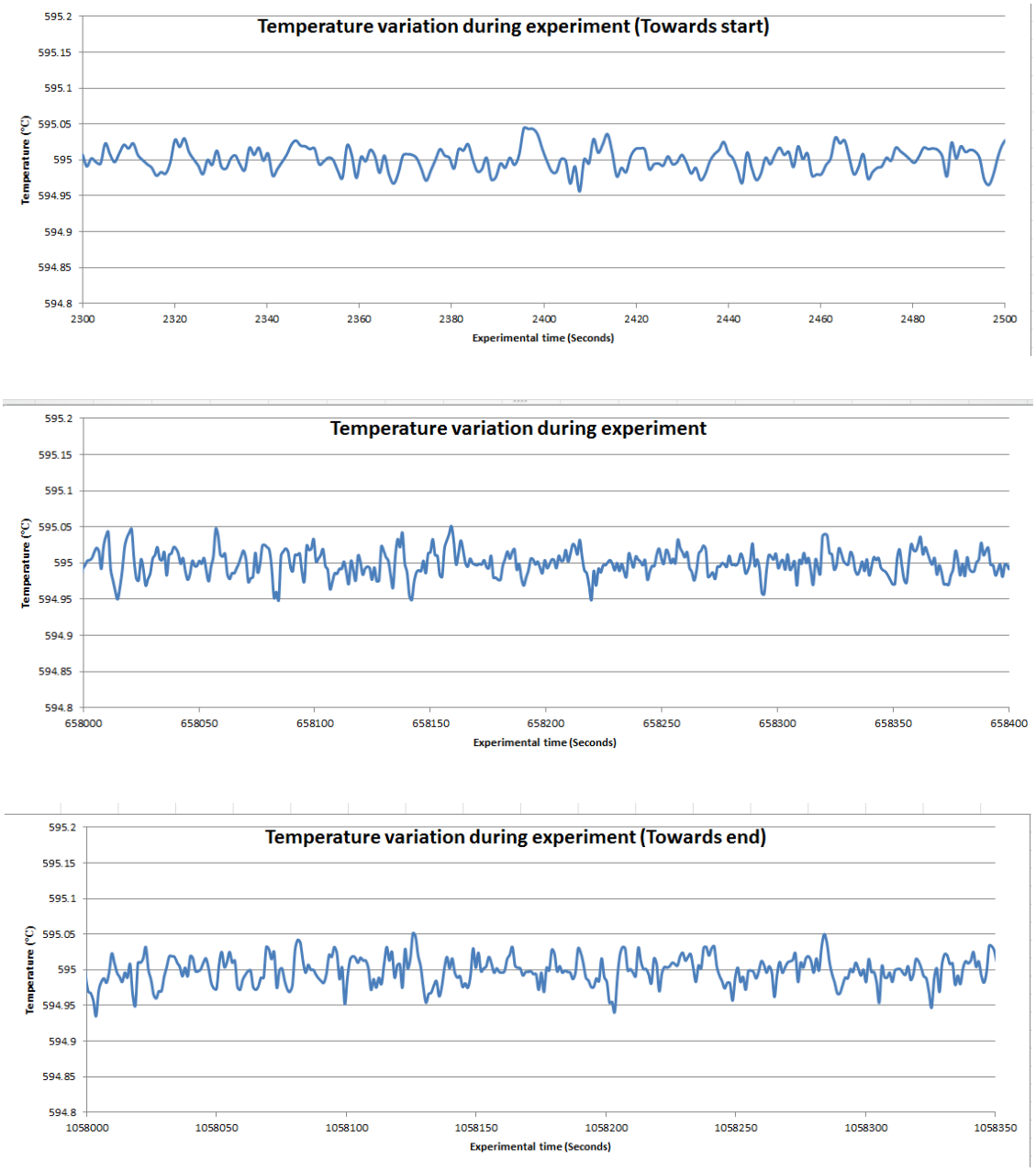

Figure 4.7. The recording or temperature shows that the control accuracy was maintained at ±0.05°C for the duration of the experiment; At the beginning, during, and at the end of the experiment

The temperature control achieve by the novel apparatus was a vast improvement on the works carried out by Maraşlı and Hunt[80], as they achieved control of ±0.08K over 2-4 day period.

The quenched sample was taken out of the crucible and cut into small discs of height around 15-20mm. The samples were mounted using conductive phemolic mounting resin, and grinding was done using SiC abrasive paper in steps. The grinding was done in 5 steps, with abrasive paper with largest grit size 240 (58 micron) first and working down to grit size 600 (15 micron). Between each grinding steps, the sample was cleaned using green soap and ethanol. After grinding process was complete, the sample was polished using non-ferrous fibre pads. The polishing was done in 2 steps, first with larger fibre size at 6µm and then with fibre size 1µm. Also the sample was cleaned after each polishing step using green soap and washed off using ethanol. The last polishing was done using a colloidal silica pad. At the end the samples were cleaned and dried. The etching was carried out to reveal the grain boundary structure to be viewed under optical microscope. For the present work, Keller's etch was used to etch the samples.

The examinations of the samples were done under Olympus GX51 optical microscope and the grain boundary groove shape was also photographed using Olympus SZX12. The below show some of the groove shapes obtained for LM25.

a)

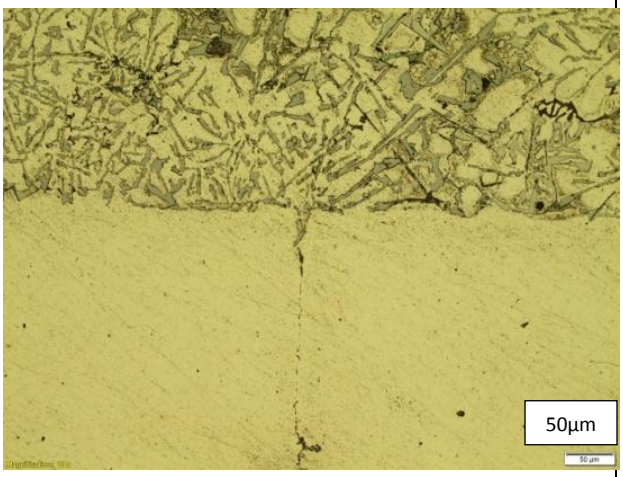

b)

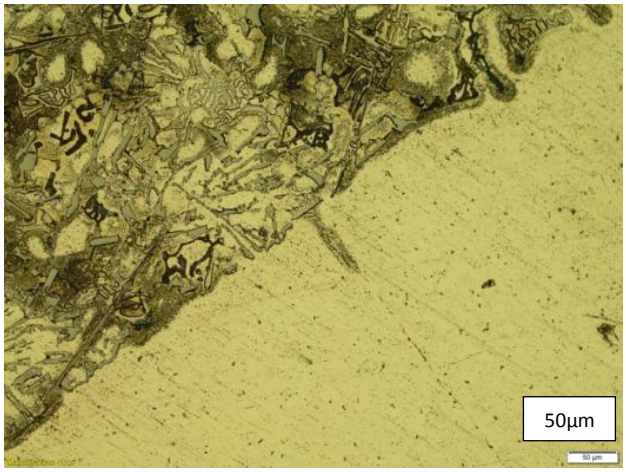

c)

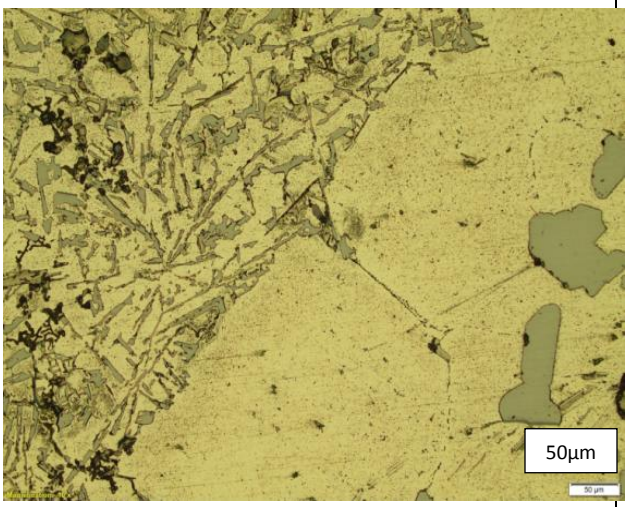

d)

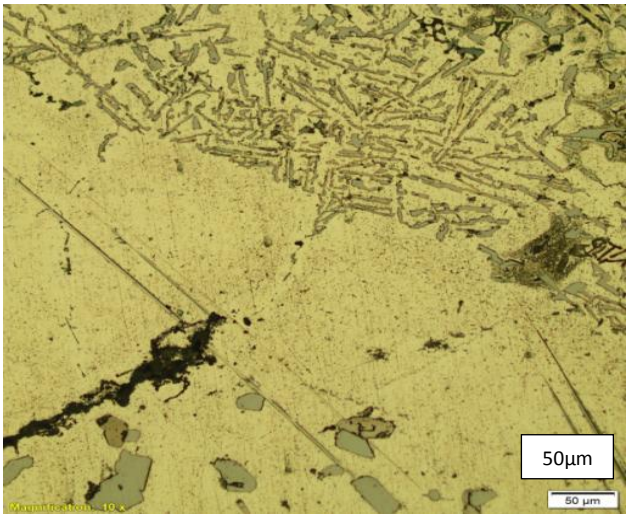

e)

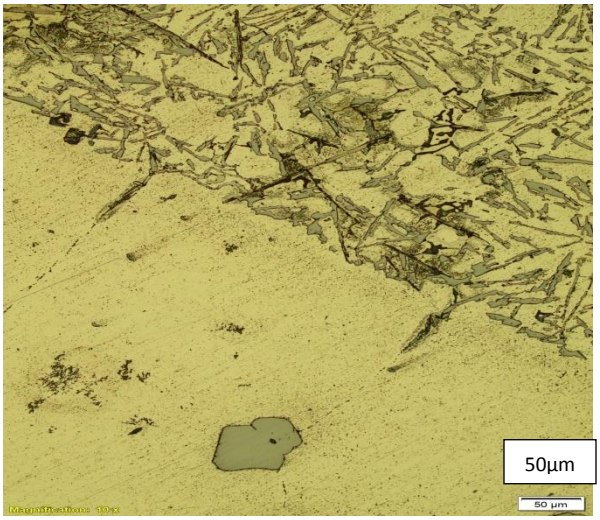

f)

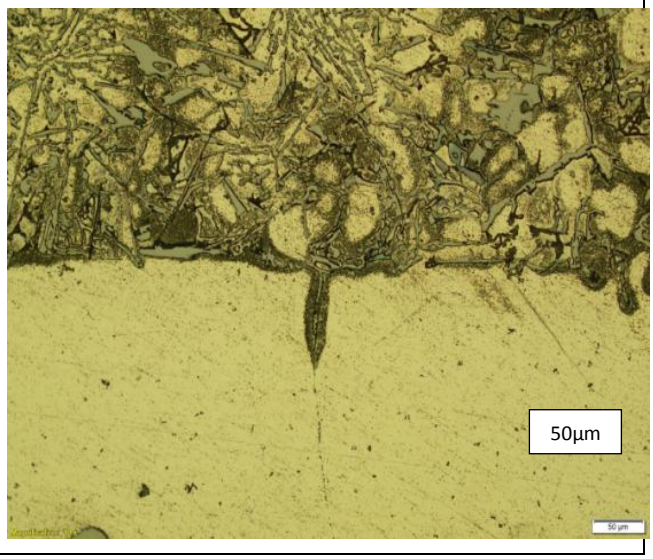

Figure4.8. The optical microscope images obtained from the experiment showing grain boundary groove shape at 50µm scale

a)

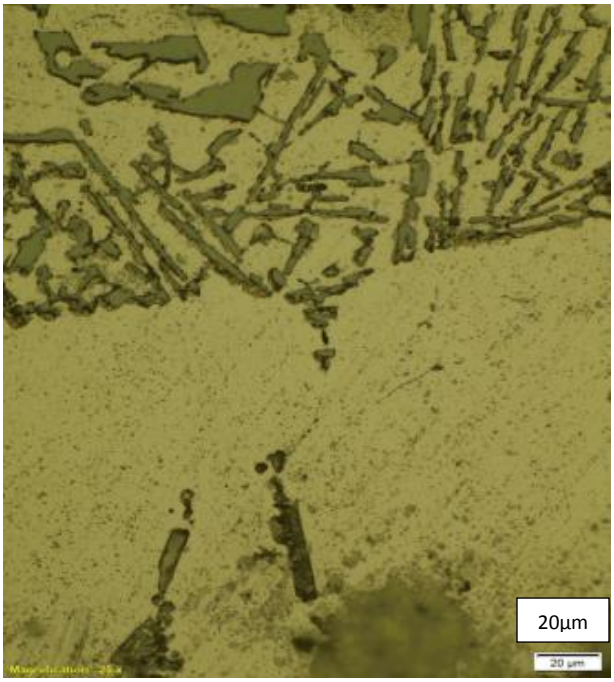

b)

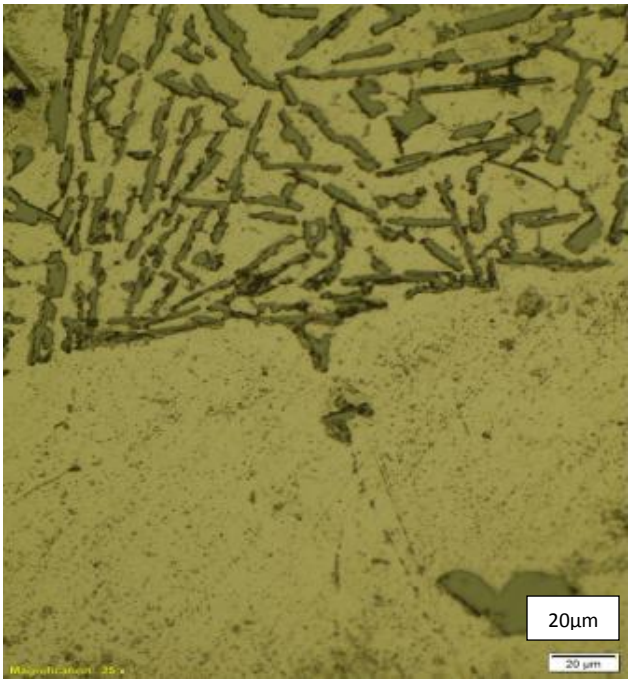

c)

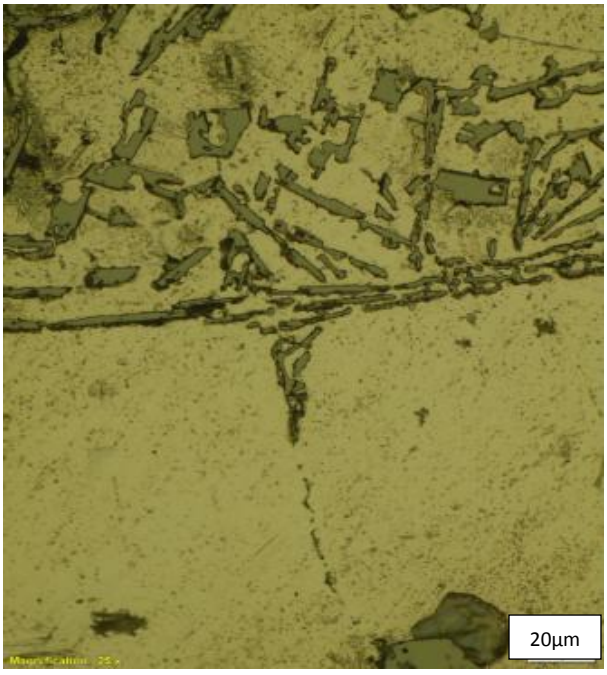

d)

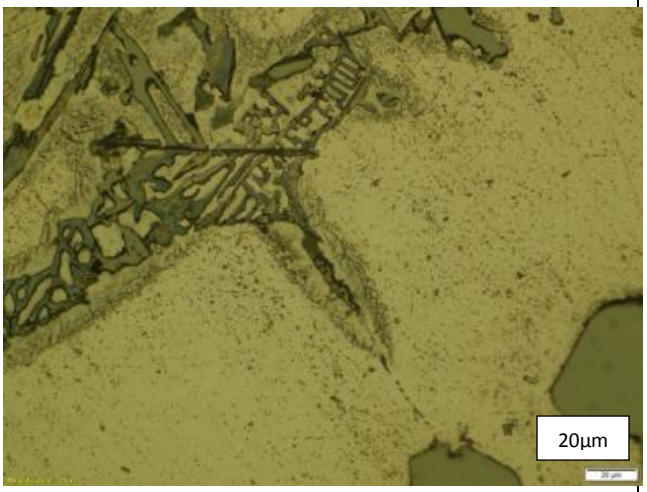

e)

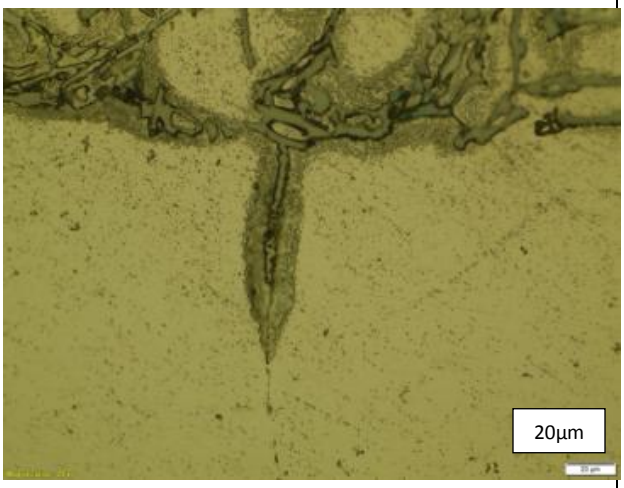

f)

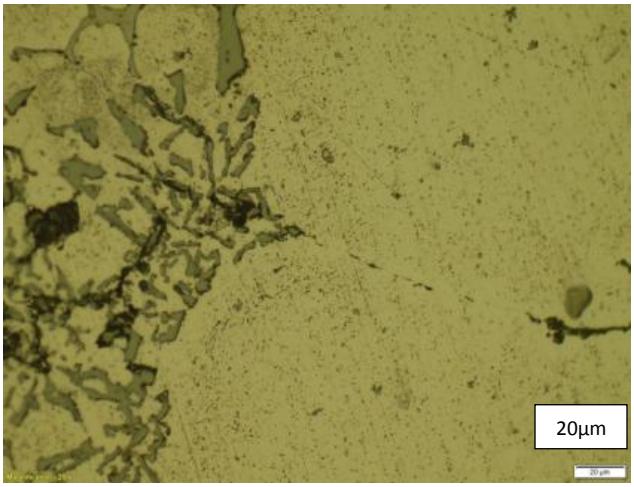

g)

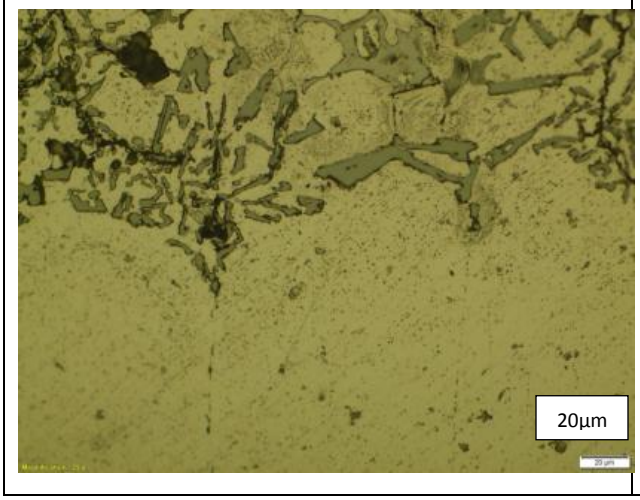

h)

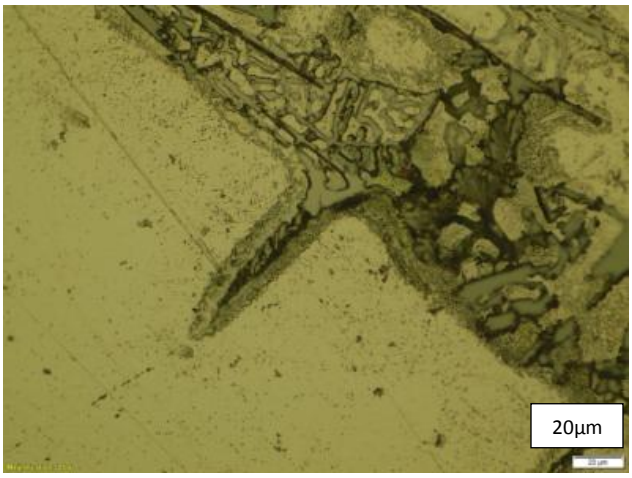

i)

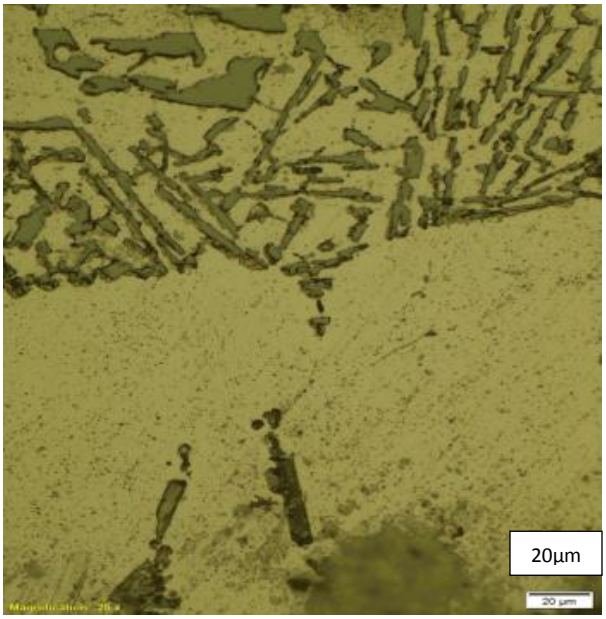

Figure 4.9 Optical microscope images of grain boundary groove shape at higher magnification at 20µm scale

The grain boundary groove shapes obtained from the experiment vary in shapes, size and depths. For example in figure 4.8 c) and e), the groove shape is not symmetric about the grain boundary and also the groove is skewed. For the grooves infigure 4.9 d),e) and h), the groove shape is very steep and has grey shade around the groove, which could be eutectic.These grooves would be rejected when applying Gibbs Thomson equation as the groove shape would be too steep and the groove curve is not clear. A good example of the groove to be used in the analysis would be in figure 4.9 i).

4.3 Temperature gradient measurement

Radial heat flow apparatus was chosen as symmetrical nature of the radial heat flow apparatus allows temperature gradient in radial direction and may give more stable temperatures.

Fourier's law can be used to represent temperature gradient for radial heat flow and it states that the heat flow rate through a material is proportional to the negative gradient in the temperature and the area perpendicular to the gradient at which the flow of heat occurs.

Fourier's law gives the temperature gradient, G_S, at the steady state condition which is,

$$\frac{dT}{dr}(G_S) = -\frac{Q}{AK} \qquad 4.1$$

Where Q is the constant heat flow, k is the thermal conductivity, A is the area

As the apparatus will produce a cylindrical sample, for radial heat flow, area, A, will become $A = 2\pi rl$. Thus giving,

$$dT = -\frac{Q}{2\pi lK}\frac{dr}{r} \qquad 4.2$$

Integrating equation 4.2,

$$\int_{T_1}^{T_2} dT = -\frac{Q}{2\pi lk}\int_{r_1}^{r_2}\frac{dr}{r} \qquad 4.3$$

gives,

$$T_2 - T_1 = -\frac{Q}{2\pi lk}\ln\left(\frac{r_2}{r_1}\right) + C \qquad 4.4$$

Where T_2, T_1 are the temperatures at radii r_2, r_1 away from the center respectively, C is an arbitrary constant, l is the length of the central heating element

If $T_2 = T_1$, $r_2 = r_1$ or Q=0, then C=0, thus giving,

$$\frac{T_2 - T_1}{\ln\left(\frac{r_2}{r_1}\right)} = -\frac{Q}{2\pi lk} \qquad 4.5$$

And dividing equation 4.5 by r, gives the temperature gradient as,

$$G \equiv \frac{dT}{dr} = -\frac{Q}{2\pi rlk_s} = -\frac{\Delta T}{r\ln\left(\frac{r_2}{r_1}\right)} \qquad 4.6$$

k_s is the thermal conductivity of the solid phase.

Using equation 4.6 for a cylindrical sample, the temperature gradient can be found against the total input power i.e. heat flow, Q, and against the distance from the center of the sample, i.e. radius, r. There are two ways to achieve the desired temperature gradient at the interface and one is to set the solid liquid interface at the required distance from the center by using varying sizes of the central alumina tube, and the other is change the total input power.

4.4 Thermal conductivity of the solid phase

The radial heat flow apparatus can be used to measure the thermal conductivities of solid, and this value is needed to determine the temperature gradient and the Gibbs Thomson coefficient.

By integrating the equation for temperature gradient, gives,

$$K_S = \frac{1}{2\pi l} \ln\left(\frac{r_2}{r_1}\right) \frac{Q}{T_1 - T_2} \qquad 3.7$$

Where r_1 and r_2 are fixed distances from the center of the sample, and T_1 and T_2 are temperatures that correspond to their radius

At a given power level, the thermal conductivity can be obtained by measuring the temperature difference between two fixed points. However, the error in the calibration of the thermocouples means that the errors may be as large as the difference in temperatures. This can be overcome by measuring the temperature difference for two different power levels. i.e. different Q values.

Thus

$$K_S = \frac{1}{2\pi l} \ln\left(\frac{r_2}{r_1}\right) \frac{\Delta Q}{\Delta T_1 - \Delta T_2} \qquad 3.8$$

Where ΔQ is the difference in input power, ΔT_1 and ΔT_2 are the temperature difference at r_1 and r_2

To calculate the thermal conductivity of solid phase, the cylindrical sample was placed inside the radial heat flow apparatus. It was necessary to achieve a large temperature gradient in order to obtain a reliable thermal conductivity measurement. The sample was positioned so that it was placed inside a water cooling jacket, which was held at 293K using refrigerating circulation bath. The temperature gradient was achieved by heating the sample from the center using Kanthal A1 heating element wire. The sample was heated up in steps of 50K up to 10K below the melting point of the sample and was held at each set temperature for more than 2 hours to achieve steady state.

The control and measurements were carried out using LabView software and the measurements were saved. Once the measurement procedure was completed, the sample was removed and cut transversely to observe the values for r_1 and r_2.

a)

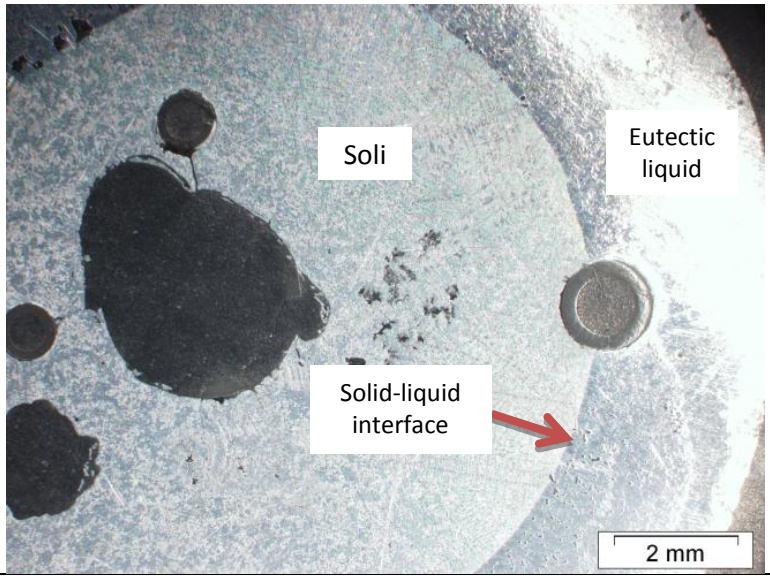
Soli
Eutectic liquid
Solid-liquid interface
2 mm

b)

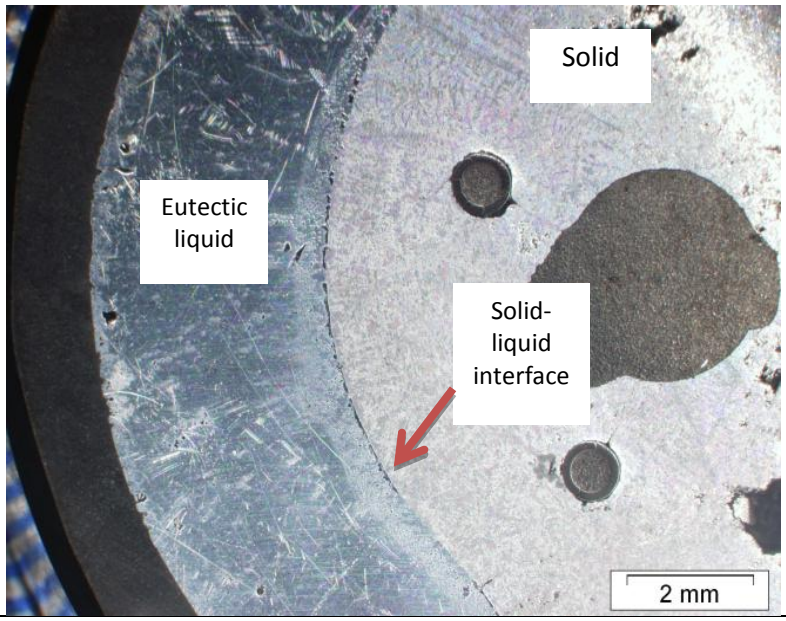
Solid
Eutectic liquid
Solid-liquid interface
2 mm

c)

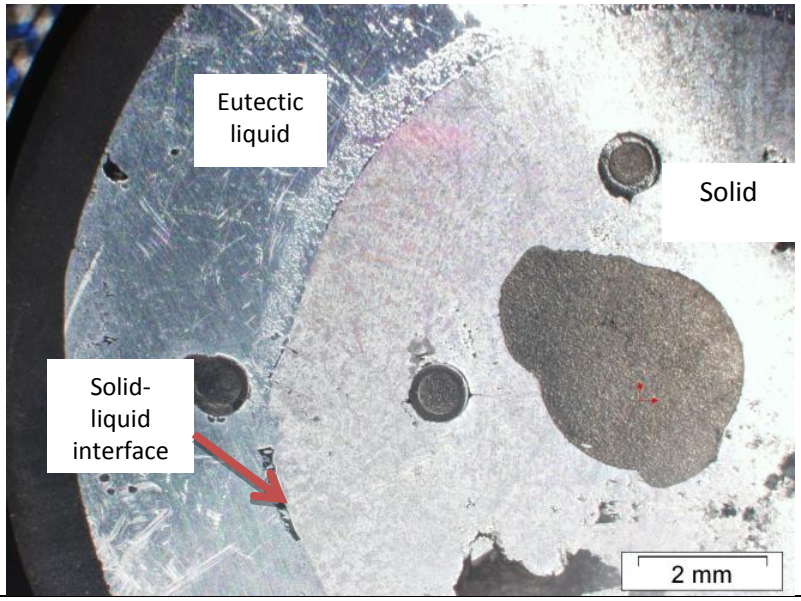

d)

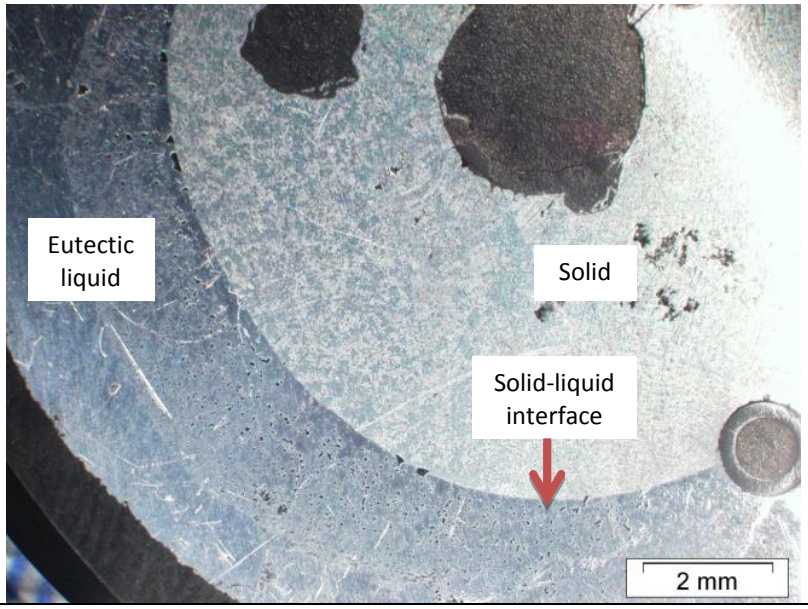

Figure4.10. the mounted samples showing the visible solid-liquid interface between the solid and eutectic liquid

The above figure 4.10 and several other cut samples were used to calculate the thermal conductivity of solid phase, and to validate the result it was plotted against a literature.

Set temp(℃)	T_1 (℃) (Temperature at R_1)	T_2 (℃) (Temperature at R_2)	T_1 - T_2 (℃)	Power (W)
100	99.5225	99.9483	0.4257	32.58
	98.5369	99.2315	0.69463	37.89
150	149.8162	149.1189	0.6973	49.57
	146.884	148.066	1.182	63.215
200	199.5289	198.5179	1.011	76.89
	194.87	196.6909	1.8209	92.606
250	248.0287	246.6743	1.3541	107.778
	242.6475	245.0688	2.5213	124.027
300	297.234	295.5409	1.6931	143.001
	289.166	292.5404	3.3744	158.7289
350	346.6897	344.7702	1.9195	168.21
	335.6602	340.0704	4.4102	193.1392
400	393.9615	396.1458	2.1843	200.93
	381.9675	387.5323	5.5648	230.4567
450	445.6848	443.1164	2.5684	238.17
	428.1492	435.0612	7.4628	266.857
500	495.2134	492.1756	3.0378	276.26
	471.7944	480.1738	8.3794	299.5927
550	544.604	541.0623	3.5417	316.21
	515.8748	525.9719	10.0971	337.6052
600	593.2729	587.8116	5.4613	347.831
	570.7549	580.5296	9.7747	388.724
650	644.0339	634.9202	9.1137	393.75
	598.0265	609.7466	11.7201	421.2053

Table 4.3. Values used for calculating thermal conductivity

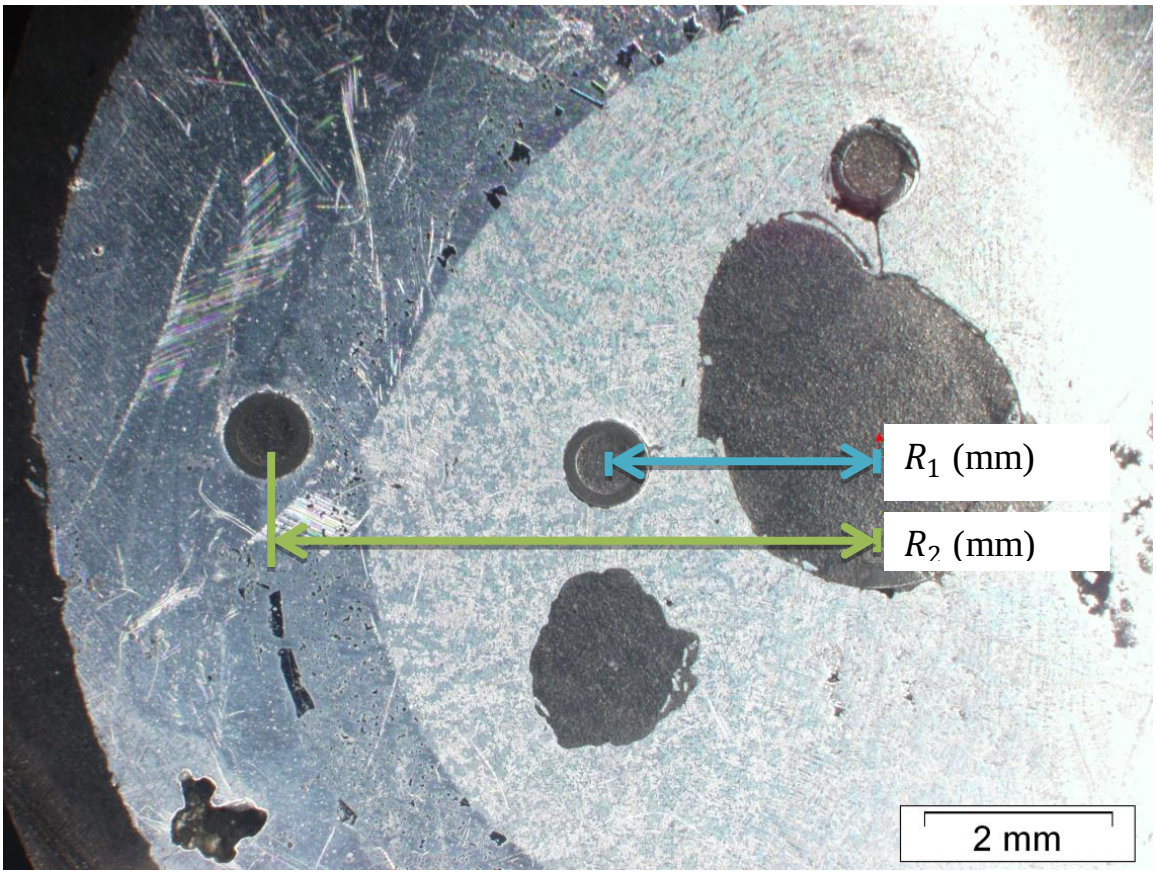

Figure4.11 the radii values at the points where the temperatures were measure for inner and outer thermocouples.

On figure 4.10 and 4.11, the samples show imperfections on the surfaces, and that could have arisen from tearing of the alloy as the alloy was being polished. The centre hole for the heating element is showing as not circular for the same reason. The solid liquid interface on some samples appears non circular, which could mean the apparatus may not be supplying radial heat flow along the full length of the furnace. This may not give ideal groove shapes for analysis, however this needs to be compensated for in application of the Gibbs Thomson equation and in error accumulation calculations.

For the experiment, the length of the heating element was 110mm±0.5mm and R1 was 1.58mm±0.01mm and R2 was 6.51mm±0.01mm.Thermal conductivity values were calculated using equation 3.8 with experimental data listed in table 4.3. The calculated thermal ductility data are plotted together Mill's values and the data for pure Al [92] for a comparison.

Considering the difficulties in obtaining accurate temperature and power measurements, it can be concluded that a good agreement with similar trends has observed in thermal conductivity measurement in the developed apparatus.

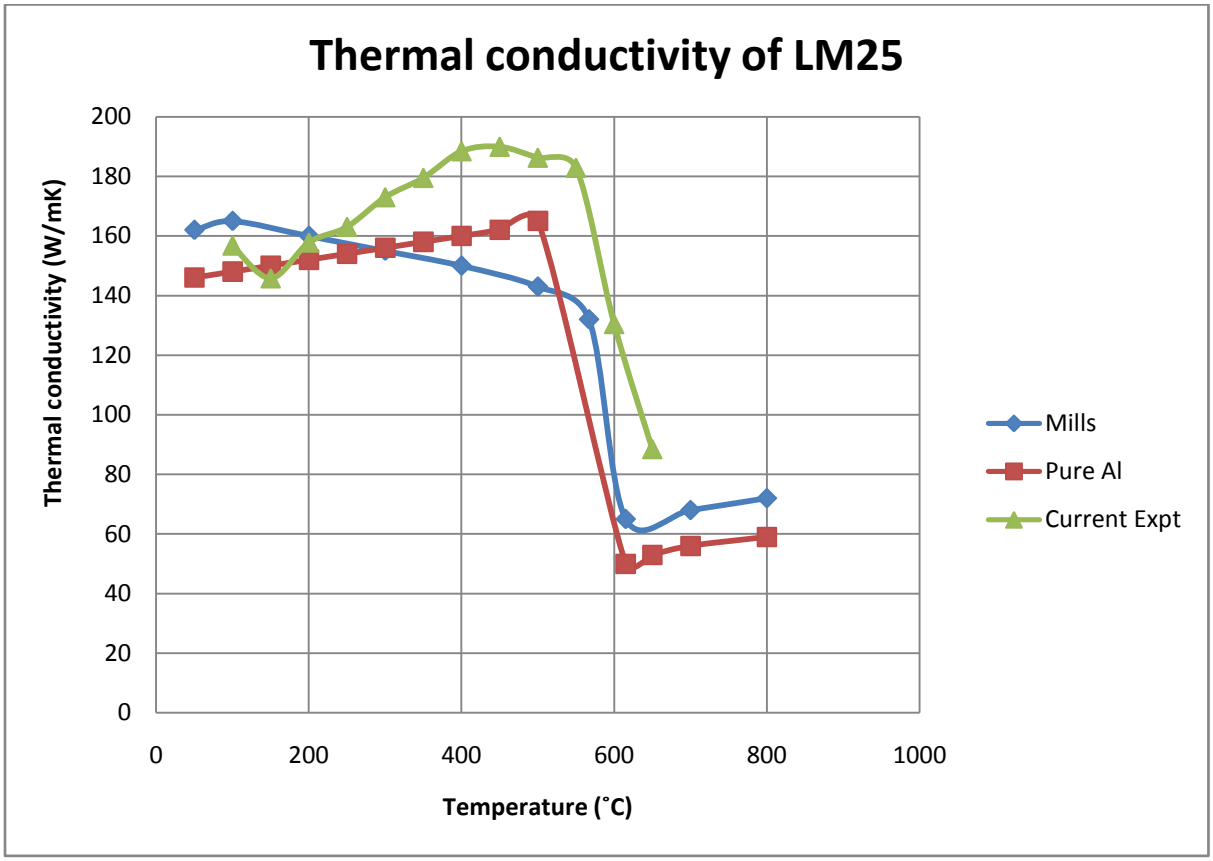

Figure4.12 Thermal conductivity value calculated for the present work compared to the literature.[92]

The result for thermal conductivity of LM25 from the current experiment in figure 4.12 generally compares reasonably well with the published data at lower temperatures of up until 250°C, however it shows a different trend of increasing in thermal conductivity value until the melting point whereas the Mills result show a decrease in thermal conductivity value before melting point. The discrepancy just before the melting point is as large as 30 percent, and as the thermal conductivity value is used in the calculation of solid liquid interfacial energy, this discrepancy needs to be taken into account in the possible error calculation.

4.5 Numerical method used to evaluate the Gibbs Thomson coefficient

It was found that the most common technique of measuring the solid-liquid interfacial energy is the grain boundary groove method. In this method, the solid-liquid interface is equilibrated with grain boundary in a temperature gradient and by measuring the equilibrium shape of the grain boundary groove profile, the solid-liquid interfacial energy can be measured.

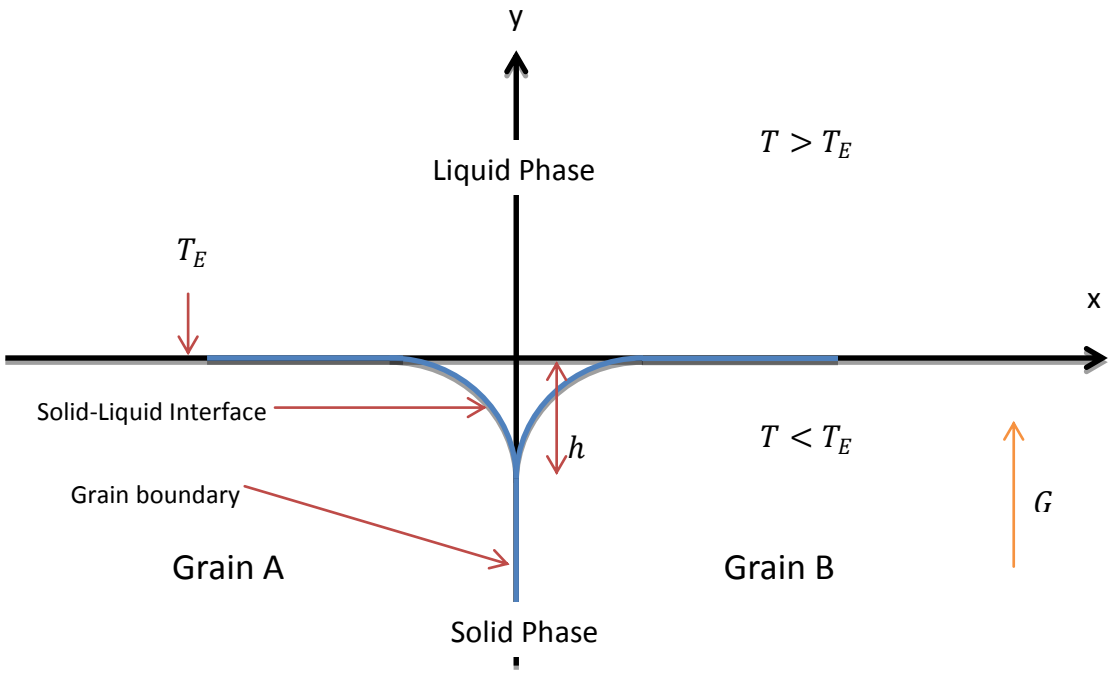

Figure.4.13 Schematic of the equilibrated grain boundary groove shape

As written in chapter 2, Jones[94], Jones and Chadwick[93] and Schaefer et al[43] have done works to estimate solid-liquid interfacial energy for transparent materials by using direct measurement technique based on Bolling and Tiller's[36] analysis of the grain boundary groove profile in an applied temperature gradient. However this method can only be applied for the cases where the system have equal solid and liquid thermal conductivity values.

Nash and Glicksman[37] then developed a method to calculate solid-liquid interfacial energy for the systems where the solid and liquid thermal conductivity values were different to one

another. However the numerical method by Nash and Glicksman is complicated and difficult to apply.

Gündüz and Hunt[45,46] developed a numerical method which calculates the temperature along the measured interface and the grain boundary groove shape rather than predicting the equilibrium shape. This numerical method can be used to calculate the Gibbs-Thomson coefficientΓ, for a measured interface shape if the temperature gradient of the solid phase and the thermal conductivities of both solid and liquid phases are known. In the present work, the Gibbs Thomson coefficient will be calculated using a similar numerical method.

A schematic diagram of an equilibrated grain boundary groove profile is shown in figure 4.13 .The shape of the profile depends on the temperature at the interface $T_e(x,y)$, the angle at the junction of the interface formed by the balance of surface tensions and the solid-liquid interfacial energy,σ_{SL}. The Gibbs Thomson equation for the cased shown in figure 4.13 can be written as,

$$\Gamma = (T_{I(\infty,0)} - T_{I(x,y)})r_{(x,y)} = \frac{\sigma_{SL}}{\Delta S_f} \qquad \textbf{4.9a}$$

$$\Gamma = \Delta T_r r_{(x,y)} = \frac{\sigma_{SL}}{\Delta S_f} \qquad \textbf{4.9b}$$

Where Γ is the Gibbs Thomson coefficient, $T_{I(\infty,0)}$ and $T_{I(x,y)}$ are the equilibrium temperatures on the flat interface and the curved interface, and ΔS_f is the entropy of fusion per unit volume

In this equation the Gibbs Thomson coefficient for the obtained groove shape can be calculated if ΔT_r is known. To do this equation 4.9 is integrated from flat interface to a point along the groove shape, which gives

$$\int_{0}^{-y} \Delta T_r \, \mathrm{dy} = \Gamma \int_{0}^{-y} \frac{1}{r} dy \qquad 4.10$$

The right hand side of the equation 4.10 can be calculated by observing the grain boundary groove shape. The left hand side of the equation 4.10 can be calculated if ΔT_r is known as a function of distance. The finite difference numerical model can be used to solve the left hand side by calculating the temperature difference between the flat interface and points along the groove shape, which is

$$\int_{0}^{y} \Delta T_r \, \mathrm{dy} = \sum (\boldsymbol{y_1} - y_2)\left(\frac{\Delta T_1 + \Delta T_2}{2}\right) \qquad 4.11$$

4.5.1 Evaluation of the Gibbs Thomson coefficient

The Gibbs Thomson coefficient can be written as,

$$\int_0^{-y} \Delta T \, \mathrm{dy} = \Gamma \int_0^{-y} \frac{1}{r} dy \qquad 4.12$$

The left hand side of the equation can be solved by applying the finite difference method by using the trapezium rule.

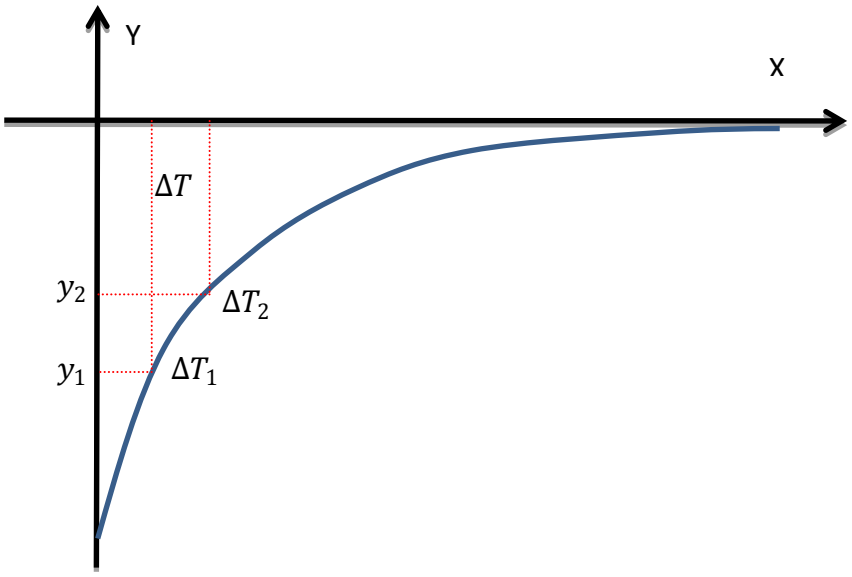

Figure 4.14 The definition of terms used for $\int_0^{-y} \Delta T_r \, \mathrm{dy}$ term using the trapezium rule

The right hand side of the equation can be calculated by observing the angle formed at the grain boundary groove cusp.

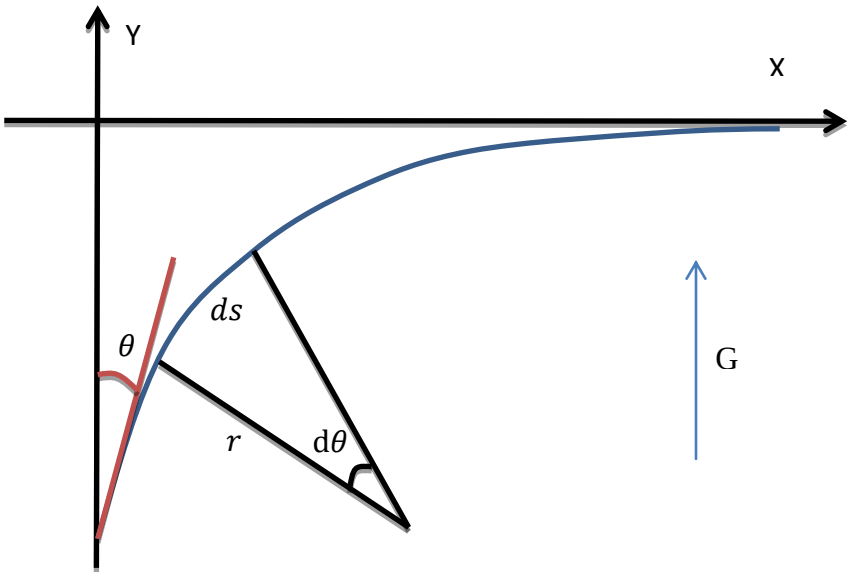

Figure 4.15 The definition to show $r\ d\theta = ds$

By using the definition $r\ d\theta = ds$ as shown in the figure 4.15 , it can be deduced,

$$\mathrm{r} = \frac{ds}{d\theta} = \frac{ds}{dy}\frac{dy}{d\theta} = \frac{1}{cos\theta}\frac{dy}{d\theta} \qquad \textbf{4.13}$$

And thus giving

$$\int_0^{-y} \frac{1}{r}\mathrm{dy} = \int_0^{\theta} \frac{1}{r} r cos\theta\ d\theta \qquad \textbf{4.14a}$$

or

$$\int_0^{-y} \frac{1}{r}\mathrm{dy} = (1 - \sin\theta) \qquad \textbf{4.14b}$$

By substituting equation 4.14b into equation 4.12, it gives

$$\int_{0}^{-y} \Delta T \, \mathrm{dy} = \Gamma(1 - \sin\theta) \qquad 4.15$$

To obtain a value for Gibbs Thomson coefficient Γ, the values of θ must be measured accurately for each points on the interface. This can be done by drawing a tangent at a point on the interface, but this is difficult and thus θ was calculated by using a Taylor expansion.

4.5.2 Taylor expansion

At any point along the interface, that point can be expanded about any point using a Taylor expansion. The Taylor expansion equation for a point about *a* for *x* gives,

$$\mathrm{x} = x_a + (y - y_a)\frac{dx}{dy} + \frac{(y - y_a)^2}{2!}\frac{d^2x}{dy^2} + \cdots \qquad 4.16$$

Where the terms higher than $\frac{d^2x}{dy^2}$ can be neglected.

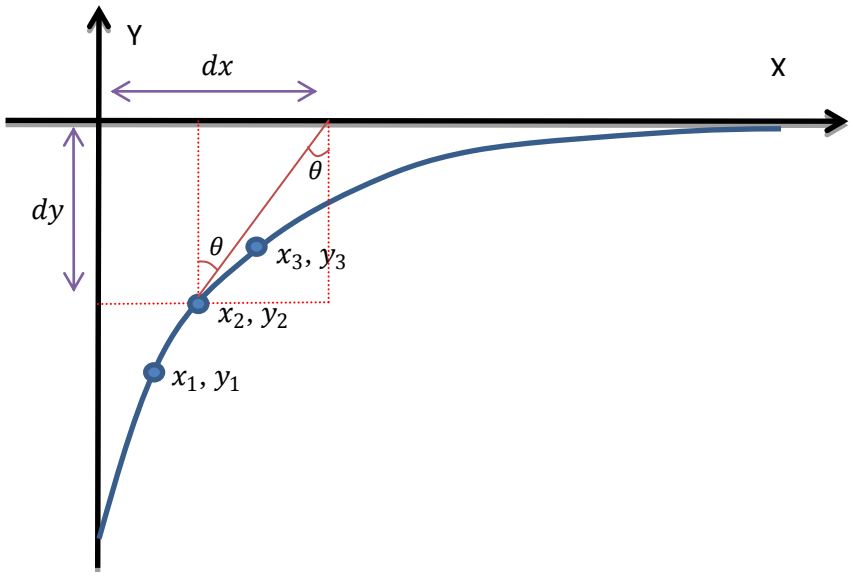

Figure 4.16 Schematic diagram to show the terms used for measuring angles for the use with Taylor expansion

From figure4.16, when the points 1 and 3 are expanded about point 2, it can be written as

$$x_1 = x_2 + (y_1 - y_2)\frac{dx}{dy} + \frac{(y_1 - y_2)^2}{2!}\frac{d^2x}{dy^2} \qquad \textbf{4.17a}$$

$$x_3 = x_2 + (y_3 - y_2)\frac{dx}{dy} + \frac{(y_3 - y_2)^2}{2!}\frac{d^2x}{dy^2} \qquad \textbf{4.17b}$$

By removing the $\frac{d^2x}{dy^2}$ term from equation 4.17a and 4.17b, and let $\mathrm{Y}_1 = \mathrm{y}_1 - \mathrm{y}_2$,$\mathrm{Y}_2 = \mathrm{y}_3 - \mathrm{y}_2$ and $\mathrm{X}_1 = x_1 - \mathrm{x}_2$, $\mathrm{X}_2 = \mathrm{x}_3 - x_2$, it gives,

$$\frac{dx}{dy} = \frac{\left(\frac{Y_1}{Y_2}X_2 - \frac{Y_2}{Y_1}X_1\right)}{Y_1 - Y_2} \qquad \textbf{4.18}$$

From figure 4.16, it can be seen that $\theta = \frac{dx}{dy}$ and thus,

$$\theta = tan^{-1}\left(\frac{dx}{dr}\right) \qquad \textbf{4.19a}$$

$$\theta = \frac{\left(\frac{Y_1}{Y_2}X_2 - \frac{Y_2}{Y_1}X_1\right)}{Y_1 - Y_2} \qquad \textbf{4.19b}$$

4.5.3 Calculation of the undercooling ΔT

For the case where the thermal conductivity values for the solid and liquid are equal, the temperature difference from the flat interface to the curved interface ΔT, only depends on the distance from the flat interface to a point on the curved interface y, and the temperature gradient G. That is,

$$\Delta T = Gy \tag{4.20}$$

From the equation 4.15, the Gibbs Thomson equation can be given as,

$$G_S \int_0^{-y} y\, dy = \Gamma(1 - sin\theta) \tag{4.21a}$$

Or

$$\Gamma = \frac{G_S y^2}{2(1 - sin\theta)} \tag{4.21b}$$

By using the equation 4.21, the Gibbs Thomson coefficient can be calculated directly by measuring the values for $y$and θ.

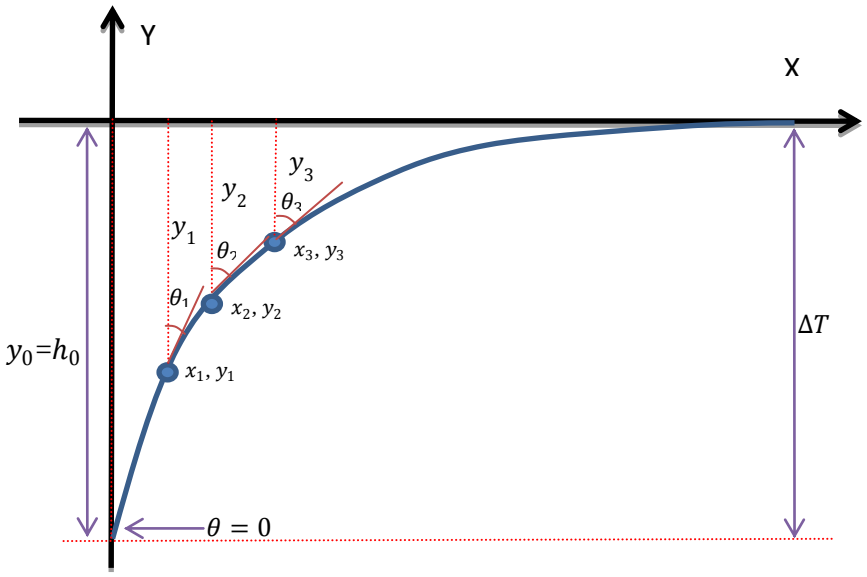

Figure 4.17 Schematic diagram showing the terms used for calculating ΔT in $K_S = K_L$ case.

By referring to figure 4.17, when $\theta = 0$and y $= h_0$, equation 4.21 gives

$$\Gamma = \frac{G_S h_0^2}{2} \qquad \textbf{4.22}$$

Which means,

$$\sigma_{SL} = \frac{G_S h_0^2}{2} \Delta S_f \qquad \textbf{4.23}$$

Where G_S is the temperature gradient in the solid phase, h_0 is the maximum groove depth and the ΔS_f is the entropy of fusion.

This equation can be used to calculate the solid-liquid interfacial energy for materials with the equal thermal conductivity values of solid and liquid phases by measuring h_0 and obtaining

values for G_S and ΔS_f. The Gibbs Thomson coefficient values at any points on the grain boundary groove shape should be the same theoretically. However the difficulty in measuring the values near the grain boundary groove junction and also the flat interface causes large errors in the value of Γ and thus leading to large errors in the value of σ_{SL}.

4.6 The effective entropy change

To be able to acquire the solid liquid interface energy value, the effective entropy change per unit volume value for solid phase is needed. This is given as,

$$\Delta S_f = \frac{(1 - C_S)(S_A^L - S_A^S) + C_S(S_B^L - S_B^S)}{V_S} \quad \textbf{4.24}$$

Where C_S is the composition of solid phase, S_A^L, S_A^S, S_B^L, S_B^S are partial molar entropies for materials A and B

The undercooling at constant composition and the change in composition at constant temperature may be related as the entropy term is not generally available.For a sphere,

$$\Delta C_r = \frac{2\sigma_{SL} V_S (1 - C_L) C_L}{rRT_M (C_S - C_L)} \quad \textbf{4.25}$$

Where $V_S$is the molar volume of solid phase, $R$is the gas constant, $T_M$is the melting temperature

For small changes,

$$\Delta T_r = m_L \Delta C_r = \frac{2 m_L \sigma_{SL} V_S (1 - C_L) C_L}{r R T_M (C_S - C_L)} \quad \textbf{4.26}$$

Where m_L is the liquidus slope

If spherical solid has value of $r_1 = r_2 = r$, the curvature undercooling is given as,

$$\Delta T_r = \frac{2\sigma_{SL}}{r \Delta S_f} \quad \textbf{4.27}$$

For an alloy, the entropy change can be given as,

$$\Delta S_f = \frac{R T_M \, (C_S - C_L)}{m_L V_S \, (1 - C_L) C_L} \quad \textbf{4.28}$$

Where R is the gas constant, T_M is the temperature, C_S is the composition of solid, C_L is the composition of liquid, m is the liquidus slope, V_S is the molar volume.

The molar volume term, V_S, may be given as,

$$V_S = V_c N_a \frac{1}{n} \qquad 4.29$$

Where V_c is the volume of unit cell, N_a is the Avogadro's number, n is the number of atoms per unit cell

4.7 The composition analysis

The composition profile of the sample was carried out using SEM and EDX analysis, where the sample was placed inside SEM and a line scan was done perpendicular to the solid-liquid interface, scanning from a solid phase across the solid-liquid interface and to the liquid phase. This was to confirm that the experiment carried out was successful in obtaining the equilibrated interface.

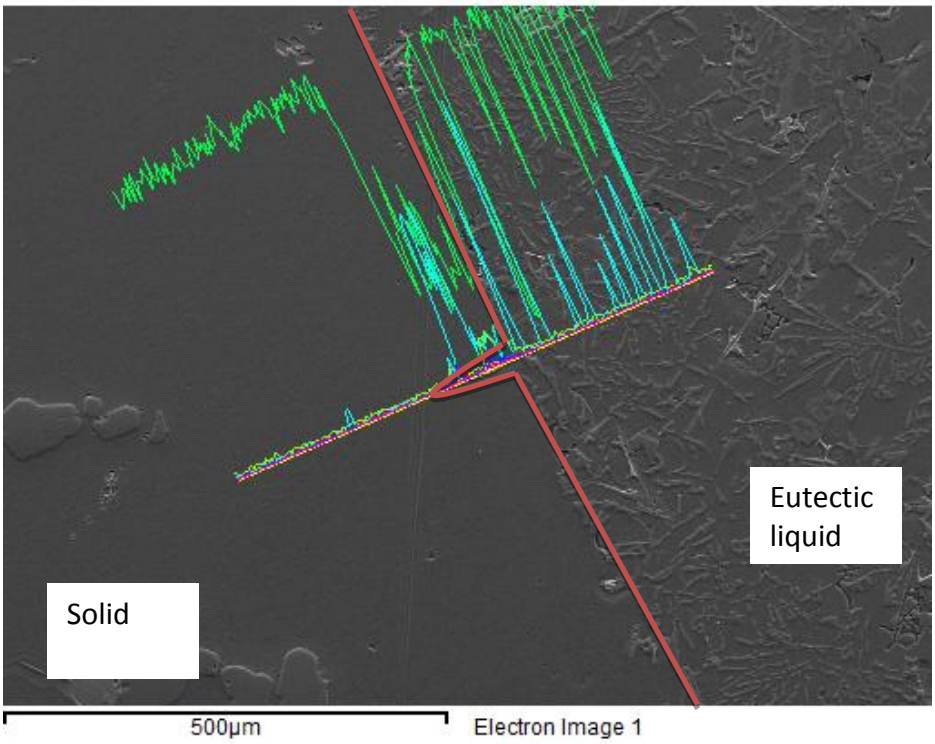

Figure 4.18a SEM image of the equilibrated solid-liquid interface of LM25 and the line scan perpendicular to the interface(red line) through grain groove

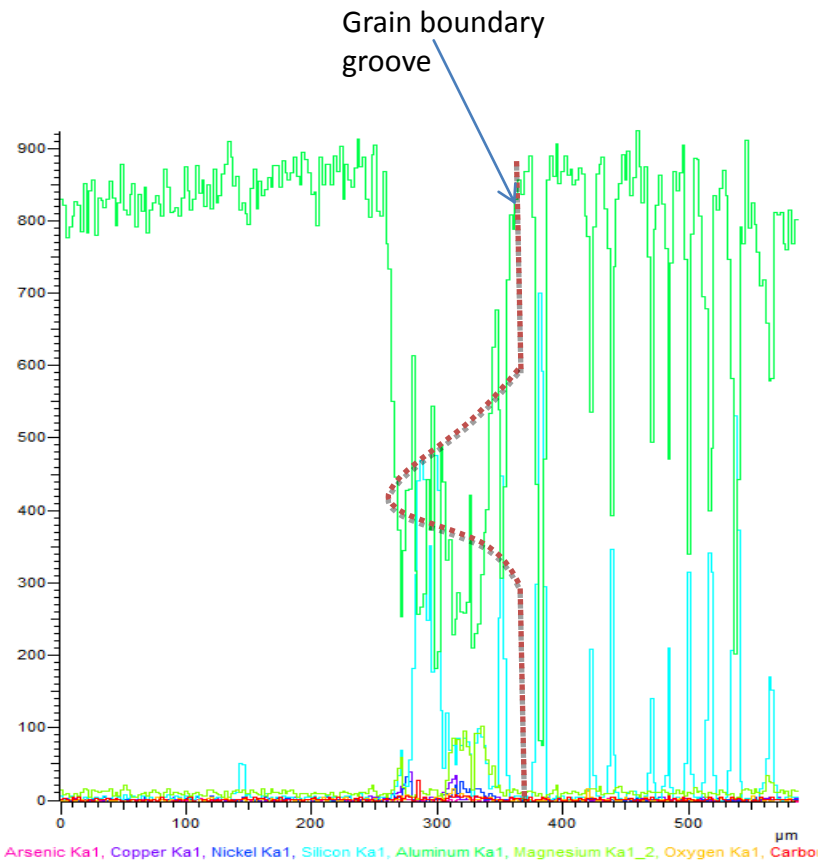

Figure4.18b The line scan perpendicular to the solid-liquid interface (line is on the groove cusp) and showing the counts of elements present along the scan line

In the figure 4.18b the x axis represents the distance along the line scan and the y axis represent the count of elements. The green line represents the count for Aluminium and the light blue line represents the Silicon count. The quantitative line scan picks up other elements but the counts are very small it is negligible. The line scan show that in the solid phase, only Aluminium is the counted which show that it consists of α-Al. As the scan reaches the groove shape and the interface, the line scan picks up Silicon show that it consists of eutectic liquid of Al-Si.

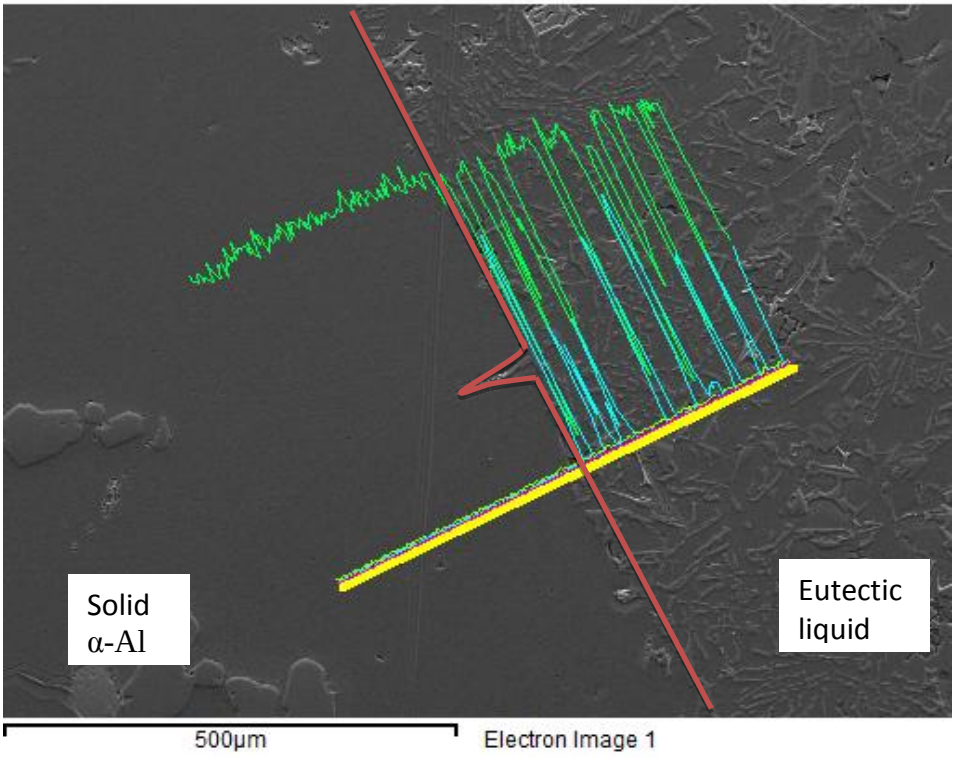

Figure 4.19a SEM image of the solid-liquid interface with grain boundary groove with line scan (yellow) perpendicular to the interface (red)

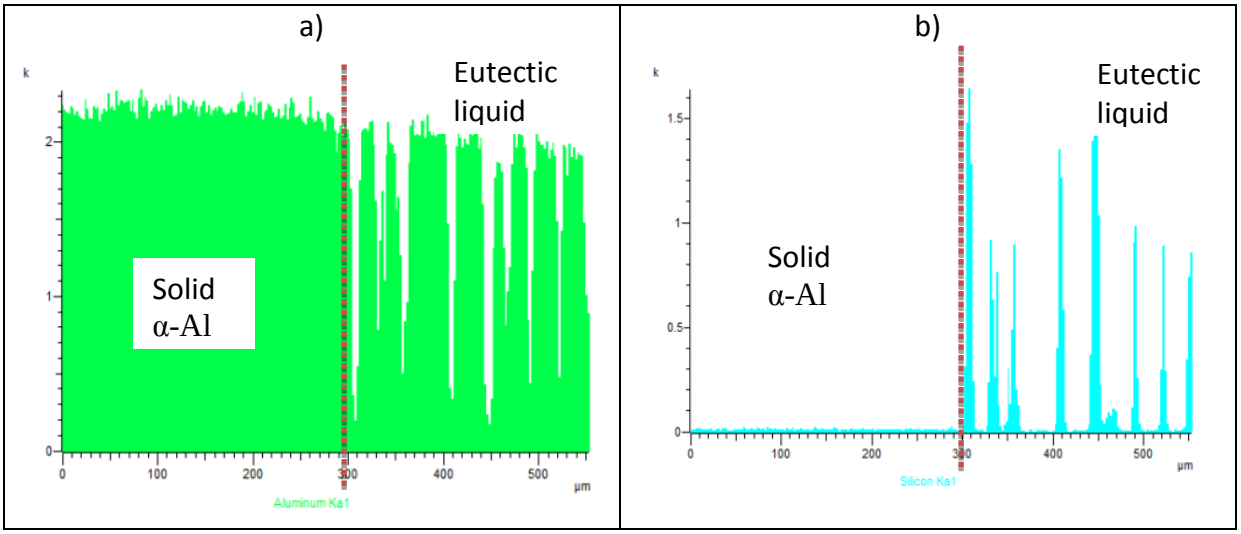

Figure 4.19b The line scan result with element counts for a) Aluminium, b) Silicon, with red line representing the interface

In figure 4.19a, the line scan was done away from the grain groove perpendicular to the solid-liquid interface along the yellow line. In figure 4.19b, a) represents the counts for the aluminium and in the solid the high count of aluminium thus confirming it is α-Al. The bright blue line represents Silicon in b), and from the scan it can be seen that the eutectic liquid phase has mixture of aluminium and silicon as the main element present and other elements are minimal. There is a clear count difference in the phases between solid and liquid about the interface, however on figure 4.18b, the line scan shown does not represent the element distribution of equilibrated interface. There is a trend of increase element count near both side of the interface that gradually decreases away from the interface.Not equilibrated groove could lead to errors in the calculation and needs to be considered.

4.8 Direct application of Gibbs Thomson equation on Grain boundary groove

The grain boundary groove shapes were obtained and drawn for calculating the solid-liquid interfacial energy values. The grain boundary groove shapes were selected and drawn as below to calculate Gibbs Thomson coefficient values.

For groove number 1,

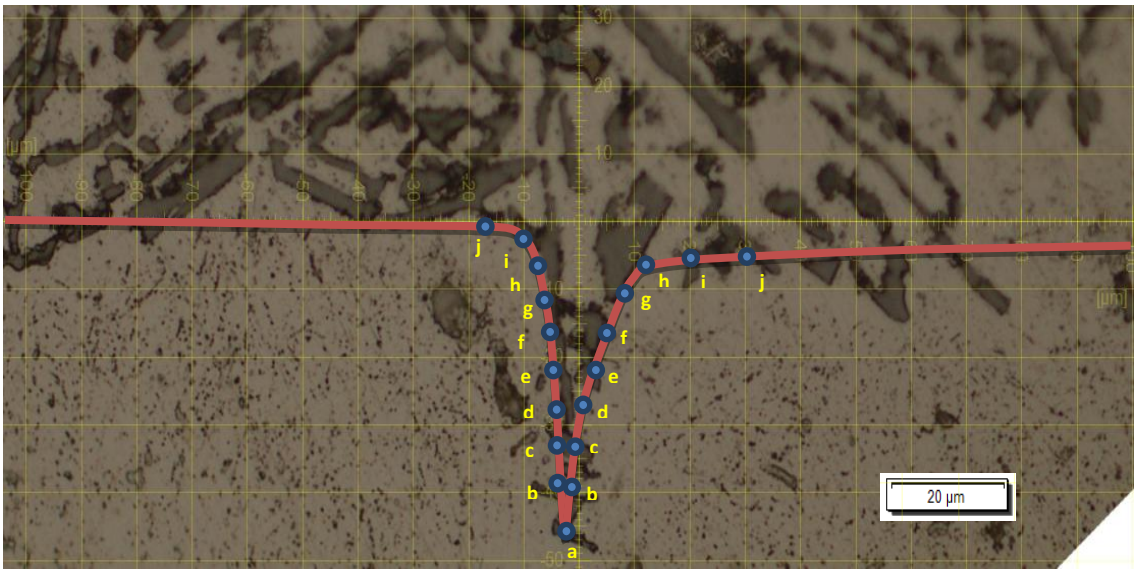

Figure 4.20 The grain boundary groove shape and the analysis points for groove 1

Temperature gradient G_s (°C/cm)	(L)	Distance from flat surface (μm)	θ°	Γ ($x10^{-5}$ K cm)	(R)	Distance from flat surface (μm)	θ°	Γ ($x10^{-5}$ K cm)
2.747	a	48.23	3.87	3.491	a	45.25	3.51	2.996
	b	42.25	7.33	2.810	b	39.67	7.94	2.507
	c	37.35	8.45	2.246	c	33.77	16.73	2.199
	d	31.75	9.67	1.664	d	26.98	30.69	2.042
	e	25.91	30.21	1.856	e	21.47	44.22	2.092
	f	19.73	43.57	1.721	f	16.85	52.37	1.875
	g	15.23	54.04	1.672	g	5.74	74.84	1.300
	h	9.85	64.62	1.381	h	2.21	85.21	1.921
	i	5.11	79.08	1.981	i	1.10	87.96	2.622
	j	1.21	87.58	2.254	j	0.67	88.99	3.968

Table 4.4 Gibbs Thomson coefficient values for each analysis points on groove 1

For groove number 2,

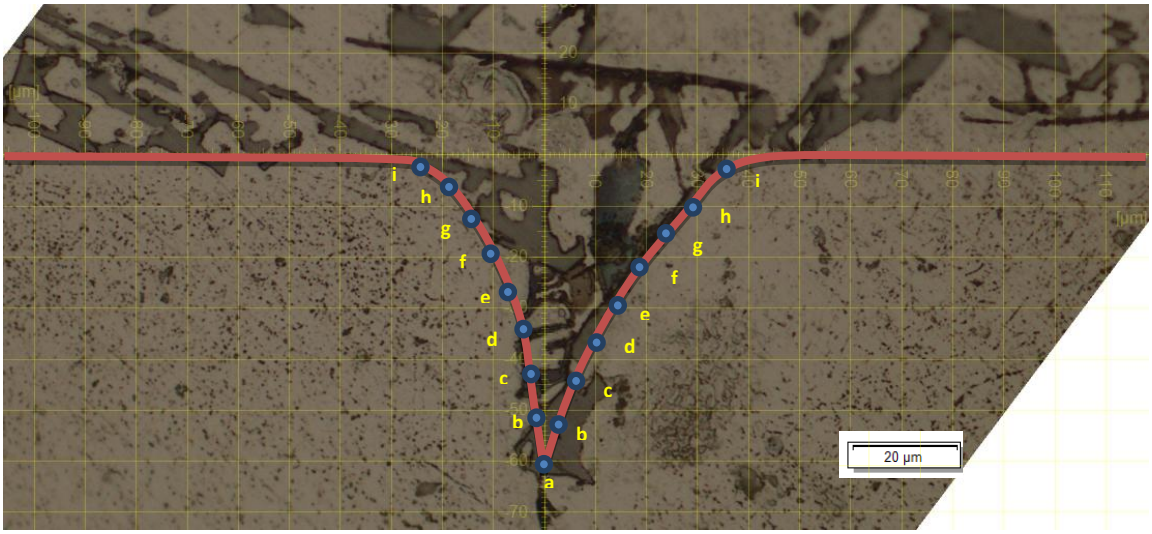

Figure 4.21 The grain boundary groove shape and the analysis points for groove 2

Temperature gradient G_s (°C/cm)	(L)	Distance from flat surface (µm)	θ°	Γ (x10^{-5} K cm)	(R)	Distance from flat surface (µm)	θ°	Γ (x10^{-5} K cm)
1.7213	a	62.95	5.51	3.773	a	62.95	12.81	4.382
	b	53.29	8.96	2.894	b	56.87	15.52	3.800
	c	45.08	10.80	2.247	c	47.97	19.72	2.989
	d	36.77	19.57	1.749	d	38.07	30.12	2.504
	e	28.79	27.20	1.314	e	30.21	37.95	2.040
	f	23.19	45.69	1.627	f	25.82	42.47	1.767
	g	17.92	51.21	1.253	g	20.10	56.85	2.136
	h	5.06	78.27	1.055	h	9.98	70.89	1.555
	i	2.17	86.64	2.357	i	3.76	75.85	4.010

Table 4.5 Gibbs Thomson coefficient values for each analysis points on groove 2

For groove number 3,

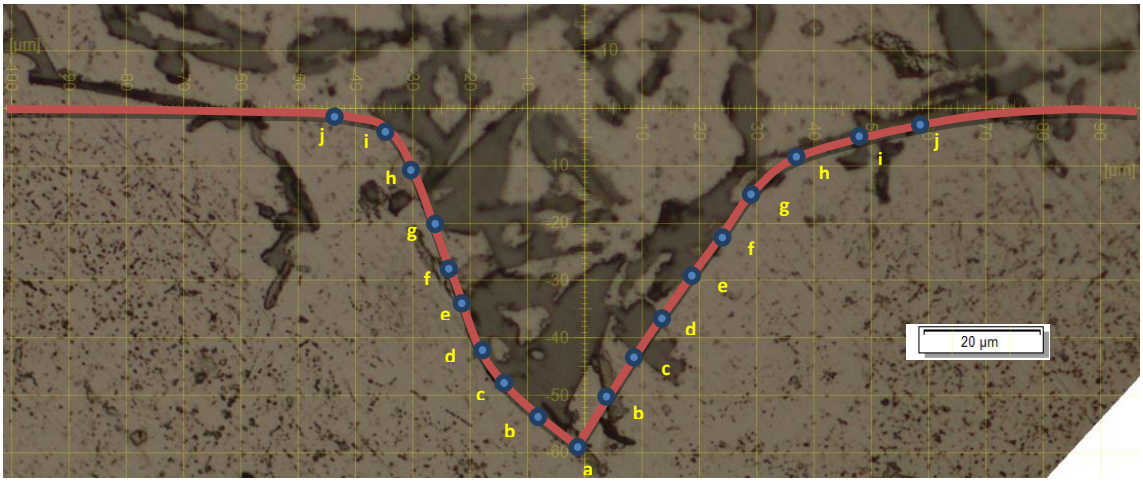

Figure 4.22 The grain boundary groove shape and the analysis points for groove 3

Temperature gradient G_s (°C/cm)	(L)	Distance from flat surface (µm)	θ°	Γ (x10^{-5} K cm)	(R)	Distance from flat surface (µm)	θ°	Γ (x10^{-5} K cm)
1.4377	a	49.66	34.87	4.139	a	49.66	30.72	3.624
	b	43.11	38.95	3.598	b	43.30	32.50	2.913
	c	35.52	43.30	2.887	c	36.32	38.13	2.478
	d	31.75	36.72	1.802	d	30.73	39.34	1.854
	e	27.23	38.13	1.393	e	24.10	41.97	1.260
	f	19.84	55.97	1.652	f	19.06	55.84	1.514
	g	14.33	66.82	1.829	g	14.27	69.31	2.269
	h	11.28	72.76	2.036	h	8.56	77.15	2.103
	i	4.15	82.73	1.540	i	3.68	83.71	1.617
	j	1.21	88.64	3.736	j	1.78	87.64	2.685

Table 4.6 Gibbs Thomson coefficient values for each analysis points on groove 3

For groove number 4,

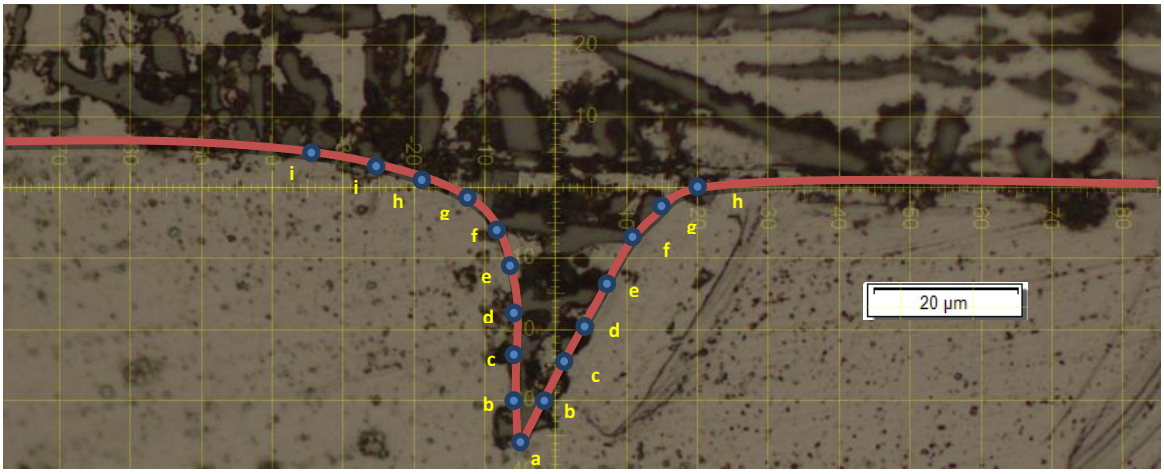

Figure 4.23 The grain boundary groove shape and the analysis points for groove 4

Temperature gradient G_s (°C/cm)	(L)	Distance from flat surface (µm)	θ°	Γ (x10^{-5} K cm)	(R)	Distance from flat surface (µm)	θ°	Γ (x10^{-5} K cm)
3.8937	a	33.19	1.75	2.212	a	33.19	25.31	3.746
	b	29.25	3.36	1.769	b	28.40	25.99	2.795
	c	23.73	2.94	1.756	c	23.73	36.68	2.723
	d	18.45	31.45	1.386	d	18.21	38.81	1.729
	e	14.11	41.75	1.160	e	15.03	47.59	1.681
	f	10.98	62.12	2.022	f	11.54	58.67	1.778
	g	9.57	70.84	3.218	g	5.74	78.88	3.417
	h	4.65	78.73	2.183	h	2.21	85.21	2.722
	i	1.54	80.31	3.236				

Table 4.7 Gibbs Thomson coefficient values for each analysis points on groove 4

For groove number 5,

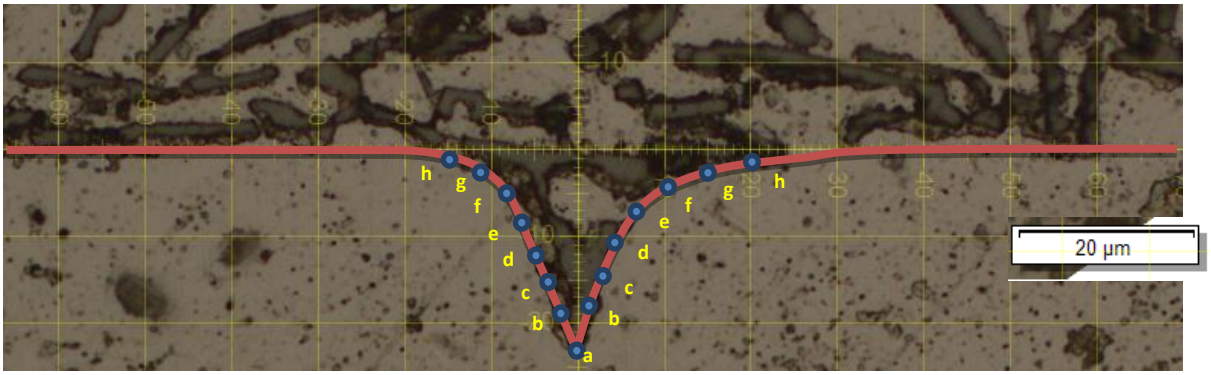

Figure 4.24 The grain boundary groove shape and the analysis points for groove 5

Temperature gradient G_s (°C/cm)	(L)	Distance from flat surface (µm)	θ°	Γ (x10^{-5} K cm)	(R)	Distance from flat surface (µm)	θ°	Γ (x10^{-5} K cm)
4.5497	a	23.73	28.84	2.474	a	23.73	27.66	2.391
	b	19.80	39.99	2.495	b	18.42	33.35	1.714
	c	16.98	48.84	2.654	c	15.04	45.54	1.798
	d	12.20	59.25	2.408	d	11.09	57.71	1.809
	e	9.15	65.97	2.197	e	7.91	68.55	2.055
	f	5.74	76.18	2.589	f	3.37	82.20	2.792
	g	3.17	82.20	2.471	g	2.24	84.60	2.572
	h	2.01	85.47	2.942	h	1.49	86.59	2.852

Table 4.8 Gibbs Thomson coefficient values for each analysis points on groove 5

For groove number 6,

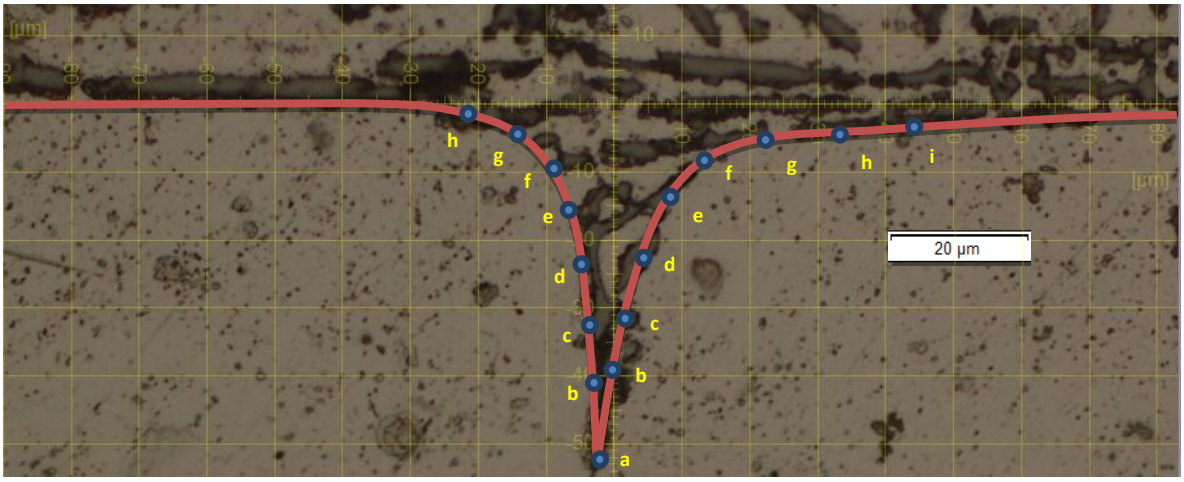

Figure 4.25 The grain boundary groove shape and the analysis points for groove 6

Temperature gradient G_s (°C/cm)	(L)	Distance from flat surface (µm)	θ°	Γ (x10^{-5} K cm)	(R)	Distance from flat surface (µm)	θ°	Γ (x10^{-5} K cm)
2.901	a	50.43	10.89	4.548	a	50.43	11.57	4.614
	b	41.85	9.26	3.028	b	39.97	16.45	3.233
	c	33.91	10.58	2.043	c	35.76	20.93	2.886
	d	28.65	15.94	1.641	d	26.98	38.51	2.798
	e	20.34	29.11	1.169	e	18.97	44.18	1.722
	f	14.81	53.28	1.603	f	14.21	78.85	1.552
	g	8.82	69.09	1.713	g	6.91	78.32	3.345
	h	4.41	82.78	3.558	h	4.71	80.64	2.417
					i	1.99	85.98	2.335

Table 4.9 Gibbs Thomson coefficient values for each analysis points on groove 6

When the groove shapes that are obtained above, it can be observed for example in figure 4.20 that the flat interface line is not symmetrical, which could mean that the apparatus was not providing radial temperature field. The image appears to indicate lack of uniformity in the groove shapes which may invalidate results from this groove shape. In terms of the flat line position and the groove shape line, for example in figure 4.22, there are eutectic phases occurring beneath the groove and the flat interface line that is drawn.This ambiguity in the groove shape line could lead to huge scatters in Gibbs Thomson coefficient value. These need to be considered when calculating error values.

A good example of the groove shape that could be used to give accurate analysis is shown in figure 4.24, where the flat interface and the groove shape is symmetrical.

4.9 The average value of Gibbs Thomson coefficient and solid-liquid interfacial energy

Γ (x10^{-5} K cm)											
Groove 1		**Groove 2**		**Groove 3**		**Groove 4**		**Groove 5**		**Groove 6**	
LHS	**RHS**	**LHS**	**RHS**	**LHS**	**RHS**	**LHS**	**RHS**	**LHS**	**RHS**	**LHS**	**RHS**
3.491	2.996	3.773	4.382	4.139	3.624	2.212	3.746	2.474	2.391	4.548	4.614
2.81	2.507	2.894	3.800	3.598	2.913	1.769	2.795	2.495	1.714	3.028	3.233
2.246	2.199	2.247	2.989	2.887	2.478	1.756	2.723	2.654	1.798	2.043	2.886
1.664	2.042	1.749	2.504	1.802	1.854	1.386	1.729	2.408	1.809	1.641	2.798
1.856	2.092	1.314	2.040	1.393	1.260	1.16	1.681	2.197	2.055	1.169	1.722
1.721	1.875	1.627	1.767	1.652	1.514	2.022	1.778	2.589	2.792	1.603	1.552
1.672	1.300	1.253	2.136	1.829	2.269	3.218	3.417	2.471	2.572	1.713	3.345
1.381	1.921	1.055	1.555	2.036	2.103	2.183	2.722	2.942	2.852	3.558	2.417
1.981	2.622	2.357	4.010	1.54	1.617	3.236					2.335
2.254	3.968			3.736	2.685						
Average											
2.108	2.352	2.029	2.798	2.417	2.408	2.105	2.574	2.529	2.248	2.413	2.767
2.2299		2.414		2.3465		2.339		2.388		2.589	

Table 4.10. Gibbs Thomson coefficient values obtained for the 6 grain boundary grooves analysed

The equation 4.30 can be used to calculate Gibbs Thomson coefficient value Γ, and the variables are shown in the results above, and thus giving the values below,

$$\Gamma = \frac{G_S y^2}{2(1 - sin\theta)} \qquad 4.30$$

Where G_S is the temperature gradient of solid, y is the distance from flat interface to a point on the groove and θ is the tangent angle from a point on the groove to vertical line

By using the formula below, the solid-liquid interfacial energy can be found,

$$\Gamma = \frac{\sigma_{SL}}{\Delta S_f} \qquad 4.31$$

The effective entropy change

$$\Delta S_f = \frac{RT_M\ (C_S - C_L)}{m_L V_S\ (1 - C_L) C_L} \qquad 4.32$$

Where R is the gas constant, T_M is the eutectic temperature, C_S is the composition of solid, C_L is the composition of liquid, m is the liquidus slope, $V_S$is the molar volume

$$V_S = \frac{M}{\rho} \tag{4.33}$$

Where M is atomic mass and ρ is the density

$$f(C) = \frac{(C_S - C_L)}{(1 - C_L)C_L} \cong \frac{(C_S - C_E)}{(1 - C_E)C_E} \tag{4.34}$$

Thus,

$$f(C) = \frac{(C_S - C_L)}{(1 - C_L)C_L} \cong \frac{(C_S - C_E)}{(1 - C_E)C_E} \tag{4.35}$$

System	Solid phase (C_S)	Quenched liquid phase (C_E)	Eutectic Temp. T_m (K)	Atomic mass of the solid phase (g)	Density of the solid phase (g/cm^3)	Liquidus slope m_L x10^2 (K/at fr)	F(C)	V_S (cm^3)
LM25 (Al-Si)	Al α (Al-1 at%Si) (Al-1 wt%Si)	Al-6.7at%Si Al-7wt%Si	888	26.9815	2.641	-9.375	-0.911	10.216

Table 4.11 The variables used to calculate the effective entropy change to calculate interfacial energy

$$\Delta S_f{}^* = \frac{RT_M}{m_L V_S} f(C) \qquad 4.36$$

Thus by substituting the values calculated in table 4.11 to equation 4.36, the effective entropy change can be calculated. The effective entropy change $\Delta S_f{}^*$ for LM25 is 0.7019 x 10^7(erg/K cm^2)

By using equation 4.31, the σ_{SL} can be given as,

	1	2	3	4	5	6
Γ ($x10^{-5}$ K cm)	2.2299	2.414	2.3465	2.339	2.388	2.589
ΔS_f (erg/K cm^2)	0.7019 x 10^7					
σ_{SL} (erg/cm^2)	156.5167	169.4387	164.7008	164.1744	167.6137	181.7219
	167.361± 8.312 erg/cm^2					

Table 4.12 The calculation of solid-liquid interfacial energy by averaging the values obtained for 6 grain boundary grooves

The standard deviation for the Gibbs Thomson coefficient can be calculated using,

$$\sigma = \sqrt{\frac{\sum(x - \bar{x})^2}{N - 1}} \quad 4.37$$

System	Solid Phase	Liquid Phase	Temperature(°C)	σ_{SL} (mJ/m^2)	work
Al-Cu	Al	AlCu	548	163.40±21.20	[45]
Al-Cu	Al	AlCu	548	160.01±19.20	[80]
Al-Si	Al	AlSi	577	168.95±21.90	[45]
Al-Mg	Al	AlMg	450	149.20±19.40	[46]
Al-Ni	Al	AlNi	640	171.56±20.58	[80]
Al-Ti	Al	AlTi	665	174.62±20.95	[80]
LM25	Al	AlSi	612	167.361±8.312	Present work

Table 4.13A comparison of the interfacial energy values from the literature survey on aluminium based system.

4.10 Error analysis in measuring thermal conductivity value

The error in measuring thermal conductivity of solid, K_S can be calculated by expressing the fractional total uncertainty in K_S, shown as,

$$\left|\frac{\Delta K_S}{K_S}\right| = \left|\frac{\Delta(Q_b - Q_a)}{Q_b - Q_a}\right| + \left|\frac{\Delta\left(\left({T_2}^b - {T_2}^a\right) - \left({T_3}^b - {T_3}^a\right)\right)}{\left({T_2}^b - {T_2}^a\right) - \left({T_3}^b - {T_3}^a\right)}\right| + \left|\frac{\Delta l}{l}\right| + \left|\frac{\Delta r_2}{r_2 \ln\left(\frac{r_3}{r_2}\right)}\right| + \left|\frac{\Delta r_3}{r_3 \ln\left(\frac{r_3}{r_2}\right)}\right| \quad \textbf{4.38}$$

a) Fractional uncertainty in the power measurement

The input power is given as,

$$\mathrm{Q} = \frac{V_{sh}}{R_{sh}} V_h \quad \textbf{4.39}$$

Where V_{sh} is the potential difference between ends of shunt, and V_h is the potential difference between the ends of the heating element, and R_{sh} is the shunt resistance. The fractional uncertainty in the input power can be,

$$\left|\frac{\Delta(Q_b - Q_a)}{Q_b - Q_a}\right| = \left|\frac{\Delta R_{sh}}{R_{sh}}\right| + \left|\frac{\left({V_2}^{sh} - {V_1}^{sh}\right)\Delta V^h + \left({V_2}^h - {V_1}^h\right)\Delta V^{sh}}{{V_2}^h {V_2}^{sh} - {V_1}^h {V_1}^{sh}}\right| \quad \textbf{4.40}$$

The potential differences between the ends of both shunt and the central heating element were measured using a digital multimeter to an accuracy of ±0.5%. The resistance in the shunt was measured with a multimeter to an accuracy of 0.01% and the total fractional error in the input power was about 1%.

b) The fractional uncertainty in measurement of the fixed distances r_2 and r_3 and the length of the heating element wire *l*.

The fixed distances where the thermocouples were placed to measure temperatures r_2 and r_3 were measured with an optical microscope to an accuracy of ±10µm, and the length of the central heating element was measured to an accuracy of ±0.5mm. The total fractional uncertainty for both measurements was less than 0.6%.

4.11 The Error analysis in measuring temperature gradient

The accuracy of Gibbs Thomson coefficient depends on the accurate measurement of temperature gradient in solid phase. For a cylindrical sample the temperature gradient can be given as

$$G_S = -\frac{Q}{2\pi r l k_s} \qquad 4.41$$

Where Q is the input power, l is the central heating element length, k_s is the thermal conductivity of the solid phase and r is the distance from the centre of the cylinder to the solid-liquid interface.

The thickness of the liquid was obtained by observing the sample under the microscope and measured using the measuring tool in the software. The measured value of *r* was accurate to the accuracy of ±20µm. The fractional uncertainty in the measurement of temperature gradient is shown as,

$$\left|\frac{\Delta G_S}{G_S}\right| = \left|\frac{\Delta Q}{Q}\right| + \left|\frac{\Delta l}{l}\right| + \left|\frac{\Delta r}{r}\right| + \left|\frac{\Delta K_S}{K_S}\right| \qquad 4.42$$

$\left|\frac{\Delta Q}{Q}\right| \approx 1\%$, $\left|\frac{\Delta l}{l}\right| \approx 0.2\%$, $\left|\frac{\Delta r}{r}\right| \approx 0.5\%$, $\left|\frac{\Delta K_S}{K_S}\right| \approx 3\%$ at the eutectic temperature of the system. The total fractional uncertainty in the temperature gradient measurement can be given as about 5%.

4.12 Fractional uncertainty in calculating the effective entropy change

The fractional uncertainty in calculating the effective entropy change is expressed as

$$\left|\frac{\Delta(\Delta S^*)}{\Delta S^*}\right| = \left|\frac{\Delta T_m}{T_m}\right| + \left|\frac{\Delta V_S}{V_S}\right| + \left|\frac{\Delta f(C_S, C_L)}{f(C_S, C_L)}\right| \quad 4.43$$

The accuracy of T_m is estimated to be ±0.5K, so the $\left|\frac{\Delta T_m}{T_m}\right| \approx 0.1\%$. The composition of the liquid and solid phases are known to accuracy of 0.1-0.3%, and the fractional uncertainty of the composition is in order of 0.5%. The largest contribution to the error is caused by the liquidus slope measurement as it might be as large as 4-5%. Thus the total error in calculating the effective entropy change can be estimated to around 5%.

5 Conclusion and Further work

The Solid-liquid interfacial energy plays an important role in liquid to solid transformation process, thus it is important to have a quantitative values of interfacial energy. In recent years, the most powerful method considered in measuring the solid-liquid interfacial energy is the

grain boundary groove method. The grain boundary groove shape is obtained by annealing the alloy in a temperature gradient. The purpose of the present work was to design, build and commission a novel apparatus to be used in measuring the solid-liquid interfacial energy.

The radial heat flow apparatus was designed and built to obtain equilibrated grain boundary groove shape. The new apparatus provided more accurate and stable temperature control over longer period of the experiment by using coiled heating element and electromagnetic shielding and provided better safety features by using DC power supply. The apparatus is improved the operating capabilities of working at higher temperatures of up to 900K with a very stable temperature control (±0.05K) over the duration of the experiment which was near 10 days. The apparatus was tested and an experiment was carried out using a commercial alloy LM25 (Al-7wt%Si).

The apparatus was used to measure thermal conductivity of solid phase of the alloy. The result obtained compared reasonable with the literature value. The experiment to obtain grain boundary groove shape was done using the radial heat flow apparatus. The alloy was held in a stable temperature gradient provided by the central heating element in the centre of the sample and the water cooling jacket outside the sample. The experiment took around 10days to anneal the sample and once the experiment was finished, the sample was quenched to obtain the grain boundary groove shape.

The solid-liquid interfacial energy was calculated by directly observing the grain boundary groove shape obtained. Gibb Thomson equation was directly applied to the groove shape to calculate the solid-liquid interfacial energy. The result obtained was varied in success, as there were large scatters in data to be considered due to apparatus providing less reliable radial temperature gradient, however there were some good results that could provide good agreement with the literature.

The temperature control of the apparatus should be very accurate and the temperature fluctuation should be less than ±0.05K for the duration of the experiment to achieve a good equilibrated grain boundary groove shape. Small increase in temperature cause melting at the solid-liquid interface, and small decrease in temperature causes solidification at the interface.

These temperature fluctuations could prevent obtaining the equilibrated solid-liquid interface. The small increase in temperature could cause the equilibrated solid-liquid interface to melt. This could cause the liquid droplets or films to form in the grain boundaries which results in deeper groove than the equilibrated groove shape. This could have caused large errors in the results.

Thus the future work into the study could be to design a highly accurate temperature design with good insulation to prevent temperature fluctuation. Also the limitation of the current apparatus design is the working temperature of the apparatus. The apparatus can only work up to the temperature of 900K which limits the range of usage to measure high temperature alloys such as Nickel alloys. A further design and improvement could be carried out to improve the working temperature to above 1500℃.

The grain boundary shapes obtained were asymmetric and this is because of the anisotropy of the grain boundary. The present work did not consider this anisotropy as the purpose of the work was to calculate the average solid-liquid interfacial energy around the grain boundary groove shape. The future work could be improved and include considering the anisotropy of the grain boundary and its effect on the interfacial energy.

6 References

[1] J.W. Martin, R.D. Doherty, B. Cantor;Stability of Microstructure in Metallic Systems, Cambridge University Press, Cambridge, United Kingdom, (1976 and 1997)

[2] D R H Jones, “Review The free energies of solid-liquid interfaces,” Journal of Materials Science 9 (1974)pg 1-17

[3] N. Eustathopoulos, M.G. Nicholas, B. Drevet;Wettability at High Temperatures, Pergamon, Oxford, United Kingdom, (1999)

[4] R.Gentle, W.Bolton, P.Edwards.; Mechanical Engineering Systems, Butterworth-Heinemann, (2001)

[5] http://en.wikipedia.org/wiki/Metastability

[6] M.F.Ashby, D.R.H.Jones.; Engineering Materials 2: An Introduction to Microstructures, Processing and Design, Third Edition, Butterworth-Heinemann, (2006) Pg56

[7] M. Gündüz, D. Phil. Thesis, University of Oxford, (1984)

[8] W.M. Ketcham and P.V.Hobbs; An experimental determination of the surface energies of ice, Philosophical Magazine, 19 (1969) pg 1161

[9] S.Suzuki and D.Kuroiwa; Grain-boundary energy and grain-boundary groove angles in ice, Journal of Glaciology, 11 (1972) pg265

[10] Herring, C.; The physics of powder metallurgy, McGraw-Hill, New York, (1951)pg143

[11] D. Turnbull; Formation of Crystal Nuclei in Liquid Metals,Journal of Applied Physics,21, (1950), pg 1022-28

[12]Amirfazli, A., Chatain, D., Neumann, A. W.; Drop size dependence of contact angles for liquid tin on silica surface: line tension and its correlation with solid-liquid interfacial

tension. Colloids and Surfaces A: Physicochemical and Engineering Aspects, 142(2-3), (1998), pg183–188

[13]Fukuda, A., Yoshikawa, T., Tanaka, T.; A fundamental approach for the measurement of solid-liquid interfacial energy. Journal of Physics: Conference Series, 165, (2009), pg 012079

[14] Levi, G., Kaplan, W. D.; Aluminium-alumina interface morphology and thermodynamics from dewetting experiments. ActaMaterialia, 51, (2003), pg2793–2802

[15] Li, D., & Neumann, A. W.; Equation of state interfacial tensions of solid-liquid systems. Advances in Colloid and Interface Science, 39, (1992), pg299–345

[16] Schwarz, B., Eisenmenger-Sittner, C., Steiner, H.; Construction of a high-temperature sessile drop device. Vacuum, 82(2), (2007)pg186–188

[17] Mazzola, L., Bemporad, E., Carassiti, F.; An easy way to measure surface free energy by drop shape analysis. Measurement, 45(3), (2012) pg 317–324

[18] Young, T.;An Essay on the cohesion of flueds, Philosophical Transactions of Royal society, London, 95 (1805) pg65-87 (Available at http://rstl.royalsocietypublishing.org/content/95/65.full.pdf)

[19] Dupré,A.;ThéorieMéchanique de la Chaleur, Gauthier-Illars (1869)

[20] Nakae. H.,Katoh. H.;Change in Surface Free Energy of Silicon in Si/Al-Si Systems during Wetting Measurement by The Sessile Drop Method, Journal of the Japan Institute of Metals and Materials,63 (1999) pg1356

[21] Levi. G., Kaplan. W. D.; Aluminium-aluminium interface morphology and thermodynamics from dewetting experiments,ActaMaterialia,51, (2003)pg2793

[22] Shinozaki. N., Satoh. N., Shinozaki. H., Wasai. K., Era. H.; Measurement of interfacial free energy between carbon saturated molten iron and graphite based on the sign rule,Journal of the Japanese Institute of Metals and Materials,70 (2006) pg950

[23] M.E. Glicksman,C.I.Vold; Determination of absolute solid-liquid interfacial free energies in metals, ActaMetallurgica, 17 (1969) pg 1

[24] M.E. Glicksman, C.I.Vold; ScriptaMaterialia, 5 (1971) pg 493

[25] R.C.Sill, A.S. Skapski; Method for the Determination of the Surface Tension of Solids, from Their Melting Points in Thin Wedges, The Journal of Chemical Physics,24 (1956) pg644

[26] A.S.Skapski, R.Billups, A. Rooney; Capillary Cone Method for Determination of Surface Tension of Solids

Journal of Chemical Physics,26 (1957) pg 1350

[27] A.S.Skapski, R.Billups, D. Casavant; Interfacial Tension Solid-Liquid of Benzene, Journal of Chemical Physics,31 (1959) pg 1431

[28] C.R.M.Wronski; The size dependence of the melting point of small particles of tin, British Journal of Applied Physics,18 (1967) pg1731

[29] C.Coombes; The melting of small particles of lead and indium, Journal of Physics F: Metla physics, 2 (1972) pg441

[30] J.R.Sambles;

An Electron Microscope Study of Evaporating Gold Particles: The Kelvin Equation for Liquid Gold and the Lowering of the Melting Point of Solid Gold Particles, Proceedings of the Royal Society A, 324 (1971) pg339

[31] G. Kanig; UntersuchungenüberSchmelz- und Gefriervorgänge in konzentriertenLösungen und gesättigtenGelen, Colloid and Ploymer Science, 173 (1960) pg97

[32] P.Kubelka and R. Procksha; EineneueMethodezurBestimmung der Oberflächenspannung von Kristallen, Colloid and Ploymer Science, 109 (1944) pg79

[33] B.R.Puri, L.R. Sharma and M.L. Lakhampal; J.Chem.Phys.,58(1954) pg 289

[34] B.R.Puri, D.D. Singh and Y.P.Myer; Freezing points of liquids adsorbed on porous solids, Transactions of the Faraday Society, 53, (1957)pg530

[35] D.R.H. Jones; Ph.D. Thesis, Cambridge University, (1970)

[36] G.F. Bolling and W.A. Tiller; Growth from the melt. I. Influence of surface intersections in Pure Metals, Journal of the Applied Physics, 31, (1960) pg 1345

[37] G.E Nash and M.E Glicksman; A general method for determining solid-liquid interfacial free energies, Philosophical Magazine, 24, (1971) pg 577

[38] N.B. Singh and M.E. Glicksman; J. Crystal Growth, 98 (1989) pg 573

[39] D.R.H. Jones; Rev. Sci. inst., 41, (1970) pg1509

[40] D.R.H. Jones;

The measurement of solid-liquid interfacial energies from the shapes of grain-boundary grooves

Philosophical Magazine, 27, (1973) pg569

[41] D.R.H. Jones and G.A. Chadwick;

Experimental measurement of the solid-liquid interfacial energies of transparent materials

Philosophical Magazine, 22 (1970) pg 291

[42] D.R.H. Jones and G.A. Chadwick;

An expression for the free energy of fusion in the homogeneous nucleation of solid from pure melts

Philosophical Magazine, 24 (1971) pg 995

[43] R.J. Schaefer, M.E. Glicksman and J.D. Ayers; High-confidence measurement of solid/liquid surface energy in a pure material, Philosophical Magazine, 32 (1975) pg 725

[44] S.C. Hardy; A grain boundary groove measurement of the surface tension between ice and water, Philosophical Magazine, 35 (1977) pg471

[45] M. Gündüz and J.D. Hunt; The measurement of solid-liquid surface energies in the Al-Cu, Al-Si and Pb-Sn systems,ActaMetallurgica, 33, 9, (1985) pg 1651

[46] M. Gündüz and J.D. Hunt; Solid-liquid surface energy in the Al-Mg system, ActaMetallurgica, 37, issue 7, (1989) pg 1839

[47] Böyük, U., Engin, S., &Maraşlı, N.; Novel experimental technique to observe equilibrated grain boundary groove shapes in opaque alloys. Journal of Alloys and Compounds, 476(1-2), (2009)pg213–219

[48] Engin, S., Böyük, U., &Maraşlı, N.; Determination of interfacial energies in the Al–Ag and Sn–Ag alloys by using Bridgman type solidification apparatus. Journal of Alloys and Compounds, 488(1), (2009)pg138–143

[49] Engin, S., Böyük, U., &Maraşlı, N.; Determination of solid–liquid interfacial energy for a solid Sn in equilibrium with a Sn–Ag–Zn eutectic liquid. Current Applied Physics, 11(4), (2011)pg1060–1066

[50] U. Böyük, N. Maraşlı, H. Kaya, E. Çadırlı, K. Keşlioğlu, Directional solidification of Al–Cu–Ag alloy, Applied Physics A, 95, (2009) pg 923–932,

[51] Bayender, B.; Solid–liquid surface energy of pivalic acid. Journal of Crystal Growth, 194(1), (1998) pg119–124

[52] Bayender, B.; Solid–liquid surface energy of pivalic acid. Journal of Crystal Growth, 194(1), (1998) pg119–124

[53] Bayender, B., Marali, N., Cadirli, E., &Gunduz, M.; Solid–liquid interfacial energy of camphene. Materials Science and Engineering A, 270(2), (1999)pg343–348

[54] Bayram, Ü.,Aksöz, S., &Maraşlı, N.; Solid–liquid interfacial energy of neopentylglycol solid solution in equilibrium with neopentylglycol–(D) camphor eutectic liquid. Journal of Crystal Growth, 338(1), (2012)pg181–188

[55] Bayram, Ü.,Aksöz, S., &Maraşlı,; N. Solid–liquid interfacial energy of solid aminomethylpropanediol solution in equilibrium with aminomethylpropanediol–neopentylglycol–D camphor liquid. ThermochimicaActa, 554, (2013)pg48–53

[56] Böyük, U., &Maraşlı, N.; Interfacial energies of carbon tetrabromide. Current Applied Physics, 9(2), (2009)pg359–366

[57] Boyuk, U., Keslioglu, K., Erol, M., &Marasli, N.; Measurement of solid–liquid interfacial energy in succinonitrile−pyrene eutectic system. Materials Letters, 59(23), (2005)pg2953–2958

[58] Böyük, U., Keşlioğlu, K., &Maraşli,; N. Solid–liquid interfacial energy of dichlorobenzene. Journal of Physics: Condensed Matter, 19(11), (2007) pg116202

[59] Erol, M.; Solid–liquid interfacial energy of bismuth in the Bi–Cd eutectic system. ScriptaMaterialia, 51(2), (2004)pg131–136

[60] Jones, D., & Chadwick, G.; Experimental measurement of solid-liquid interfacial energies: The ice-water-sodium chloride system. Journal of Crystal Growth, 11(3), (1971) pg 260–264

[61] Maraslı, N.; Solid–liquid interface energies in the succinonitrile and succinonitrile–carbon tetrabromide eutectic system. Journal of Crystal Growth, 247(3-4), (2003) pg613–622

[62] Ocak, Y., Akbulut, S., Boyuk, U., Erol, M., Keslioglu, K., &Marasli, N.; Measurement of solid–liquid interfacial energy for solid d-camphor solution in equilibrium with succinonitrile d-camphor eutectic liquid. ScriptaMaterialia, 55(3), (2006) Pg235–238

[63] Ocak, Y., Akbulut, S., Böyük, U., Erol, M., Keşlioğlu, K., &Maraşlı, N.; Solid–liquid interfacial energy for solid succinonitrile in equilibrium with succinonitrile dichlorobenzene eutectic liquid. ThermochimicaActa, 445(1), (2006) Pg86–91

[64] Özer, A., Bayram, Ü.,Aksöz, S., &Maraşlı, N.; Solid–liquid interfacial energy of neopentylglycol solid solution in equilibrium with succinonitrile-neopentylglycol-aminomethylpropanediol liquid. Journal of Crystal Growth, 364, (2013)pg34–39

[65] Akbulut, S., Ocak, Y., Marasli, N., Keslioglu, K., Kaya, H., &Cadirli, E.; Determination of interfacial energies of solid Sn solution in the In–Bi–Sn ternary alloy. Materials Characterization, 60(3), (2009)pg183–192

[66] Akbulut, S., Ocak, Y., Maraşlı, N., Keşlioğlu, K., Kaya, H., &Çadırlı, E.; Determination of solid–liquid interfacial energies in the In–Bi–Sn ternary alloy. Journal of Physics D: Applied Physics, 41(17), (2008)pg175302

[67] Bulla, a., Carreno-Bodensiek, C., Pustal, B., Berger, R., Bührig-Polaczek, a., & Ludwig, a.; Determination of the Solid-Liquid Interface Energy in the Al-Cu-Ag System. Metallurgical and Materials Transactions A, 38(9), (2007)pg1956–1964

[68] Jones, H.; An Evaluation of Measurements of Solid/Liquid Interfacial Energies in Metallic Alloy Systems by the Groove Profile Method,Metallurgical and Materials Transactions A, 38(7), (2007) pg1563–1569

[69] Kaygısız, Y., Akbulut, S., Ocak, Y., Keşlioğlu, K., Maraşlı, N., Çadırlı, E., & Kaya, H.; Experimental determination of solid–solid and solid–liquid interfacial energies of solid ε (CuZn5) in the Zn–Cu alloy. Journal of Alloys and Compounds, 487(1-2), (2009) pg103–108

[70]Keşlioğlu, K., Ocak, Y., Aksöz, S., Maraşlı, N., Çadırlı, E., & Kaya, H.; Determination of interfacial energies for solid al solution in equilibrium with Al-Cu-Ag liquid,Metals and Materials International, 16(1), (2010)pg 51–59

[71]Kesliolu, K., Erol, M., Marasli, N., &Gunduz, M.; Experimental determination of solid–liquid interfacial energy for solid Cd in Bi–Cd liquid solutions,Journal of Alloys and Compounds, 385(1-2), (2004)pg 207–213

[72]Meydaneri, F., Payveren, M., Saatçi, B., Özdemir, M., &Maraşlı, N.;Experimental determination of interfacial energy for solid Zn solution in the Sn-Zn eutectic system. Metals and Materials International, 18(1), (2012) pg95–104

[73]Meydaneri, F., Saatçi, B., Gündüz, M., &Özdemir, M.; Determination of thermal conductivities of Sn–Zn lead-free solder alloys with radial heat flow and Bridgman-type apparatus. Continuum Mechanics and Thermodynamics,(2012)

[74] F. Meydaneri, B.Saatçi, M. Özdemir; Experimental determination of solid–liquid interfacial energy for solid Sn in the Sn–Mg system,Applied Surface Science, 257(15), (2011)pg6518–6526

[75] B. Saatçi, H.Pamuk; Experimental determination of solid–liquid surface energy for Cd solid solution in Cd–Zn liquid solutions,Journal of Physics: Condensed Matter, 18(45), (2006) pg10143–10155

[76] M.Volmer, A. Webber; ZeitschriftfürPhysikalischeChemie, 119 (1925) pg277

[77] R. Becker, W. Doring; Annals of Physics, 24 (1935) pg 719

[78] B. Chalmers; Principles of solidification, John Wiley and Sons, New York, (1964), pg 62

[79] J.H. Holloman; Heterogeneous Nucleation, Thermodynamics in physical metallurgy, ASM, (1950)

[80] N. Maraşlı, J.D. Hunts, “SOLID-LIQUID SURFACE ENERGIES IN THE Al-CuAl,, Al-NiAl, AND Al-Ti SYSTEMS,” Acta Metallurgica 44, no. 3 (1996) pg 1085-1096.

[81] J.R. Leigh; Temperature measure and control, Peter Peregrinus Ltd,(1998)

[82] R.C. Dorf; Modern control systems, Addison-Wesley, (1992)

[83] http://www.expertune.com/tutor.html

[84] D.W. Clarke; PID algorithms and their computer implementation, Oxford Press, (1983)

[85] http://www.ni.com/white-paper/3782/en/

[86] http://www.expertune.com/artCE87.html (published in control Engineering, March 1987)

[87] Eurotherm Controls, Control loop parameter setting: 900 EPC series handbook

[88] https://thaicontrol.files.wordpress.com/2011/11/tune1.jpg

[89] J.G. Ziegler,N.B. Nichols;"Optimum settings for automatic controllers" (PDF), Transactions of the ASME 64: (1942) pg759–768

[90] British and European Aluminium Casting Alloys: their properties and characteristics, edited R Bartley, Publ. Assoc. Light alloy refiners, Birmingham (1992)

[91] M.J. Richardson, D. Hayes, A.P. Day, K.C. Mills; Final report on differential scanning calorimetry, PMP, CMMT, NPL (1996)

[92] K.C. Mills; Recommended values of Thermophysical properties for selected commercial alloys, Woodhead Publishing, (2002)

[93]D.R.H. Jones and G.A. Chadwick;

Experimental measurement of the solid-liquid interfacial energies of transparent materials

Philosophical Magazine, 22 (1970) pg 291

[94] D.R.H. Jones; PhD. Thesis, Cambridge University, (1970)

[95] J. Liu, R.L. Davidchack, H.B. Dong; Molecular dynamics calculation of solid–liquid interfacial free energy and its anisotropy during iron solidification, Computational Materials Science, 74 (2013) pg92–100